

FORMATION AND TRANSFORMATION OF AMORPHOUS
CALCIUM-MAGNESIUM CARBONATES IN SYNTHETIC SEAWATER

BY

JARED WESLEY SINGER

A THESIS

SUBMITTED TO THE FACULTY OF

ALFRED UNIVERSITY

IN PARTIAL FULFILLMENT OF THE REQUIREMENTS
FOR THE DEGREE OF

DOCTOR OF PHILOSOPHY

IN

MATERIAL SCIENCE AND ENGINEERING

ALFRED, NEW YORK

FEBRUARY, 2013

Alfred University theses are copyright protected and may be used for education or personal research only. Reproduction or distribution in any format is prohibited without written permission from the author.

FORMATION AND TRANSFORMATION OF AMORPHOUS
CALCIUM-MAGNESIUM CARBONATES IN SYNTHETIC SEAWATER

BY

JARED WESLEY SINGER

B. S. UNIVERSITY OF UTAH, CHEMISTRY, 2006

M. S. UNIVERSITY OF UTAH, GEOLOGY, 2013 (ANTICIPATED)

SIGNATURE OF AUTHOR _____ (Signature on File)

APPROVED BY _____ (Signature on File)
GEOFFREY M. BOWERS, SUPERVISOR

(Signature on File)
SCOTT MISTURE, ADVISORY COMMITTEE

(Signature on File)
S. K. SUNDARAM, ADVISORY COMMITTEE

(Signature on File)
NATHAN P. MELLOTT, ADVISORY COMMITTEE

(Signature on File)
ALASTAIR N. CORMACK, CHAIR, ORAL THESIS DEFENSE

ACCEPTED BY _____ (Signature on File)
DOREEN D. EDWARDS, DEAN
KAZUO INAMORI SCHOOL OF ENGINEERING

ACCEPTED BY _____ (Signature on File)
NANCY J. EVANGELISTA, ASSOCIATE PROVOST
FOR GRADUATE AND PROFESSIONAL PROGRAMS
ALFRED UNIVERSITY



Cy Twombly (1928-2011)
"Untitled"
1964 and 1984

ACKNOWLEDGMENTS

This work was supported by the United States Department of Energy, Office of Basic Energy Science through grants DE-FG02-10ER16128 and DE-FG02-08ER15929. NMR experiments described in this work were performed in the Environmental Molecular Sciences Laboratory, a national scientific user facility sponsored by the Department of Energy's Office of Biological and Environmental Research and located at Pacific Northwest National Laboratory. Sarah Burton and Andrew Lipton of Pacific Northwest National Laboratory's Environmental Molecular Science Laboratory provided assistance in the operation of the high-field NMR. Additional thanks to EMSL staff Bruce Arey for assistance with microscopy and Mark Bowden for assistance with X-ray diffraction. Computational collaboration with the group of R. James Kirkpatrick at Michigan State University has been invaluable; much thanks is owed for the guidance of R. James Kirkpatrick, and for the contributions of A. Ozgur Yazaydin including execution of molecular dynamics and some of the quantum chemical calculations; Dr. Andrey Kalinichev is thanked for his involvement in the original research proposal, for helpful discussions, and exemplary scientific wisdom. Thanks to the National Center for Supercomputing Applications for access to the Cobalt and Carbon clusters, and to the R. J. Kirkpatrick Group's in-house computational resources. Thanks to Geoffrey Bowers for assistance and teaching related to NMR spectroscopy, NMR data processing, and for writing the majority of NMR instrumental methods contained here. Richard Reeder from Stony Brook University kindly provided the atomic positions from the reverse Monte Carlo model from which many useful comparisons are derived. The Ph. D. committee at Alfred University has provided many useful discussions, and is thanked for their participation.

TABLE OF CONTENTS

	Page
Frontispiece.....	iii
Acknowledgments	iv
Table of Contents.....	v
List of Tables	vi
List of Figures.....	viii
Symbols and Abbreviations	xi
Abstract.....	xii
I INTRODUCTION	1
II LITERATURE REVIEW	11
A. Motivation: Role of Calcium Carbonates in Nature.....	11
B. Formation of Ion Pairs, Prenucleation Clusters, and Amorphous Carbonates	14
C. Behaviors of Magnesium in Carbonate Precipitation	22
D. Reference Phases in the Ca-Mg-CO ₃ -H ₂ O System	26
E. Crystallization	30
III METHODS	35
A. Synthetic Methods (Overview).....	35
B. Characterization Methods.....	39
C. Computational Methods.....	48
IV RESULTS AND DISCUSSION.....	57
A. CASTEP NMR Properties.....	57
B. Carbon (13) NMR.....	68
C. Calcium (43) NMR.....	72
D. Magnesium (25) NMR	86
E. Dolomite Crystallization	96
F. Next Steps and Future Work	103
V CONCLUSION.....	109
REFERENCES.....	110
APPENDIX.....	127

LIST OF TABLES

	Page
Table 1. Magnesium content of biogenic and synthetic carbonates. Pathway of precipitation and impurity exclusion kinetics during recrystallization give rise to tremendous variability between biological species. Intraspecies variability is not known but likely also depend on individual metabolic differences that are a function of local water temperature, turbidity, and water chemistry.	24
Table 2. Summary of Ca-Mg-CO ₃ -H ₂ O crystalline reference phases (with accepted mineral names). From inspection of unit formulae alone, one can observe the differential behaviors of Ca and Mg in the metal-carbonate-water system. For example, the diversity of polymorphs foreshadows the possibility for disorder, solid solutions, and mixed phase assemblages. The formulae of ikaite and lansfordite are similar to the simulated results of ion pair hydration structures. Mixed Ca-Mg compounds tend toward Mg-rich compositions. Mg-CO ₃ -H ₂ O compounds have a more continuous distribution of water contents than that of Ca-CO ₃ -H ₂ O compounds, reflecting the gradual dehydration kinetics of Mg-H ₂ O complexes.	30
Table 3. Labels of synthetic variables used throughout this manuscript. Note that these labels refer to the parent solution, while the compositional variable $x=[\text{Mg}/(\text{Ca}+\text{Mg})]$ and water contents (weight percent) refer to the solid composition.	36
Table 5. NMR and crystallographic data used in the correlation between Ca-O bond distance (Å) and isotropic chemical shift (ppm) for hydrous and anhydrous Ca carbonates. Our own CASTEP calculations give similar results to previous work by Bryce ^{173;174} . Mean Ca-O bond distances are taken from the literature with work on hydrates (monohydrate and ikaite) attributable to Swainson et al. ^{146;185} , vaterite to Wang and Becker ¹⁵⁰ , hydrated Ca ²⁺ to Politi et al. ^{34;56} , and ion pair to Di Tomasso and De Leeuw ⁹⁹ . Bold values highlight the data used in the correlation for determination of maximum bond distances.	67
Table 6. NMR and crystallographic data used in the correlation between Mg-O bond distance (Å) and isotropic chemical shift (ppm) for anhydrous and hydrous Mg carbonates. Our own CASTEP calculations differ substantially from certain results experimental results of Pallister et al. and MacKenzie and Meinhold ^{171;177} . Particularly the three site model for hydromagnesite (Table 4) is reduced to a two-site model for comparisons discussed within the text.	68
Table 7. Peak positions and line widths for the ACC samples in this study determined by fitting the resonances to single Gaussian functions, corresponding to spectra in Figure 13.	

*After subtraction of Lorentzian fit for calcite ingrowth. **After subtraction of Lorentzian fit for coexisting calcite and aragonite.	75
Table 8. Synthesis conditions and compositions of ACC of Figure 13.	75
Table 9. XAS-determinations of Ca-O bond distances and coordination numbers from natural samples of amorphous carbonates previously reported in the literature.	84
Table 10. Fit parameters of ikaite experimental NMR and ^{43}Ca CASTEP NMR	128
Table 11. Carbon (13) CASTEP NMR properties calculations for reference phases in the Ca-Mg- $\text{CO}_3\text{-H}_2\text{O}$ system. P-denotes conversion to a primitive cell (P1) symmetry. The relaxed symmetry constraints do affect the calculation.....	133

LIST OF FIGURES

	Page
Figure 1. A multiscale vision of carbonate nucleation (A-D), aggregation (E, F), and crystallization in the environment (G-I) draws from a vast and growing literature, experimental and computational studies, and from synthetic and natural systems. Ion pair hydration is studied by both polarizable MD of Ca-CO ₃ -6H ₂ O (A) ¹⁶ and AIMD of Mg-CO ₃ -4H ₂ O (B) ¹⁷ . Cluster formation and PNC simulations require larger simulations and make use of polarizable force fields (C) ¹⁸ and new force field development based on solvation enthalpies (D) ^{19; 20} . Reverse Monte Carlo (RMC) modeling of total x-ray scattering gave rise to a heterogeneous structural model (E) ²¹ and facilitates extended MD simulations of bulk ACC materials (F; this work). This work furthers our understanding of how organisms use calcium carbonate (G, H) and routes toward CO ₂ sequestration (I).	3
Figure 2. Polarizable MD simulation snapshot of PNC growth and ion attachment (A) having color-coded Ca ²⁺ ions that correspond with umbrella sampling free energies (B). This simulation demonstrates the absence of energetic barriers for ion attachment to the disordered particle. ¹⁸	15
Figure 3. “Water is the Key to Nonclassical Nucleation,” showing a snapshot from MD simulation of hydrated ion pair addition to a growing cluster (A) and free energies as a function of cluster size and hydration state (B). ^{19; 20}	18
Figure 4. Goodwin et al.’s (2010) reverse Monte-Carlo refinement of experimental total scattering data ²¹ of an ACC structure having ‘monohydrate’ composition (1a) and experimental XRD of indistinguishable materials (1b) that were produced using two different synthetic methods ¹¹²	21
Figure 5. Calorimetry of Amorphous Phases relative to anhydrous crystalline endmembers ¹⁰² that implies solid solution from $x = \text{Mg}/(\text{Mg} + \text{Ca}) < 0.5$ and a mechanical mixture of AMC ($x = 1.0$) and APMC ($x = 0.5$) when $x > 0.5$	34
Figure 6. Pulse sequence diagrams for various sequences used throughout the work including Bloch decay, Proton-Carbon decoupling, and the quadrupolar Carr Purcell Meiboom Gill (CPMG) sensitivity enhancement.	44
Figure 7. CASTEP NMR calculations make use of electron pseudopotentials that enable very high-level calculations of valence electrons and excited states.	49
Figure 8. The method of polyhedral averages identifies the coordination environment of each Ca ion (A; illustrated for a single Ca), and produces a single valued bond distance for each	

Ca ion's coordination environment (B). This type of averaging is appropriate for comparison to NMR data, which samples the mean coordination environment. . 56

Figure 9. The method of polyhedral averages is extended to the Goodwin et al. structure of ACC shown as ball and stick model A, and as polyhedral representation in B. The method of polyhedral averages was also applied to crystalline reference phases (calcite, Wang's vaterite, Kamhi's vaterite, monohydrocalcite, and aragonite). 56

Figure 10. CASTEP calculated ^{43}Ca -NMR parameter (absolute isotropic shielding) correlated with experimentally determined isotropic shifts (A); the correlation coefficient ($y = -0.8639x + 974.1$; $R^2 = 0.99931$) is a testament to the accuracy of the CASTEP code. Mean Ca-O bond distance is also correlated with ^{43}Ca -NMR isotropic chemical shifts and gives good results for the entire $\text{Ca-CO}_3\text{-H}_2\text{O}$ system. 57

Figure 11. CASTEP calculated ^{25}Mg -NMR parameter (absolute isotropic shielding) correlated with experimentally determined isotropic shifts (A; $-0.909922x + 511.591110$; $R^2 = 0.998324$). Mean Mg-O bond distance is poorly correlated with ^{25}Mg -NMR isotropic chemical shifts (B) and poorly correlated with the quadrupolar coupling constant because geometric factors are increasingly important when the NMR active nuclei have large nuclear quadrupole moments. The Hydromagnesite, 9 site is somewhat of an outlier because it is coordinated by two hydroxyl groups. 61

Figure 12. Carbon (13) NMR of amorphous carbonates and crystalline reference phases (A) and comparison of ACC, ACMC, and AMC to a mechanical mixing model (B). Arrow denotes the region of low-frequency mismatch between ACMC (green) and AMC (blue). This region of mismatch challenges the nano- phase separation model of ACMC $x < 0.5$ put forth by Radha et al. ¹⁰². ACC=amorphous calcium carbonate; CC=calcite; pD=stoichiometric protodolomite ($x=0.5$); Hm*=defective hydromagnesite; Hm=hydromagnesite; Cal-pD=calcian protodolomite ($x=0.47$); A=aragonite; ACMC=mixed magnesium calcium carbonate ($x=0.6$); AMC=amorphous magnesium carbonate ($x=1.0$). 69

Figure 13. Integration of experimental ^{43}Ca NMR with molecular dynamic and quantum mechanical computation for ACC and ACMC samples labeled according to synthetic conditions. The combined approach eases the limitations of either technique alone and forms the basis of a new multi-scale approach to NMR analysis. Arrows for MD results of reference phases indicates the degree of isotropic shift underprediction using the method of polyhedral averages. The dashed purple line is for polyhedrally averaged results of Kamhi's vaterite, as compared to Wang's vaterite in the solid purple line. CASTEP calculations are only performed for Wang's vaterite, although Kamhi's vaterite is observed by experimental NMR. 74

Figure 14. Logarithm of background corrected XRD patterns for ACC samples synthesized at PNNL after storage in ambient conditions for ~100 days. Unusual peak positions or relative intensities are denoted by * 78

Figure 15. TGA of samples associated with Figure 10. TGA of synthetic ACC indicating labile water contents ranging from 10-40 weight percent (<250°C), monohydrate decomposition (~210°C), and multi-stage decomposition of mixed Na, Mg, Ca carbonates (350-500°C).	81
Figure 16. Comparison of experimental NMR with results derived from models and X-ray Absorption Spectroscopy. Previously published mean Ca-O bond distances and coordination numbers for synthetic and naturally occurring amorphous carbonates determined by X-ray Absorption Spectroscopy (Table 9) ^{31; 49; 52; 53; 56; 140; 192}	85
Figure 17. CASTEP-SIMPSON simulated reference phases in the Mg-CO ₃ -H ₂ O system, with and without proton equilibration under static conditions at 20T.	87
Figure 18. CASTEP-SIMPSON simulated reference phases in the Mg-CO ₃ -H ₂ O system, with and without proton equilibration under MAS (10 kHz) conditions at 20T.....	88
Figure 19. Static ²⁵ Mg NMR spectra of synthetic phases in the Mg-CO ₃ -H ₂ O system compared to proton-only equilibrated CASTEP NMR reference spectra.	92
Figure 20. MAS (10 kHz) ²⁵ Mg NMR spectra of synthetic phases in the Mg-CO ₃ -H ₂ O system compared to proton equilibrated CASTEP NMR reference spectra.	93
Figure 21. Logarithm of XRD Intensities for samples relevant to Mg-NMR spectra. Vertical lines trace the features of dolomite (D) to highlight differences between protodolomite (pD), calcian protodolomite (cal-pD) and hydromagnesite (Hm).	95
Figure 22. TGA and DTA from RT to 900°C for AMC, ACMC, and protodolomite (pD). DTA can not be quantitatively converted to the energy of the transition because of unknown sample densities and heterogeneous sample contact with the platinum electrode during shrinkage and cracking.	97
Figure 23. SEM of the ACMC precursor, protodolomite (pD+Hm), and calcian-pD and company. Scale represents 1 micrometer in all images. The amorphous particles of ACMC (x=0.6) are aggregates that are <100nm in diameter. Proto-dolomite (pD) has dumbbell shaped floret structures with rods on the order of 100 nm thickness however the structural relationship between pD and hydromagnesite is not evident in these images. The multiphase nature of the calcian protodolomite (cal-pD) is clearly evident from the different morphologies, including aragonite (A) and hydromagnesite (Hm).	99
Figure 24. The asymmetric site in lansfordite provides an analogy to protodolomite. .	101
Figure 25. SAXS raw data for several samples ACC (x~0), ACMC (x~0.6), and protodolomite (pD, x~0.6) as compared to crystalline calcite and glass and air backgrounds.	

Backgrounds are not explicitly subtracted from the sample data. The small angle scattering becomes convoluted with scattering from the primary beam around 0.2 degrees.	105
Figure 26. Porod plot of SAXS data ACC ($x \sim 0$), APMC ($x \sim 0.6$), and protodolomite (pD, $x \sim 0.6$) as compared to crystalline calcite and glass and air backgrounds. Backgrounds are not explicitly subtracted from the sample data.	106
Figure 27. ^1H - ^{13}C CPMAS spectra from 20.0 T for ikaite -5°C . Ikaite ^{13}C - ^1H CP resonance is well-fit with single Lorentzian functions centered at 168.2 ± 0.1 ppm. Heating the sample at 60°C was sufficient to remove all water from the sample (shown by the lower trace).....	130
Figure 28. ^{43}Ca MAS NMR spectra and SIMPSON simulations of the ikaite NMR resonance at 20.0 T. Synthetic ikaite specimen is colored blue and the simulation results red. Several spinning sidebands are not shown. The sample exhibited a minute quantity of calcite near 21 ppm that is not shown.	130
Figure 29. TGA and DSC of ikaite thermal decomposition showing a two-stage dehydration of six stoichiometric water molecules, absence of recrystallization event (no exothermic event), and decarbonation temperature (698°C) consistent with perseverance of an amorphous phase at high temperature.....	131
Figure 30. SEM of ikaite crystals displaying rhombohedral habit and onset of decomposition (cracking and vaporization) under SEM conditions. There is a 100 micron scale in all micrographs.....	132

SYMBOLS AND ABBREVIATIONS

6HC	ikaite (calcium carbonate hexahydrate)
A	aragonite
ACC	amorphous calcium carbonate
ACMC	amorphous calcium magnesium carbonate
AIMD	ab initio molecular dynamics
AMC	amorphous magnesium carbonate
AP	activity product ($\approx Q$)
ALS	advanced light source
C_i	cluster (of non-specific structure)
CC	calcite
CP	cross polarization
CPMG	Carr-Purcell-Meibaum-Gill
DRIFTS	diffuse reflected infra-red Fourier transform spectroscopy
EDS	Energy dispersive spectroscopy
EXAFS	extended x-ray absorption fine structure
FF	force field
Hm	hydromagnesite
INS	inelastic neutron scattering
IP	ion pairing
IR	infra-red
MAS	magic angle spinning
MC	Monte Carlo
MD	molecular dynamics
MHC	monohydrocalcite
NMR	nuclear magnetic resonance
pD	protodolomite
PNC_i	prenucleation cluster
Q	reaction quotient
QM-DFT	quantum mechanic- density functional theory
RMC	reverse Monte Carlo
SANS	small angle neutron scattering
SAXS	small angle x-ray scattering
SEM	scanning electron microscopy
T	temperature
t	time
TGA	thermal gravimetric analysis
WAXS	wide angle X-ray scattering
WDS	Wavelength dispersive spectroscopy
XANES	X-ray absorption near edge structure
XAS	X-ray absorption spectroscopy
XRD	X-ray Diffraction
XRF	X-ray fluorescence

ABSTRACT

The aqueous chemistry, precipitation, and crystallization of metal-carbonates comprises a vast field of research that underlies the urgency of CO₂ sequestration, ocean-acidification, and biomineralization. The results of recent experimental and computational studies suggest that amorphous calcium and magnesium carbonates are precipitated from supersaturated aqueous conditions by non-classical aggregation of ion pairs, dimers, dynamically-ordered-liquid-like-oxypolymers (DOLLOPS), and prenucleation clusters (PNCs). We present the first high field (20 T) ⁴³Ca and ²⁵Mg NMR studies of amorphous calcium-magnesium carbonates (ACC, ACMC, AMC) materials. Direct integration of computational techniques with experimental NMR provides a novel step forward toward multi-scale integration of computational and experimental techniques. Supporting information is derived from X-ray diffraction (XRD), thermogravimetric/differential thermal analysis (TGA-DTA), and scanning electron microscopy – energy dispersive spectroscopy (SEM-EDS) and provides important comparison to the bulk structures and composition.

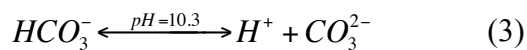
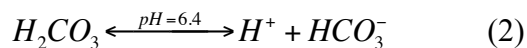
High field NMR of amorphous carbonates demonstrates that amorphous carbonates contain various types of local disorder, but does not corroborate the theory of polyamorphism nor nano scale phase separations postulated by other workers. Carbon (¹³C) NMR of ¹³C-enriched materials indicates a degree of Ca-Mg solid solution in ACMCs, as ACMC ¹³C resonances cannot be adequately reconstructed from the pure ACC and AMC ¹³C resonances. However, with increasing Mg-content (and therefore H₂O content) ¹³C NMR resonances are strongly influenced by water-carbonate hydrogen bonding, shifting to lower resonance frequency and broadening. The ¹³C-NMR are well-fit with single Gaussian distributions, suggesting that two-phase models of ACMCs are not required to explain our ¹³C NMR observations. Proton-carbon cross polarization indicates that there is a H population proximal to carbonate groups for all amorphous phases. ⁴³Ca NMR yields line shapes that span the resonance frequency range of all known crystalline calcium carbonate polymorphs and is well fit with a single Gaussian distributions. ⁴³Ca NMR does not support a theory of polyamorphisms, but rather suggests an unstructured, continuous distribution of local environments that is unlike any specific crystalline phase. The mean ⁴³Ca chemical shifts vary 0.77 ppm from compositions x=0 to 0.5 [x=Mg/(Mg+Ca)], demonstrating that Mg²⁺ has very little influence on the molecular-scale ⁴³Ca environment in ACMCs. Through integration of quantum mechanical calculations, classical MD, and NMR we ascertain a maximum mean Ca-O bond distance in our ACCs/ACMCs of 2.45 ± 1 Å that is independent of composition. Unlike the indistinguishable local calcium environments, ²⁵Mg NMR of amorphous material gives evidence for several distinct overlapping quadrupolar line shapes. These sites do not generate NMR resonances that are perfect matches for known crystalline polymorphs of magnesian carbonates and extend toward lower resonance frequencies far beyond the range of known equilibrium analogs. By comparison to the range of reference phases, the low frequency singularities of ACMC-AMC resonances are consistent with some population of Mg-O bond distances greater than 2.10 Å and/or some fraction of sites with high coordination numbers (up to 8). The local Mg environment of a protodolomite crystallization [x=Mg/(Mg+Ca)=0.6] exhibits ²⁵Mg NMR parameters most similar to the asymmetric Mg²⁺ coordination environment of lansfordite [Mg(CO₃)₂(H₂O)₄]²⁻ or huntite. Although H-C cross polarization indicates no H-bonding with carbonate the XRD gives not long-range indications of huntite. The large effective radius of strongly hydrated Mg in the protodolomite likely provides a driving force for cation ordering in dolomite.

INTRODUCTION

Calcium carbonate buffers the ocean, the atmosphere, the soil, and our bones. Diverse marine organisms display a masterful control of calcium carbonate's form and crystallization that has eluded generations of scientists. Biomimetic engineering has made great progress in the recent decades^{1; 2; 3; 4; 5; 6}, but these man-made materials pale in comparison to the elegance, versatility, and durability produced by certain single-celled organisms. In addition to their apparent mastery of carbonate material chemistry, the ranks of calcareous marine organisms constitute a vital component of the ocean food web as coral reefs, bivalves such as clams and oysters, and microorganisms such as coccolithophores and foraminifera. By the end of the century calcareous marine organisms will suffer global decline as a direct consequence of exponential growth in CO₂ emissions and subsequent ocean acidification^{7; 8; 9; 10}. In the mass media CO₂ is better known for its greenhouse activity, whereby, in positive feedback with the greenhouse activity of water vapor, the ice caps (north, then south) are also predicted to vanish by the end of the century¹¹. Reductions in sea ice formation is proportional to decreases in bottom water formation, and is forecasted to effectively shut off the "great conveyor belt" of thermohaline ocean circulation¹². Cold upwelling zones are highly productive regions of the ocean that will concomitantly wither and no longer recycle nutrient supplies to the surface ocean. Thus, the loss of CaCO₃ based marine organisms very likely (albeit indirectly) precedes the collapse of ocean circulation and ocean productivity. Stagnation of the ocean circulation further perturbs the thermal balance between ocean, atmosphere, and inland climates in ways that will lead to even greater mean temperatures and raises great uncertainty regarding the habitability and habitable area for land-dwellers as well. Geological CO₂ sequestration is an essential and urgent

mitigation technology for CO₂ emissions that hinges upon guaranteed stability of nonequilibrium carbonate deposits^{13; 14; 15}. To better understand and predict the time evolution of CO₂ sequestrations, a multi-scale model of carbonate precipitation far from equilibrium must include every aspect from molecular-scale interfacial reactivity, to pore-scale processes, to geological scale structural evolution (Figure 1). Although the technological and chemical challenges of CO₂ sequestration are indeed great, they are not so difficult as large-scale political and economic cooperation that is prerequisite for drastic reductions in CO₂ emissions (or alternatively increase in sequestration). Admittedly with a myopic air characteristic of a chemist, this thesis indulges in the molecular scale details of an urgent global problem.

Calcium carbonates have been greatly studied as a buffer of natural waters and solids that form from aqueous environments:



In the above chemical reactions, atmospheric carbon dioxide dissolves in seawater and through formation of short-lived carbonic acid, CO₂ enters the polyprotic carbonate equilibrium.

Transformations to bicarbonate and carbonate ions are relatively slow, and in biological systems there are specific enzymes (namely carbonic anhydrase) that are responsible for catalyzing the formation of CO₃²⁻ at biologically suitable pH.

The solid form of calcium carbonate has some unusual chemical behaviors, namely, retrograde solubility and stable supersaturations that provided early hints that aqueous behaviors of calcium carbonate did not adhere to the classical theories of nucleation and precipitation.

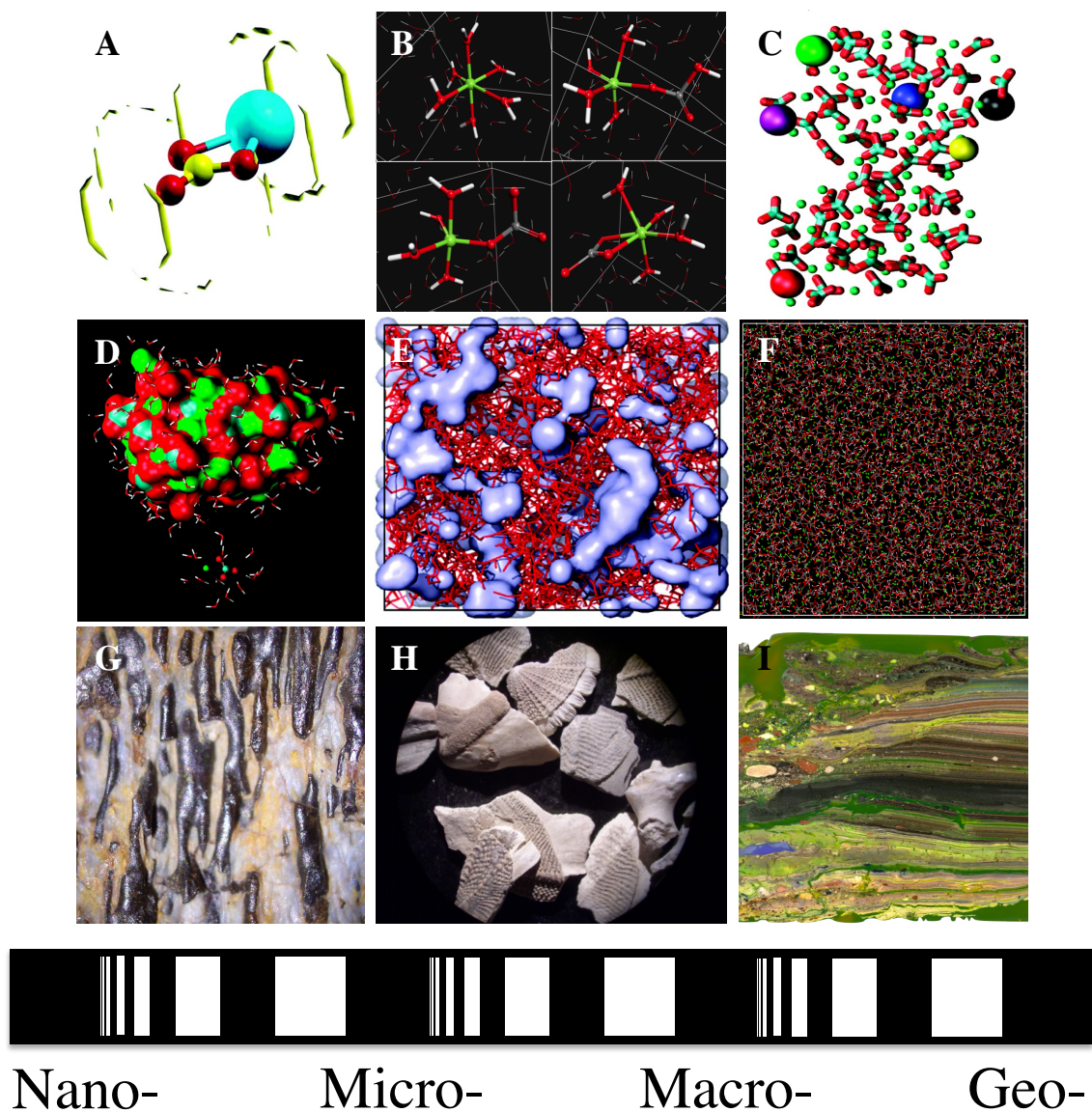


Figure 1. A multiscale vision of carbonate nucleation (A-D), aggregation (E, F), and crystallization in the environment (G-I) draws from a vast and growing literature, experimental and computational studies, and from synthetic and natural systems. Ion pair hydration is studied by both polarizable MD of $\text{Ca-CO}_3\text{-6H}_2\text{O}$ (A)¹⁶ and AIMD of $\text{Mg-CO}_3\text{-4H}_2\text{O}$ (B)¹⁷. Cluster formation and PNC simulations require larger simulations and make use of polarizable force fields (C)¹⁸ and new force field development based on solvation enthalpies (D)^{19;20}. Reverse Monte Carlo (RMC) modeling of total x-ray scattering gave rise to a heterogeneous structural model (E)²¹ and facilitates extended MD simulations of bulk ACC materials (F; this work). This work furthers our understanding of how organisms use calcium carbonate (G, H) and routes toward CO_2 sequestration (I).

More recently experimental and theoretical chemists have joined forces to solve the molecular scale nature of calcium carbonate's non-classical nucleation pathways that include a burgeoning structural hierarchy of stable ion pairs (IP) ¹⁶, dynamically-ordered liquid-like oxyanion polymers (DOLLOP) ²², clusters (C_i) and prenucleation clusters (PNC_i) ^{18; 19; 20; 23}, and aggregations of these states to form amorphous calcium carbonate (ACC) ²¹:



Although natural calcium carbonates may exist in relatively pure forms, natural waters are rarely pure and the matrix ions have a great influence on the nucleation pathways. A diversity of common "spectator" ions (viz. Na⁺, Mg²⁺, Sr²⁺, H⁺, K⁺, PO₄³⁻, SO₄²⁻, OH⁻, Cl⁻) are highly concentrated in seawater, saline groundwater, industrial wastes, and intracellular environments. Although these species are not specified in the preceding reactions (reaction 1-8), ostensibly these 'spectators' moderate the nucleation kinetics of calcium carbonate and may chemically substitute or become trapped within the solid through physical processes of aggregation and/or chemical exclusion of impurity substitutions upon crystallization. Through these various mechanisms, the matrix of spectators has a significant influence on the crystallization pathways and evolution of CaCO₃ polymorphs. In very highly concentrated brines (under evaporative conditions) this entire family of abundant alkali- and alkaline earth-metals in combination with anions and oxyanions can form many mixed-species crystalline phases, solid-solutions, and mixed-phase assemblages, a review of which is beyond the scope of this introduction. The existence of amorphous precursors are also well studied in phosphate ^{24; 25}, sulfate ²⁶, arsenate ²⁷,

and other oxyanion-bearing materials. The continuity of solid solutions and constitution of multi-phase assemblages are affected by similar non-classical precipitation pathways and the existence of amorphous intermediates analogous to those of calcium carbonate. The nonclassical intermediate states escalate the complexity of phase separations and crystal nucleation for this entire family of species--leading to outcomes that cannot be predicted by classical thermodynamics. Although the existence of non-classical pathways is recognized in many compositional fields this thesis will restrict its exploration to the precipitation of amorphous Ca-Mg carbonates from saline solutions rich in NaCl similar to modern seawater composition.

Unanswered questions in regard to calcium-magnesium carbonate chemistry are decades old^{28; 29; 30} and the most common questions are centered on geological occurrences of Ca-rich carbonate minerals, biomineral forms of predominantly Ca-carbonates, and crystal polymorph selection under a variety of conditions. Since most of sedimentary processes on earth occur in the ocean, these questions are dominantly framed within a saline, seawater-like matrix. Due to the similar chemical behaviors of Mg and Ca, and due to a 5:1 ratio of Mg to Ca in seawater, Mg is the most significant impurity in relation to precipitation of calcium carbonates in most natural environments. It is known that Mg^{2+} stabilizes ACMCs, and the mechanism behind Mg^{2+} stabilization of the amorphous carbonate is a relatively recent question^{31; 32; 33; 34; 35} that bears directly on long-standing issues in geochemistry such as the mechanisms of massive geological dolomite $CaMg(CO_3)_2$ formation^{36; 37; 38; 39; 40; 41; 42; 43} and of aragonitic biomineralization^{44; 45}. Both dolomite and bio-aragonite formation may enhance our abilities to sequester CO_2 using quasi-natural mechanisms. Thus, in addition to amorphous calcium carbonate (ACC) this work will especially consider the related behaviors of endmember amorphous magnesium carbonate (AMC) and diverse intermediate compositions of amorphous calcium-magnesium carbonate

(ACMC). Over the last decade the debate has shifted from the thermodynamic arguments of equilibrium to the realm of disequilibrium and kinetics, and this investigation into the behaviors of the amorphous carbonate phases are part of a recent movement to understand non-equilibrium processes. There are currently outstanding questions that surrounding the structural evolutions of calcium-magnesium carbonates in solution prior to precipitation, whether the disposition for crystallization pathway is predetermined by the prenucleation cluster (PNC) formation conditions or dependent on subsequent processing and storage, whether the forms of these intermediate states are similar or dissimilar to known equilibrium polymorphs, and how the distribution of states i at all scales is affected by synthetic or natural conditions. The issues that surround the solution chemistry of calcium carbonate nucleation and PNCs have been recently reviewed, however the discussion is skewed toward a theory of prestructured polyamorphisms that are framed in terms of equilibrium crystalline polymorphs⁴⁶. The use of the word “polyamorphisms” in the carbonate literature has most commonly been interpreted as having local domains similar to crystalline polymorphs but aggregated in a disordered state, however in this work we will use the term more generally to denote amorphous materials of identical composition that may differ in any physical property. Polyamorphisms at non-local length scales have hardly been considered in the recent carbonate literature but this concept is observed in other amorphous materials that are subject to nano-scale phase separations, network connectivity, and inhomogeneous topologies. Beyond biomineralization, geological CO₂ sequestration has added a new and dynamic, multi-element matrix for consideration--specifically the dissolution products of host-rock silicates upon injection of acidic supercritical CO₂^{47; 48}. The precipitation pathway and mineralization kinetics during CO₂ sequestration is fundamentally similar to biomineralization, and it is our hope that regardless of the specific solution matrix

composition that principals and techniques of general relevance will emerge from these studies of ACC-AMC phases. However, quantitative treatment of kinetics in multi-element, heterogeneous media quickly reaches an intractable level of complexity across scale, as one must necessarily track the details of interfacial reactivity, nanoporous and mesoporous flow, and network topologies that evolve in time and space. To approach such chemical challenges, rapid development is now occurring at the interface of experiment and theoretical computations-- limited by resolution and scale, respectively. Thus the critical steps forward require integration of experiment and computation in a manner that overcomes the intrinsic limitations of each. In this work we present a new approach for comparing the results of experimental nuclear magnetic resonance (NMR), with molecular dynamics (MD) and quantum mechanical calculations.

This work offers the first insights to calcium-magnesium amorphous carbonates through NMR of calcium (^{43}Ca) and magnesium (^{25}Mg). The NMR of ^{43}Ca and ^{25}Mg is only recently afforded by the availability of increasingly large superconducting magnets, sophisticated electronics, and (in the case of ^{43}Ca) expensive isotope enrichment. Nuclear magnetic resonance is established by net alignment of nuclear spins in an NMR-active isotope with the field when exposed to a very strong external magnetic field, and chemical information on the 1-4/5 bond scale can be obtained by the perturbation of the thermal equilibrium spin system using a pulse of current applied to a solenoid that surrounds the sample. The relaxation of the perturbed nuclear spins back to thermal equilibrium generates a tiny flow of electrical current in the coil that decays exponentially, and this current can be amplified, recorded, and Fourier analyzed to generate NMR spectra. The differential perturbation-relaxation behaviors of nuclear spins due to the specific types of magnetic shielding and deshielding established by different local environments often allows deconvolution of distinguishable local structural environments that

can be correlated to either molecular-scale structure or dynamic behavior in the material of interest. Even with the latest high-field magnets and electronic amplifiers, the NMR experiments of certain nuclei remain very time consuming or even impossible. In the case of the least sensitive NMR-active isotopes, many thousands of pulse-relaxation experiments are co-added to produce sufficient signal to noise ratio for detailed structural or dynamic analysis--if any signal is obtained at all. ^{43}Ca and ^{25}Mg NMR are extremely difficult to observe using NMR technique due to combinations of low gyromagnetic ratios (γ), low natural abundances, and the observation of relatively large quadrupolar coupling constants (C_Q) in many materials. The low- γ nuclei are inherently insensitive because the nuclear spin dipole is small with respect to the nuclear spin angular momentum, thus net alignments of nuclear spins are relatively small and the perturbation pulse is relatively inefficient at established spin coherence. The limitations arising from low natural abundance of NMR-active isotopes can be overcome through brute-force isotope enrichment (used here for ^{43}Ca NMR) or through various pulse sequences designed to boost sensitivity (used here for ^{25}Mg NMR). Another routine technique in solid-state NMR spectroscopy for improving sensitivity is magic angle spinning (MAS), which improves resolution and sensitivity for solid samples by eliminating effects on the resonance line shape due to interactions that depend on the "magic" angle (54.74° ; the value giving a null result in the second Legendre polynomial). Any nucleus having a non-integer spin state greater than $1/2$ (i.e. $3/2, 5/2, 7/2, \dots$) generates a signal from a residual second order quadrupolar interaction that cannot be completely canceled through magic angle spinning (MAS). These second order quadrupolar interactions causes a broadening of the NMR line shape and therefore reduced overall intensity. Because of the preceding difficulties, most of the previous knowledge regarding local coordination environments of metals in alkaline earth metal carbonates has come

from Ca- and Mg-EXAFS^{34; 49; 50; 51; 52; 53; 54; 55; 56; 57; 58; 59; 60} but these techniques are considered indirect/model dependent, since the analysis and processing of EXAFS data is necessarily fixed according to the analysis of reference phases. Although reference phases provide important comparison for NMR interpretation, the choice of reference does not alter the information contained within the unknown's NMR spectra. Additionally, NMR of light elements fills a gap where XAS techniques are inherently insensitive. Thus, in spite of the difficulties inherent to NMR, it provides an independent validation of the EXAFS local structure determinations and fills complimentary needs that are not possible through other structural techniques.

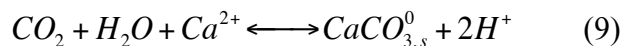
To maximize the information that can be extracted from the NMR results, this work incorporates a direct integration of experiment with computation across several length scales, through quantum mechanical calculations of NMR properties of crystalline reference phases (CASTEP NMR), though use of molecular dynamic (MD) simulations of crystalline reference phases and amorphous phases, and through NMR spectral simulation of crystalline reference phases under the influence of various instrumental parameters and fundamental interactions (SIMPSON). The quantum mechanical calculations of NMR properties for crystalline materials has become only recently possible and reliable through development of quality atomic pseudopotentials^{61; 62} that offer both efficiency and accuracy for large elements. Improved parallelization of QM-DFT algorithms exponentially decrease the necessary run time of these calculations on large supercomputers. Furthermore, graphical user interface (GUI) softwares like Materials Studio (Accelrys) have made quantum mechanical and molecular dynamic calculations practically accessible without the need for user knowledge of computer programming languages--a seminal advance in the popularization of computational chemistry techniques. Although molecular dynamics contains no nuclear information, nor any electronic

information, MD contains molecular scale information regarding bond distances, coordination number, nearest neighbor, second nearest neighbor, coordination geometry, symmetry, etc., that externally influence the ensemble of nuclear spins nested within each atomic representation. These integrating variables can be combined for qualitative interpretation of NMR spectra and through empirical relations with the fundamental NMR properties derived from the CASTEP NMR calculations. The results of CASTEP NMR properties calculations can be further utilized within SIMPSON⁶³, a bulk-scale spectral simulation software that is useful for addressing the affects of instrumental parameters on the observed/theoretical NMR spectrum . The combined experimental/computational approach facilitates peak assignments for unknown phases; it allows cross calibration of independent methods and may lead to improvement of MD force field development; and it improves the confidence of interpretations through visualization and model rendering, permitting analysis of otherwise intractable problems in materials chemistry, geochemistry, biochemistry, and many other fields.

LITERATURE REVIEW

A. Motivation: Role of Calcium Carbonates in Nature

Carbonate mineralization plays a central role in the buffering of carbon dioxide and acid, and in the transport of metals (viz. Ca). as illustrated by the sum of reactions 1-4 (reaction 9),



Anthropogenic CO₂ disrupts the equilibrium of reaction 9, driving the acidification of the ocean and a corresponding decline of CaCO₃-based life (coral, foraminifera, coccolithophores, bivalves, etc.)¹⁰. Calcareous organisms provide a substantial basis of the ocean food chain in both caloric quantities and physical substrates (i.e. coral reefs). It is predicted with high confidence that the ocean will be largely uninhabitable for calcareous organism within this century unless CO₂ emissions are dramatically reduced⁷. Yet mitigation of ocean acidification is very costly^{6; 32; 64; 65; 66; 67; 68} and may require large-scale capture and geologic sequestration of CO₂ as supercritical fluids.

A fundamental knowledge of amorphous carbonate nucleation and crystallization (discussed briefly in the introduction) is an essential component of long-term stable carbon sequestration^{13; 69} and would simultaneously benefit the efficiency and predictability enhanced oil recovery operations with supercritical CO₂. On short timescales, carbon is sequestered physically as supercritical fluids that may be trapped geologically beneath impermeable formations like clay or tight shale. The rates of upward migration and short-term stability are highly dependent on temperature, pressure, host-lithology, and rock mechanics. Sequestration

research has also led to advanced physical/structural percolation models and is one driver of development of multiscale, hybrid transport models^{13; 70; 71}. However physically sequestered fluids are bound to migrate upward along faults and fissures in the earth. Earthquakes and other geological instabilities (which are currently unpredictable) could lead to spontaneous and rapid migration to the surface where localized emissions of CO₂ may simply asphyxiate the entire locality. Outgassing eruptions of CO₂ present considerable risk (and are known to be deadly from natural CO₂ eruptions) prompting government agencies to seek 10,000-year guarantees for stable supercritical carbon dioxide sequestration projects¹⁴. On very long timescales (hundreds to thousands of years) the conversion of supercritical CO₂ fluids to carbonated minerals (CO₂ mineralization) will provide the most reliable form of sequestration. Supercritical CO₂ fluids are highly acidic and will dissolve much of the host rock mineralogy^{13; 15; 72; 73}. As the CO₂ and soluble elements are dissolved into a brine-like media one expects the eventual neutralization of the fluids and carbonate mineralization. The kinetics of host-rock dissolution and precipitation under deep subsurface conditions remains a subject of active investigation^{47; 72; 74}. There are also field scale injection study sites in several locations that have been chosen for stable, high-volume structural traps (porous sandstone)⁴⁸ or because of their potential to catalyze mineralization (deep basalts of Iceland)⁷⁵.

In an effort to address our modern climate change, earth scientists look to the past. The study of biogenic carbonate sediments^{29; 76} has long been central to paleoclimatic reconstructions. Ideally, the concept of a chemical proxy for temperature, pressure, or process composition relies on a mechanistic understanding of trace element or isotope fractionation factors as a function of the variable of interest. Practically and most commonly, geochemical proxies are based on empirical calibrations for an isolated variable under static boundary

conditions. The fidelity of such a proxy is only valid so long as the natural sample conforms within the synthetic/experimental/field boundary conditions that give rise to the empirical correlation of the calibration. This opens a possibility for misinterpretation when unforeseen variables are intrinsically included in the correlation. Furthermore, interpretation of proxy data derived from empirical models are subject to additional limitations that arise from the statistical correlation coefficients and propagation of error during model development in addition to the chemical-analytical precision of the empirical data. Through increasingly detailed mechanistic understanding of chemical [and isotopic] fractionation processes it is often possible to deconvolute simultaneous, independent processes that give rise to the observed correlation and improve the fidelity and sensitivity of the paleoproxy. The amorphous phases (ACC, APMC, and AMC) are undoubtedly intertwined with biomineralization processes and the carbonate-based paleoproxies⁷⁷, including trace element and isotope thermometry⁷⁸, reconstruction of seawater compositions and redox state, control over the amount and identity of the crystalline calcium carbonate polymorphs in a formation, understanding present and past biological mineralization processes^{79; 80}, and sedimentary diagenesis^{81; 82}. Recent studies in the group of Donald DePaolo has demonstrated that the ACC precipitation pathway minimizes the aqueous-solid isotope effects of the metal ion (viz. Ca^{2+} , Mg^{2+})^{78; 80; 83}--presumably because there is only a small isotope fractionation during cluster formation, and no isotope effect during aggregation of carbonate clusters and effectively closed-system crystallization within a condensed phase. The 'vital effects' were formerly a theoretical dumping ground for unexplained deviations between inorganic carbonate mineralization experiments and biogenic carbonates produced under comparable conditions^{35; 84}. However it is now known that various calcareous organisms do make use of unique, species-specific mineralization pathways by using specialized organic

matrix^{44; 85; 86; 87; 88} and an amorphous precursor^{64; 80; 89; 90; 91} however there is much to be learned about the molecular-level mechanisms. Thus, the trace element (or isotope) fractionation observed in the final crystalline product is coupled to the structural pathway of ACC precipitation, rates of transformation during biological processing, and the degree to which biomineralization process is open or closed. Thus, a molecular-scale understanding of all intermediate states, details of organism-specific processing, and the metabolic-kinetic connections are necessary to make *a priori* corrections for vital effects and deconvolute the influence of these effects with external variables such as seawater temperature and composition.

Calcium carbonates (and ubiquitous carbonate substitution in phosphates, sulfates, and hydroxides) play a general role in acidic environmental remediation⁹², maintains biologically suitable pH in a wide variety of systems³¹, and buffers tooth and bone tissues⁹³. The pH of CaCO_3 in equilibrium with HCO_3^- ranges from about 7 to 10, which brackets the range of most natural waters, blood, and intracellular environments—thus the importance of the carbonate buffer to life can not be understated. Bones and teeth are dominantly phosphatic but contain up to 30% carbonate substitution in local domains⁹⁴. Bioactive glasses have initial pH values near 6-7 and carbonation of the dissolution products is an important transformation that renders solid products at suitable pH for bioactivity and osteogenesis^{95; 96}. Ongoing research in this direction may reveal new pathways to reduce implant rejection and to increase the rates of transformation of engineered bone and tooth replacement/repair materials^{87; 97; 98}. Nucleation processes, amorphous phases, and their crystallization are broadly relevant in nature and technology; successful development of these applications relies on a bottom-up approach that integrates the latest computational and analytical technology.

B. Formation of Ion Pairs, Prenucleation Clusters, and Amorphous Carbonates

The multi-scale nature of the amorphous carbonate formation and transformation is evident in the literature. Unlike classical nucleation theory, where precipitates form by growth of crystalline nuclei, CaCO_3 condensation is known to include stable ion pairs (reaction 5)¹⁶, dimers and small clusters (reaction 6)⁹⁹, DOLLOPS²², and PNCs (reaction 7)^{18; 19; 20; 23; 46}. These states coexist in solution prior to visible precipitation of ACC (reaction 8). This pathway is preferred over classical nucleation because these non-crystalline states can grow larger with virtually no energetic barrier¹⁸ (Figure 2).

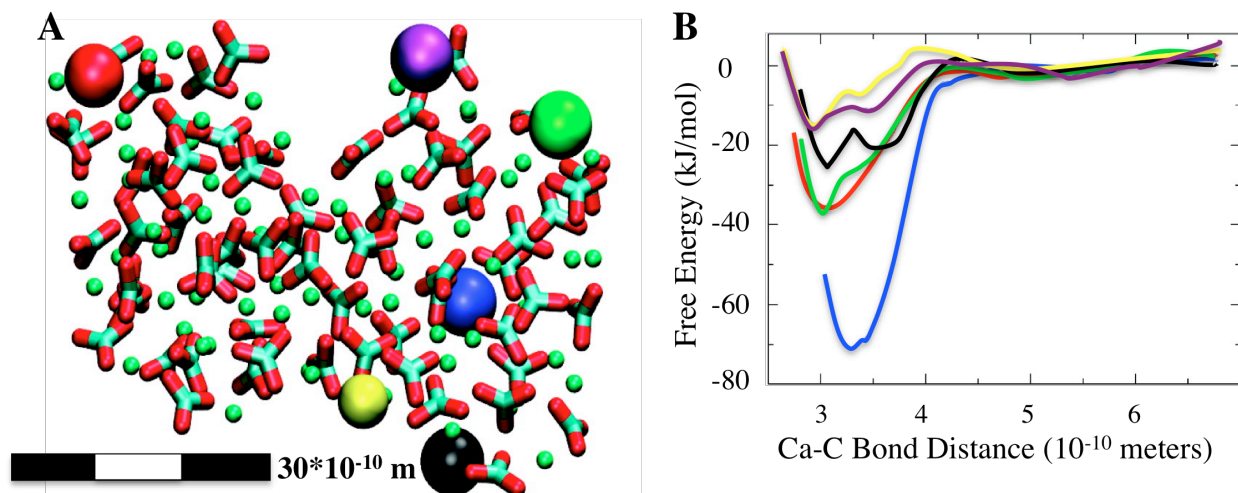


Figure 2. Polarizable MD simulation snapshot of PNC growth and ion attachment (A) having color-coded Ca^{2+} ions that correspond with umbrella sampling free energies (B). This simulation demonstrates the absence of energetic barriers for ion attachment to the disordered particle.¹⁸

The CaCO_3 ion pair is long lived in the neutral-basic pH regime. Workers of the Parrinello Group used polarizable molecular dynamics (MD) modeling of $\text{Ca}^{2+}\text{CO}_3^{2-}$ ion pairing in dilute conditions to show that the ion pair is strongly associated and coordinated by six H_2O molecules¹⁶. These authors argue that ion pair hydration is related to the $\text{CaCO}_3 \cdot 6\text{H}_2\text{O}$ (ikaite) crystalline structure, but upon detailed inspection, the water dynamics of ion pair hydration bears no

resemblance to dynamics of water in ikaite ¹⁶. In slightly acidic regimes (pH 6-7) the bicarbonate species is also known to engage in ion pairing and ion pair dimerization behaviors with calcium, but bicarbonate forms are more labile (H-bonding more strongly with H₂O solvent) and do not grow so large as the carbonate clusters. Quantum mechanical density functional theory (QM-DFT) calculations predict a variety of stable ion-pair dimers $\text{Ca}_x(\text{HCO}_3)_y(\text{H}_2\text{O})_x$ ⁹⁹ having shallow energetic barriers between various conformations of the structures. Under increasingly basic pH conditions the bicarbonate deprotonates to carbonate and the aggregation states of calcium carbonate become increasingly large. Most recently, molecular dynamic computational studies lead to the 'discovery' of DOLLOPS, which are $(\text{Ca}^{2+}\text{CO}_3^{2-})_n$ polymeric structures produced at higher pH values in a fashion similar to the dimerization of HCO₃. DOLLOPS are yet another topological pathway between the ion pair and PNCs²². At even higher pH /CO₃²⁻ supersaturation, the concentration of DOLLOPS increases, causing a higher collision probability for these Ca²⁺/CO₃²⁻/H₂O structures that ultimately leads to the formation of PNCs. At some threshold value of supersaturation, PNC aggregation yields solid precipitates of amorphous carbonate. Given the rapidly growing number of identified prenucleation states, one may hypothesize that these are in actuality various snapshots of a process continuum having a pot-holed type energy landscape with several shallow energy minima with respect to ambient kT. Ostensibly, it is possible that these states coexist, transform to one another, and equilibrate at some particular compositional ratio depending on the conditions (however this degree of control has not yet been realized by neither experimental nor computational approaches). One recent study has related the hierarchy of states to the process of spinoidal decomposition ¹⁰⁰, however, further distinctions must be made regarding the state reversibility and fractal emergence that are not typical of other spinoidal decompositions.

Prenucleation clusters were first postulated through experimental work²³, and have been extensively studied via computational approaches since that time^{20; 22; 23; 55; 73; 100; 101; 102; 103; 104; 105; 106; 107; 108; 109; 110}. Gebauer et al. observed evidence of pre-nucleation clusters via robotic titration methods, and using dynamic light scattering (DLS) and analytical ultracentrifugation reports observing a ~2 nm cluster with the approximate composition of $70\text{Ca}70\text{CO}_3$ prior to visible ACC precipitation²³. It remains undetermined by both laboratory experiment and computational studies if the ‘70-cluster’ represents a well-defined energy minimum across a wide range of conditions or if it is an artifact of specific saturation and matrix conditions. More detailed mechanistic insight into PNC formation comes from the MD work of Tribello et al. that tracks the free energy of Ca ions during their approach and attachment to emerging PNCs, leading to PNC growth¹⁸. They find that the disordered PNC particle presents little energetic barrier to an approaching ion as compared to the large energy barriers associated with epitaxial growth of crystalline phases. Therefore ion attachment and PNC growth is accelerated by the disordered hydration sphere that is weakly bound, in contrast to the ordered hydration layers that are more strongly associated with highly crystalline surfaces. The work of Tribello also shows that Ca^{2+} may exist in mono- and bi-dentate configurations with CO_3^{2-} within the PNC (notated η_1 and η_2 , respectively, for the number of oxygen shared between Ca and a single CO_3 entity). This is evidenced by the double well observed in the color-coded free energy profile of Ca-association (Figure 2). On larger scales, computational studies have shown that cluster growth proceeds not only by ion and ion pair attachment, but may accelerate by cluster agglomeration without any known energy barrier^{18; 111}. Raiteri and Gale have developed several new classical force fields that are parameterized based on the thermodynamics of solvation and polymorph phase transitions for anhydrous crystalline calcium carbonates (calcite, vaterite, and aragonite) in water

^{19; 20; 22}. They have applied their force fields with reasonable success to hydrated phases in the Ca-CO₃-H₂O system (including ACC, ikaite, and monohydrocalcite), although for hydrated crystalline species (ikaite, and monohydrocalcite) the errors in lattice parameters and unit cell volumes are significantly larger than for anhydrous species. Subsequent studies performed with their force fields has emphasized the importance of water in the nucleation and growth process. Figure 3 shows the chemically disordered nature of the PNC surface, where the variations in surface composition are indicated by color code (Figure 3A; red=oxygen, green=calcium, blue=carbon).

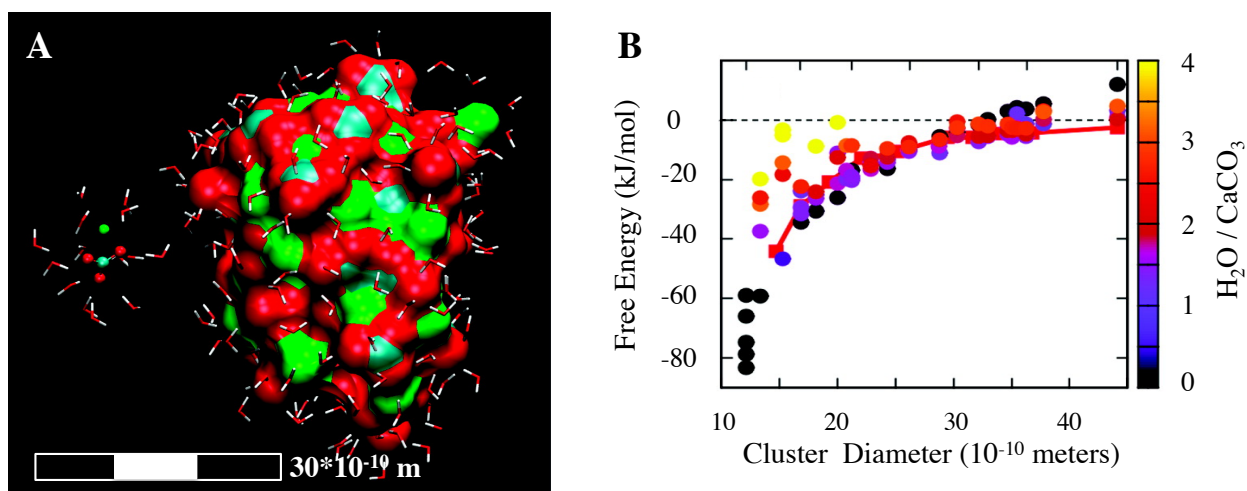


Figure 3. “Water is the Key to Nonclassical Nucleation,” showing a snapshot from MD simulation of hydrated ion pair addition to a growing cluster (A) and free energies as a function of cluster size and hydration state (B). ^{19; 20}

As previously suggested in the work of Tribello and colleagues, the work of Raiteri and Gale supports the idea of a disordered PNC surface and further illustrates the influence of surface disorder on the hydration sphere of PNCs. Free energies of the PNCs derived from their simulations show that very small PNCs (10 Å) are stable in an anhydrous state and that larger clusters require the inclusion of increasing amounts of water to remain stable as the cluster size

grows. The anhydrous PNCs appear to destabilize without additional water at larger diameters due to increasing internal energy that outweighs the favorable solvation energy of the amorphous particle. On the other hand, very high hydration levels ($\text{H}_2\text{O}/\text{CaCO}_3=3-4$) are overall less stable, and therefore phases at this level of hydration are more transient also maintaining relatively small particle sizes (up to 20 Å). Within these extremes, computations show that at intermediate level of hydration ($\text{H}_2\text{O}/\text{CaCO}_3=1-3$) PNCs are reasonably stable and may grow to larger diameters (> 40 Å). Indeed 1-2 stoichiometric waters are commonly observed in experimental synthesis of ACC, consistent with the idea of ACC forming from partially-hydrated PNCs^{55; 101; 102; 112}. However, the notion of fixed water content is artificially imposed by the simulation conditions and there is no reason to assume from first principles that any PNC is homogeneous. Although not explicitly postulated by Raiteri and Gale, their work provides an energetic basis for the evolution of PNC composition with growth, and is consistent with hypotheses of an anhydrous core with a gradient of water contents as one moves radially from the particle center in ACCs. Some inferences from TEM have suggested the PNC is non-homogeneous^{23; 55} but the subnanometer scales are at the limits of microanalytical technology and no large-scale computer simulation have addressed the non-homogeneity of PNC/ACC materials.

There remains a debate as to whether the local structures of PNCs and amorphous carbonates reflect the minimum energy configurations of equilibrium crystalline phases or something altogether different, and whether the short-range structure of PNC/ACC influences the pathway of crystallization and the final crystal structure. According to the theory of *polyamorphisms*, amorphous phase may possess local structural environments similar to those of crystalline polymorphs⁵⁵, however such domains are too small for coherent X-ray diffraction. The theory of polyamorphism also suggests that an amorphous carbonate will become

predisposed to a particular crystallization pathway during the cluster evolution. This stands in contrast to the network amorphous structures of silicates and the topological models of metallic glasses that possess unique structural environments that are entirely different from crystalline analogs. These glassy states are super-cooled liquids that reflect the solvated solution structure rather than the trajectory toward crystalline phases. None-the-less, polyamorphism theory is consistent with short range structural transitions from vaterite-like to calcite-like PNC/ACC that have been observed in solution close to the CaCO_3 saturation point (pH~9.5) using WAXS²³, ^{13}C NMR⁵⁵, and diffraction-based crystallization experiments¹¹³. One should note, however, that the spectral features of the amorphous material are very diffuse and these authors interpret the mean values of their data solely in terms of the theory of polyamorphisms. Additional support for polyamorphism comes from the observation of mixed aragonite/vaterite-like local structures in polarizable MD simulations of PNC growth¹⁸ however these results are not supportive of the calcite- and vaterite-like polyamorphisms of Gebauer's work. To add to the disagreement, meta-dynamic simulations suggest that only vaterite-like structures are possible in early stages of clustering¹¹¹ and time-resolved synchrotron XRD showed distinct stepwise transitions from ACC to vaterite to calcite¹⁰⁶. Another study combined EXAFS and ^{13}C - ^1H NMR observations and found no clear relationship between synthetic ACC and any known short-range structure¹¹², entirely contrary to the previous interpretations of polyamorphisms. The Goodwin et al. model of ACC utilized reverse Monte-Carlo (RMC) modeling of X-ray total scattering (Figure 4) to identify the segregation of Ca-poor domains (blue/purple) from anhydrous ACC domains (red)²¹ having an intermediate scale

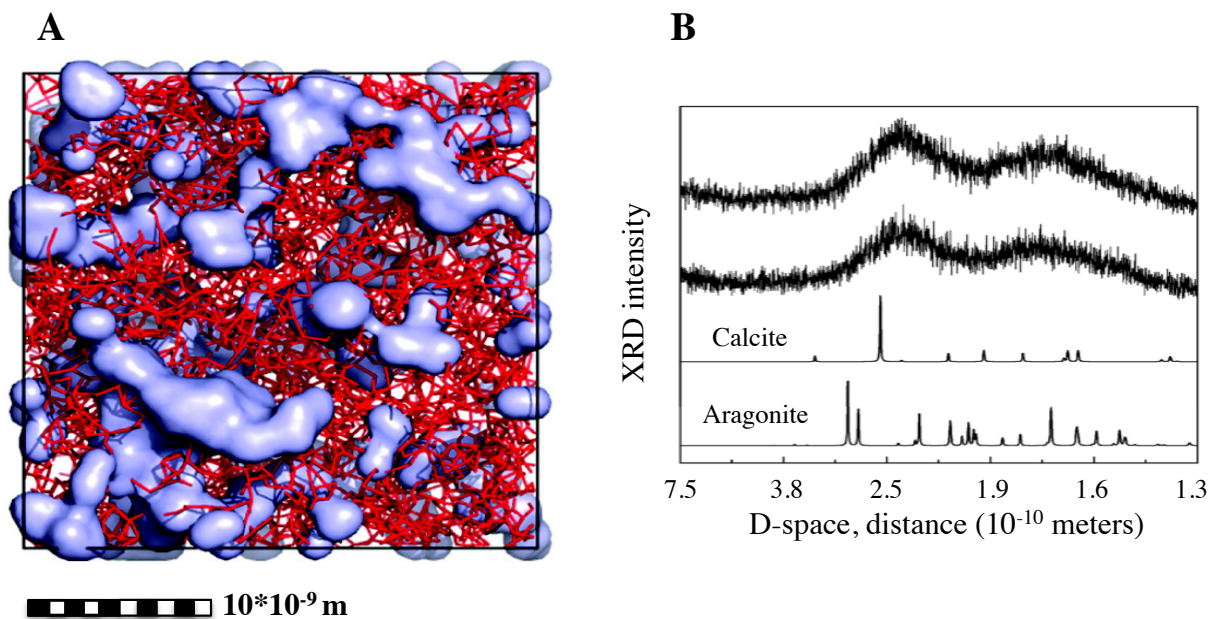


Figure 4. Goodwin et al.'s (2010) reverse Monte-Carlo refinement of experimental total scattering data²¹ of an ACC structure having 'monohydrate' composition (1a) and experimental XRD of indistinguishable materials (1b) that were produced using two different synthetic methods¹¹².

heterogeneity. Though it is important to note that RMC modeling does not produce a single, unequivocal structure, there is no evidence in any of the RMC results that is consistent with local environments analogous to the crystalline polymorphs of calcium carbonate. One of the Goodwin et al. RMC models was used as the initial configuration for our molecular dynamics studies of ACC structure and stability and will be analyzed directly for comparison to NMR results below (see methods and results)¹⁰¹. In summary, there are a great many variables to consider that must differ in the preceding experiments and therefore lead to differing results. The subtle influence of experimental variables on metal-carbonate clustering kinetics and the exact mechanistic controls of crystalline polymorph selection remains a matter of debate for amorphous carbonates. One of the key objectives of our work is to address the relevance of

various structural models for the ACC-ACMC-AMC system via NMR, which is sensitive to the molecular-scale structural environments about weak x-ray absorbers such as H, C, O, and Mg.

C. Behaviors of Magnesium in Carbonate Precipitation

Amorphous calcium carbonates are stabilized by organic and inorganic mechanisms, where as amorphous calcium carbonate precipitated from an impurity-free matrix has low water content (≤ 1 formula unit) and crystallizes rapidly (seconds to minutes) to vaterite and/or calcite products^{55; 112}. Stabilizing elements/molecules include specialized biogenic proteins^{85; 114; 115; 116}, synthetic organic polymers^{35; 88; 109; 117; 118} and select inorganic ions like Mg^{2+} ^{29; 32; 34; 118; 119; 120; 121; 122; 123; 124}, PO_4^{3-} , and Cu^{2+} . It is well-known that impurities affect the short-range structure, increase the induction time of nucleation (the time period from addition of all chemicals to the observation of the first visible precipitates)¹⁰⁹, and increase the solution's ability to become supersaturated with respect to $CaCO_3$. Few studies articulate explicit structural models of impurity domains in amorphous materials, except recent studies that demonstrate silica impurities are excluded from ACC to form a coating at the particle surface^{125; 126}. There have been EXAFS studies of impurities in amorphous and crystalline carbonate phases^{34; 54; 127; 128; 129}, but these have often produced conflicting results and have not provided clear relationships that link impurity domains in amorphous materials to crystalline products^{128; 129; 130}. Furthermore, these EXAFS studies often seek single-phase solutions, making their applicability to amorphous carbonates possibly inappropriate if the material is indeed heterogeneous. Additional challenges to understanding impurity inclusion/exclusion and local structures from these types of studies include verification of impurity dynamics and insight into what regulates inclusion and exclusion at the solid-liquid interface. One study of monohydrocalcite (MHC) crystallization noted a Mg-

rich rind surrounding radiating crystals of MHC ¹²¹. Presumably the structure emerged through transformation of an amorphous aggregate and that dissolution of Mg from ACC was intimately related to the crystallization of MHC and precipitation of the Mg-rich rind. Integrated experimental and computational studies are needed to resolve the evolution of dissolution, diffusion, and reprecipitation within a condensed medium like ACC with sufficient atomic detail to capture interfacial processes and the integrated effects over intra-particle (micron) length scales.

Due to its high abundance in seawater and its chemical similarity with Ca, magnesium is a common impurity in biomineralized calcium carbonate, and has received much attention ^{34; 54; 77; 119; 121; 122; 131; 132; 133; 134; 135; 136}. The temperature sensitivity of Mg incorporation in carbonates has been used for decades as a palaeothermometer of ancient ocean temperatures ²⁹. Without mechanistic knowledge of the incorporation mechanism and subsequent mineral transformation rates, such temperature reconstruction is plagued by species-specific and local artifacts—the so-called ‘vital effects’ mentioned earlier in this dissertation ^{9; 84; 137}. Table 1 illustrates Mg contents of several naturally occurring and synthetic examples of predominantly calcium carbonates. Magnesium content of coprecipitated calcium carbonates and biogenic calcium carbonates is a function of solution composition, temperature, degree of crystallization and crystallization mechanism, solution trapping within particles, and the final phase assemblage that may coexist. Therefore, increasingly sophisticated material characterizations, and a deeper understanding of the chemical mechanisms and structural pathways utilized by each organism are vitally important to understand the impurity composition of biomineralized materials.

Table 1. Magnesium content of biogenic and synthetic carbonates. Pathway of precipitation and impurity exclusion kinetics during recrystallization give rise to tremendous variability between biological species. Intraspecies variability is not known but likely also depend on individual metabolic differences that are a function of local water temperature, turbidity, and water chemistry.

Material	Mg (at. %)	Ref.
Ascidian Skeleton ACC	5.9	[12]
Ascidian Organic	1.7	[12]
Synthetic ACC+Mg	8.5	[12]
Ascidian Skeleton ACC	9	[67]
Plant Cystolith ACC	4-13	[67]
Foraminifera aragonite	0.01-0.06	[84]
Brachiopod Calcite	4-12	[27]
Coral Aragonite	0.04-0.08	[85]
Clam Aragonite	5.8	[86]
Synthetic ACC+organic	25-50	[29]
Synthetic MHC	5.2	[87]

From inorganic and biological crystallization experiments it is well known that Mg generally leads to the crystallization of aragonite, rather than calcite or vaterite, and the mechanism of magnesium's influence over polymorph selection is a long-standing question in regards to numerous marine organisms that produce long-lasting aragonite far outside of this phase's field of equilibrium 'thermodynamic' stability. This question is intertwined with the details of Mg inclusion in ACC and its subsequent exclusion during crystallization processes. The overall chemical depletion of Mg in ACC relative to parent solution concentrations¹³⁸ implies that there is an initial selectivity at the solid-liquid interface of the growing ACC particle. It has been shown that Mg incorporation to ACC is less selective at large activity products¹³⁹. Mg is further occluded from ACC upon crystallization to MHC, 6HC, or anhydrous phases³², which is widely supported by bulk chemical data and by EDS mapping of Mg-rich skins on spherical MHC microstructures¹²¹. Even so, up to 10% of Mg substitution

may persist in MHC¹⁴⁰. Mg incorporation into ACMC is also linked to the topology of coexisting organics if they are present³⁵. The first simulations on Mg-organic coupling by polarizable MD suggest that Ca²⁺ readily forms contact ion pairs with carboxylic oxygen while Mg²⁺ will not bind to the organic matter in a stable fashion¹⁴¹. Mg is highly excluded during foraminifera calcification (Table 1) and the degree of Mg selectivity is insensitive to dissolved inorganic carbon (DIC)¹⁴². Synchrotron x-ray absorption spectroscopy (XANES, EXAFS) studies of Mg-stabilized ACC find Mg stabilization causing an evolution from aragonite-like short-range structure to MHC-like with increasing Mg content, in contrast to other stabilizing agents such as eggshell protein¹²⁹ and [poly]aspartic acid¹²⁸ that lead to vaterite-like ACC; however this only causes more confusion, since it appears that inclusion of Mg in ACMC does not facilitate an aragonite-like local structure. No complimentary NMR, neutron scattering (INS, SANS), or simulations have been reported for Mg-PNC/ACC formation or related to the activity of Mg²⁺ in association with PNC/ACC surfaces. There is, however, ample evidence that Mg incorporation is coupled to the hydration state of ACC. Recent QM-DFT calculations demonstrate a strongly bonded Mg[η¹-(H)CO₃](H₂O)₄⁺ hydrated complex^{17; 143}, providing a basis for structural coupling between water and Mg in ACC. Mg K-edge XAS has shown that Mg-O in ACC is shortened (2.04-2.06Å) relative to anhydrous minerals (2.10-2.12Å)³⁴; this likely reflects existence of the aforementioned hydrated complex (Mg-O=2.06Å)¹⁴³ or less-probable interactions with organic phases (2.07-2.09Å)⁵⁴. Additionally Mg K-edge XAS has shown that Mg-O in aragonite is substantially shortened (2.06-2.08 Å) relative to Ca-O in aragonite (2.55 Å) suggesting either severe substitutional distortion or segregation to a nanophase of unknown structure⁵⁴. The literature from Mg-EXAFS of ACMC and Mg

substitution in crystalline carbonates lacks any general consensus, and therefore may suggest that a diversity of mechanisms and pathways for Mg incorporation and exclusion in carbonate phases.

D. Reference Phases in the Ca-Mg-CO₃-H₂O System

The combination of these four elements (Ca, Mg, CO₃, H₂O) provide a number of crystalline geometric arrangements to produce a variety of crystalline materials (polymorphisms) and materials in the Ca-Mg-CO₃-H₂O system are broadly susceptible to disorder, solid solution, defects, and multi-phase crystallization assemblages. As mentioned above, the theory of local polyamorphisms asserts that the amorphous phases can be understood in terms of local domains that are similar to crystalline polymorphs, however this model stands in contrast to the network structures of silicate glasses and topological theories of metallic glasses. Regardless of whether local polyamorphism or glassy network structures are the correct models for ACMCs produced from synthetic seawater, the crystalline materials in the Ca-Mg-CO₃-H₂O system (Table 2) provide useful comparisons to the nonequilibrium amorphous phases that form the primary subject of this thesis. Indeed, the unstable amorphous phases do eventually transform into these materials, and knowledge about them is therefore essential to an evaluation of whether crystalline “templating” exists on the molecular scale. The compounds of Table 2 form the standard state, or reference phases, to which we will compare our experimental results for amorphous and disordered precursors.

Calcium carbonate crystallizes in three anhydrous phases (CaCO₃: calcite, aragonite, and vaterite) and two hydrated phases (CaCO₃•H₂O: monohydrocalcite and CaCO₃•6H₂O: ikaite). Of the anhydrous phases, calcite is thermodynamically favored at ambient conditions and has the

smallest mean Ca-O bond distance (2.36 Å). Aragonite has the longest mean Ca-O bond distance (2.47 Å) and is favored under elevated pressure, temperature, and in the presence of large impurity ions (Sr^{2+} , Pb^{2+} , Ba^{2+}). Whilst MgCO_3 (magnesite) and $\text{CaMg}(\text{CO}_3)_2$ (dolomite) adopt a calcite-like structure, $\text{Mg}^{2+}_{(\text{aq})}$ promotes crystallization of aragonite¹¹⁸ and carbonate hydrates¹⁴⁴ rather than promoting dolomite or magnesite phase separations. The exact mechanisms that underlie the effects of Mg are long standing questions of carbonate chemistry (discussed in the previous section C). MHC and ikaite are thermodynamically favored with respect to calcite in the presence of water by low temperature ($<25^\circ\text{C}$) and by crystallization inhibitors such as proteins^{91; 145}, Mg^{2+} ¹²¹, and large anions (polyphosphate). These inhibitors are widely thought to influence crystallization by affecting the pre-nucleation clusters or by their incorporation into the amorphous precursor, although the exact mechanisms of crystallization (and therefore the exact role of these calcite inhibitors) are poorly understood. Ikaite consists of calcium carbonate ion pairs isolated within a clathrate-like cage of hydrogen bonded water molecules. Monohydrocalcite has been described by two accounts that differ with respect to the orientation of water molecules^{146; 147}. The more recent neutron scattering study of Swainson has likely determined the true proton positions although there is not sufficient evidence to reject the existence of both varieties and/or a disordered continuum. Vaterite is a kinetically preferred product of carbonate crystallization whose ambient stability is intermediate to calcite and aragonite (mean Ca-O bond distance is $\sim 2.40\text{\AA}$). The controversy regarding the nature of vaterite is similar to that of monohydrocalcite, having several structural variants that may include carbonate ion orientation disorder and the possibility of stacking disorder¹⁴⁸. Kamhi's vaterite exhibits total carbonate ion orientational disorder¹⁴⁹ and is kinetically preferred over the more ordered and more stable variety solved computationally by Wang¹⁴⁸. Wang's vaterite is -11

kJ/mol more stable than the Kamhi's disordered vaterite, however the activation of ordering was estimated to be 94 ± 10 kJ/mol^{148; 149; 150}, and therefore the disordered variety is likely to persist at ambient conditions. While calcite and aragonite have widely known occurrences in biomineralized materials, it has also been recently observed that ACC transforms to vaterite in the calciferous gland of earthworms⁸⁹.

The mixed Ca-Mg crystalline phases are generally sorted into two distinct groups above and below $x = \text{Mg}/(\text{Mg} + \text{Ca}) = 0.5$. Mixed crystalline phases that are rich in Ca ($x < 0.5$) are typically isostructural with calcite as a solid solution series from calcite up to $x = 0.3$ and from dolomite down to $x = 0.47$, exhibiting an immiscibility gap between ($x = 0.3 - 0.47$) that separates “magnesian calcites” from “calcian protodolomites” under ambient conditions^{132; 151}. Magnesium solid solution in aragonite is restricted to a smaller compositional range ($x < 0.1$) than observed for calcite (discussed above in section C). Very little is known about Mg substitution in monohydrocalcite and ikaite, although one theoretical DFT study suggested that $x = 0.5$ variety of ikaite should be thermodynamically favorable⁴³ although no such material has been observed naturally or synthetically. The mixed magnesium-calcium phases ($x > 0.5$) $\text{CaMg}(\text{CO}_3)_2$ (dolomite), $\text{CaMg}_3(\text{CO}_3)_4$ (huntite), and $\text{Ca}_2\text{Mg}_{11}(\text{CO}_3)_{13} \cdot 10\text{H}_2\text{O}$ (sergeevite) tend toward discrete phase separation rather than solid substitution and have unknown synthetic routes. This is perplexing as massive mountains of pure dolomite exist commonly in geological settings^{152; 153; 154}, yet their origin remains unclear and ordered dolomite is notoriously difficult to synthesize in pure form and at ambient temperatures^{38; 155} (a greater discussion of dolomite is given below in the section E, on crystallization). The crystal structure of naturally occurring huntite has been determined by powder XRD¹⁵⁶, while a detailed crystal structure refinement of sergeevite has not been accomplished. The contrasting behaviors of solid solutions below $x < 0.5$ and phase

separation when $x > 0.5$ may reflect more general thermodynamic tendencies of amorphous precursors phases like ACC-ACMC-AMC.

Pure magnesium carbonates exist only in a single anhydrous state MgCO_3 (magnesite, having calcite like structure) without analogs to vaterite or aragonite. The pure magnesium carbonates are dominated by a diversity of hydrated states including $\text{MgCO}_3 \cdot 2\text{H}_2\text{O}$ (barringtonite), $\text{MgCO}_3 \cdot 3\text{H}_2\text{O}$ (nesquehonite), $\text{MgCO}_3 \cdot 5\text{H}_2\text{O}$ (lansfordite). Barringtonite does not have a well known crystal structure¹⁵⁷ and so only nesquehonite and lansfordite have been explicitly considered as reference compounds for subsequent comparison to Mg-NMR data. At higher pH values (>10), OH^- present via direct addition or by autoprotolysis of water is also readily incorporated into magnesium compounds. Since $\text{Mg}(\text{OH})_2$ has a much lower solubility of with respect to $\text{Ca}(\text{OH})_2$ this could be anticipated that OH substitution into Mg-carbonates would be more favorable than for calcium carbonates. Hydroxide bearing phases also include a diversity of hydration states, leading to minerals such as $\text{Mg}_2\text{CO}_3(\text{OH})_2$ (pokrovskite), $\text{Mg}_2\text{CO}_3(\text{OH})_2 \cdot 3\text{H}_2\text{O}$ (artinite), $\text{Mg}_5(\text{CO}_3)_4(\text{OH})_6 \cdot 4\text{H}_2\text{O}$ (hydromagnesite), $\text{Mg}_5(\text{CO}_3)_4(\text{OH})_6 \cdot 5\text{H}_2\text{O}$ (dypingite), and $\text{Mg}_5(\text{CO}_3)_4(\text{OH})_6 \cdot 6\text{H}_2\text{O}$ (giorgiosite). Of these mixed hydroxycarbonate compounds, only hydromagnesite was observed in these experiments. Recently dypingite was discovered in natural association with hydromagnesite in arctic permafrost and attempts to synthesize (and presumably obtain detailed XRD structural refinements) are currently underway¹⁵⁸. Aside from hydromagnesite many of these compounds are not well understood structurally and therefore cannot be used for explicit comparisons as reference compounds for Mg-NMR. Much work remains to investigate and understand the crystalline phases of the Mg- CO_3 - H_2O system.

Table 2. Summary of Ca-Mg-CO₃-H₂O crystalline reference phases (with accepted mineral names). From inspection of unit formulae alone, one can observe the differential behaviors of Ca and Mg in the metal-carbonate-water system. For example, the diversity of polymorphs foreshadows the possibility for disorder, solid solutions, and mixed phase assemblages. The formulae of ikaite and lansfordite are similar to the simulated results of ion pair hydration structures. Mixed Ca-Mg compounds tend toward Mg-rich compositions. Mg-CO₃-H₂O compounds have a more continuous distribution of water contents than that of Ca-CO₃-H₂O compounds, reflecting the gradual dehydration kinetics of Mg-H₂O complexes.

Name	Formula	Name	Formula
Calcite	CaCO ₃	Magnesite	MgCO ₃
Vaterite	CaCO ₃	Barringtonite	MgCO ₃ •2H ₂ O
Aragonite	CaCO ₃	Nesquehonite	MgCO ₃ •3H ₂ O
Monohydrocalcite	CaCO ₃ •1H ₂ O	Lansfordite	MgCO ₃ •5H ₂ O
Ikaite	CaCO ₃ •6H ₂ O	Pokrovskite	Mg ₂ CO ₃ (OH) ₂
Dolomite	CaMg(CO ₃) ₂	Artinite	Mg ₂ CO ₃ (OH) ₂ •3H ₂ O
Huntite	CaMg ₃ (CO ₃) ₄	Hydromagnesite	Mg ₅ (CO ₃) ₄ (OH) ₆ •4H ₂ O
Sergeevite	Ca ₂ Mg ₁₁ (CO ₃) ₁₃ •10H ₂ O	Dypingite	Mg ₅ (CO ₃) ₄ (OH) ₆ •5H ₂ O
		Giorgiosite	Mg ₅ (CO ₃) ₄ (OH) ₆ *6H ₂ O

E. Crystallization

Throughout the literature and in this dissertation, there are numerous examples of how processing conditions and subsequent crystallization pathways can be used as a tool for reconstructing amorphous structure, with dolomite CaMg(CO₃)₂ and ikaite CaCO₃•6H₂O serving a special role in this regard. Crystallization experiments of ACCs lead to widely differing results that depend upon the extent and type of additives and impurities¹¹³, synthesis and aging temperature¹⁵⁹, pH/degree of calcium carbonate saturation in solution^{159; 160}, and a host of unsolved process variables. The diversity of results has created more confusion rather than a consensus of understanding. One might reasonably suppose that syntheses across the compositional span from ACC to AMC [0<Mg/(Mg+Ca)<1] and a range of naturally relevant

temperatures (0-25°C) can be used to produce most *or all* of the crystalline phases of Table 2 which are all found naturally occurring at ambient conditions. Continued effort toward controlled crystallization experiments, while appreciating the role of non-crystalline intermediates, should be a highly fruitful direction for future research.

The geological abundance of the mineral dolomite $\text{CaMg}(\text{CO}_3)_2$ and its apparent low temperature formation¹⁵³ stand in contrast to the rarity of modern dolomite formations and "impossibility"⁴² of low temperature synthesis in the laboratory. This contradiction was dubbed the 'dolomite problem'³⁷ and has yet to be resolved. In a natural setting, low-temperature dolomite formations are typically found in ocean sediments and a diversity of other environments including soils, rivers, coal, and pearls¹⁵⁵. Sulfate reducing microbes that mitigate the sulfate inhibition of dolomite formation has been hypothesized as mechanisms for precipitation of dolomite in natural settings^{161; 162; 163}. There have been many attempts to precipitate dolomite in the laboratory, but successful methods require hydrothermal conditions (>200°C) that are inconsistent with environmental observations of low-temperature dolomite (40-80°C)¹⁵³. For a comprehensive review of laboratory attempts at low temperature dolomite synthesis, the reader is referred to the book of Deelman, chapter seven (available freely online at the writing of this thesis)¹⁶⁴. Low temperature synthesis typically results in a controversial phase that has been given many names including protodolomite, neodolomite, hydrodolomite, magnesian calcite, calcian magnesite, etc. The most common low-temperature synthesis result is a Mg-deficient phase ($\text{Mg}/(\text{Mg}+\text{Ca})=x\sim 0.47$)—often called calcian protodolomite. Even dolomite seed crystallization experiments (>115°C) have resulted in calcian protodolomite overgrowths of the seed crystals⁴¹. Of the numerous terms in use, we will continue to use “protodolomite” to refer the entire genre of dolomite-like phases and whenever possible clarify

the specific details of hydration, stoichiometry, and coexisting phase assemblages. The stoichiometry of Ca and Mg in this family of materials can be easily obtained from the position of the *hkl*(104) reflection¹⁵¹. The Ca/Mg order parameter can be deduced from *hkl*(015) layers of alternating calcium and magnesium that give rise to superstructural reflections that are rarely observed in synthetic experiments. Even multi-year experiments have led to a lack of superstructural reflections⁴⁰, and one hypothesis suggests that slow diffusional ordering of cation disordered protodolomite is responsible for the massive geological formations, but requires geological timescales. Of the entire suite of literature, only one particular low-temperature experiment (40-60°C) involving many oscillatory acidic and basic cycles lead to a minor amount of ordered dolomite¹⁵⁵. A recent report using CMC gums and agar gels¹⁰⁴ has demonstrated that the synthesis of stoichiometric cation-disordered dolomite (coexisting with monohydrocalcite) is possible using non-biological synthesis in the presence of organic moieties. In the course of studying the suite of ACMC compositions in this work, we identified a purely inorganic method for synthesis of stoichiometric, cation-disordered dolomite at ambient conditions (20-50°C). The diversity of natural occurrences and difficulty of synthesis highlights the subtleties of pathway, process, and kinetics for the crystallization of dolomite and the difficulty in predicting the crystallization mechanism for ACMC materials.

The relationship between the carbonate hydrates (MHC and 6HC) and the amorphous precursor has also been a matter of debate. The argument for a direct relationship between monohydrocalcite and ACC on account of similar water contents (with ACC having 0-2 stoichiometric waters)^{121; 140} is weakly supported by the coexistence of ACC and MHC in calcareous corpuscles of tape worms⁹¹. Also previously mentioned in regards to the behavior of magnesium during ACC formation, one experiment observed radiating MHC spicules within a

Mg-rich exclusion rind. Yet, there are several reports of Mg-stabilized ACC conversion to ikaite^{145; 165; 166} including this work. Anecdotally, we have also observed MHC crystallization via dehydration of ikaite-like precursors (containing <6 H₂O per formula unit) at 50°C. The dehydration of ikaite to MHC is also supported by $\delta^{13}\text{C}$ and $\delta^{18}\text{O}$ studies on the coexistence of ikaite and MHC in a Greenlandic fjord¹⁶⁷. ACC, ikaite, and MHC have been observed dehydrating directly to *any and all* of the various anhydrous polymorphs¹⁶⁸. The numerous pathways of crystallization can only be systematically addressed with clearer understanding of ACC, APMC, and AMC structure.

One recent study compares the structure of ACC, nano phase separation, and crystalline phase through the lens of thermochemistry^(102; Figure 5). The authors conclude that a dolomite-like APMC ($x=0.5$) is most stable of all amorphous carbonates, analogous to the crystalline species dolomite $\text{CaMg}(\text{CO}_3)_2$. Based on the slope trajectories of figure 5, the authors infer that Mg-rich compounds [$x=\text{Mg}/(\text{Mg}+\text{Ca})>0.5$] are phase-separated and represent a two-phase mechanical mixture of a dolomite-like APMC and AMC. This is not unlike the tendency for dolomite, huntite, and sergeevite to phase separate. Amorphous carbonates with $x<0.5$ that are Ca-rich do not follow the predictions of a simple mixing model, and therefore a solid solution is proposed. This is not unlike the tendency for Ca-rich mixed phases ($x<0.5$) to exist in solid solutions that are isostructural with a pure Ca polymorph. However, there are well known immiscibility gaps on both sides of the $x=0.5$ composition in this system, and therefore unmixing of solid solutions is expected in all regions of the diagram. In addition, the authors used two different precipitation techniques, a Na_2CO_3 addition such as in this study below $x=0.5$ and an ammonia-based precipitation method above the $x=0.5$ boundary, making it difficult to determine whether their observations are a synthetic consequence rather than a general principal.

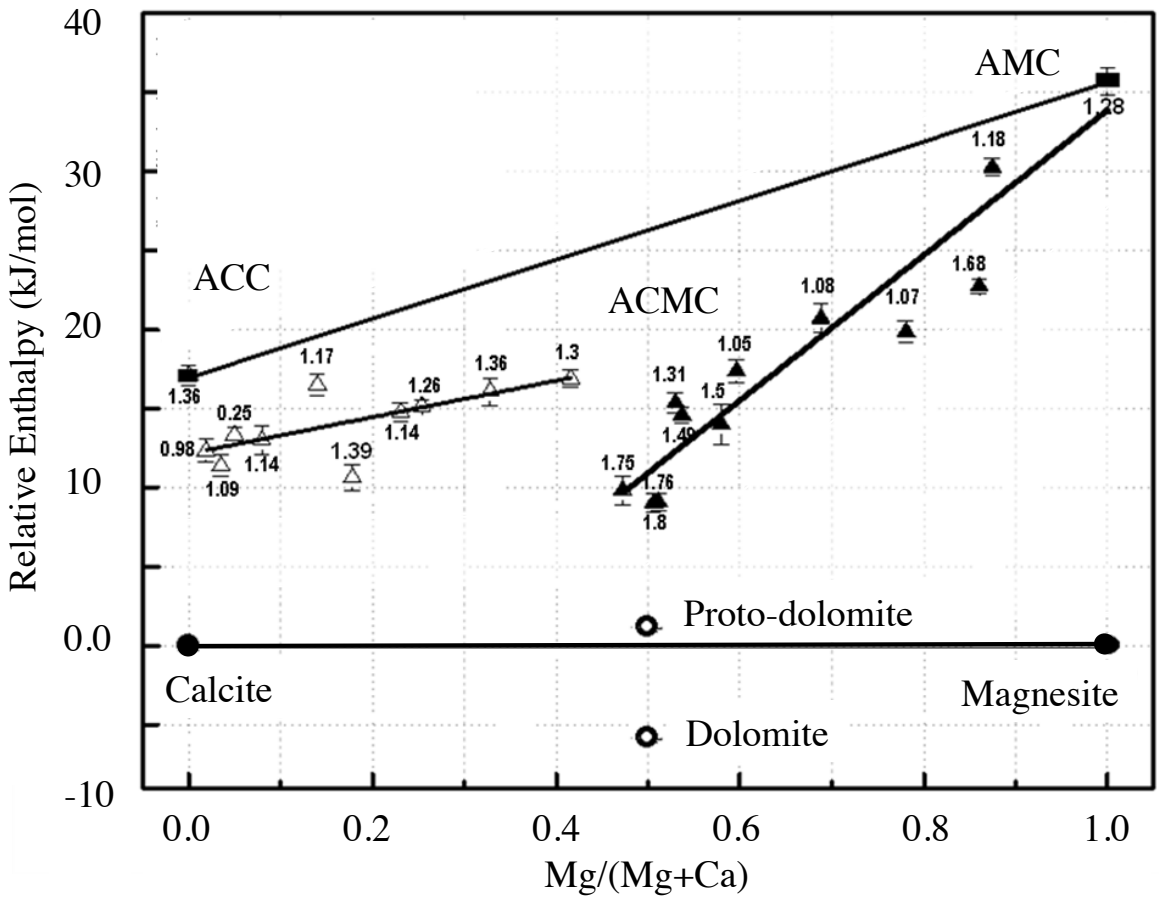


Figure 5. Calorimetry of Amorphous Phases relative to anhydrous crystalline endmembers¹⁰² that implies solid solution from $x = \text{Mg}/(\text{Mg} + \text{Ca}) < 0.5$ and a mechanical mixture of AMC ($x = 1.0$) and ACCM ($x = 0.5$) when $x > 0.5$.

METHODS

A. Synthetic Methods (Overview)

There are diverse methods for precipitation of alkaline earth carbonates: addition of alkali carbonate (direct precipitation), addition of ammonia, diffusion gel methods¹¹⁹, introduction of CO₂ gas to Ca²⁺ bearing solutions, and enzyme catalysis¹³⁶. The method used in these studies involves solid Na₂CO₃ additions to synthetic seawater to form the precipitated phase. The amounts of Ca and Mg in the precipitated solids may be controlled via a temperature dependent chemical fractionation of the ions between the solid and solution phases, by modifying the parent solution composition, or by the degree of supersaturation (degree of Na₂CO₃ excess, effectively the solution pH generated by the basic reagent if other carbonate salts are used). For collection of amorphous materials, immediately upon observation of an opacity change in the solution, the reaction is quenched by vacuum or gravity filtration and washing using anhydrous methanol. The MeOH wash removes excess free H₂O that catalyzes the crystallization process while preserving chemical water within the amorphous structure. Throughout this work, sample designations will refer to the condition of synthesis and parent solution composition with labels described in Table 3. In all cases the MeOH wash solution is stored at an equivalent temperature (room temperature or ice bath) to ensure consistent thermal history of the precipitated phase. Whenever possible, the sample weight was monitored gravimetrically to ensure evaporation of MeOH and characterized either immediately or within days of quenching depending on the anticipated stability of the sample (stability with respect to composition is inferred from preliminary syntheses performed in our laboratory).

Table 3. Labels of synthetic variables used throughout this manuscript. Note that these labels refer to the parent solution, while the compositional variable $x=[\text{Mg}/(\text{Ca}+\text{Mg})]$ and water contents (weight percent) refer to the solid composition.

Mg/Ca	Label
5	High-Mg
0.5	Low-Mg
0	Mg-free
Temperature	
20-25	RT
0-5	LT

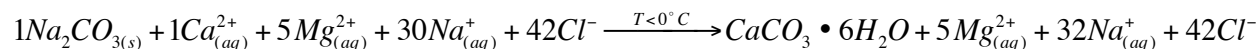
For NMR analysis, samples of ^{43}Ca -enriched ACC, AMC, and ACMCs were synthesized by a similar method. Because ACC can readily transform to the crystalline phases, samples for NMR analysis were prepared immediately adjacent to the NMR spectrometers at the NMR facility of the William R. Wiley Environmental Molecular Sciences Laboratory (EMSL) at Pacific Northwest National Laboratory (Richland, WA, USA). Synthetic seawater (600mM ionic strength) was prepared by adding deionized water, NaCl, and $\text{MgCl}_2 \cdot 6\text{H}_2\text{O}$ to a ^{43}Ca -enriched solution prepared by dissolving ~ 0.5 g of 30%-enriched $^{43}\text{CaCO}_3$ (ISOFLEX USA) in a slight excess of 0.1 M HCl. Solutions used during the precipitation process were prepared using reagent grade NaCl, anhydrous Na_2CO_3 , and $\text{MgCl}_2 \cdot 6\text{H}_2\text{O}$ (Fischer Scientific) and >17 M Ω deionized water. The identity and purity of the solid reagents obtained from Fisher Scientific were determined before solution preparation using XRD and TGA. The NaCl was anhydrous as reported, but the $\text{MgCl}_2 \cdot 6\text{H}_2\text{O}$ contained an additional $4\text{H}_2\text{O}$ /formula unit ($\text{MgCl}_2 \cdot 10\text{H}_2\text{O}$) likely to buffer against evaporation and to preserve the hexahydrate structure. The amounts of Mg and Ca were varied to produce parent solutions with molar Mg/Ca ratios of 5 and 0. In experiments without Mg, additional NaCl was added to maintain constant ionic strength. Samples were synthesized either at room temperature (20-25°C) without additional

temperature control or at 2-5°C maintained by direct contact of the reaction beaker with a crushed ice/water mixture. Temperature was monitored over the course of each reaction using a digital temperature sensor mounted in the reaction beaker and a mercury thermometer placed in the external thermal reservoir (bench top or ice bath).

To induce ACC precipitation, anhydrous Na_2CO_3 was added to the solution while the mixture was stirred rapidly. The amount of Na_2CO_3 added was varied such that the onset of observable precipitation occurred within a few minutes regardless of the solution Mg content. The Mg-free sample required only stoichiometric addition of Na_2CO_3 (no excess CO_3^{2-}), whereas solutions with Mg/Ca = 5 required addition of 1.5 to 2.0 times the stoichiometric amount of carbonate to obtain a similar induction period. The pH of our synthesis equilibrates to ~10 with excess Na_2CO_3 . However it is important to consider that PNC formation, aggregation, and precipitation occurs on a pH gradient at the interface of the parent solution with dissolving Na_2CO_3 . Unlike the robotic titrations of Gebauer et al.^{23; 55}, it is impossible for us to specify an average pH that reflects the microscopic disequilibrium of this precipitation method. As the solutions became uniformly cloudy, the suspended solids were rapidly collected via vacuum filtration using 650nm Millipore type DVPP filters. The filtered solids were rinsed with >100 mL anhydrous methanol (Sigma Aldrich) previously equilibrated at the appropriate temperature (RT or over ice). The solids were then air-dried on the filter apparatus for 1-2 minutes. In most cases it was possible to complete filtration and drying within 10 minutes of introducing the Na_2CO_3 . Samples were considered to be completely dry when their mass became stable for ~10-60 minutes on a four-digit balance or as indicated by >2-3 half-lives of exponential weight loss. The mode of weight loss was not confirmed via mass spectrometry or other analytical method, but is thought to include a labile residue of methanol and water. The air-dried powders were

lightly dispersed with a mortar and pestle and immediately loaded into 4mm rotors with standard end caps for NMR analysis. Effort was made to ensure the rotor temperature during transport and immediately upon insertion to the NMR probe matched with the synthesis temperature.

Crystallization experiments employ a variety of modifications to the amorphous synthesis described above. Such modifications include increased exposure to the parent solution (long stirring time), low degrees of supersaturation (low activity product nearer to equilibrium), rinsing with water rather than methanol or absence of washing, heating (25-50°C) under humid conditions, freezing, and/or any combination of these. To induce dolomite crystallization, the amorphous precursor is washed with deionized water rather than MeOH, and is stored at 20-50°C and 100% relative humidity in an open plastic vial for 11 days. The sample is dried for analysis at room temperature. Synthetic ikaite was prepared for NMR analysis at the William R. Wiley Environmental Molecular Sciences Laboratory housed at Pacific Northwest National Laboratory, and method development and additional characterizations were executed at Alfred University. Ikaite is synthesized by addition of anhydrous $\text{Na}_2\text{CO}_{3(s)}$ to a saline parent solution and stored in a freezer for one week. The saline parent solution is similar to synthetic seawater, consisting of 30 parts NaCl, 5 parts MgCl_2 , and 1 part CaCl_2 . A stoichiometric amount of Na_2CO_3 is added to the parent solution in a lidded polyethylene container over an ice/salt mixture ($<0^\circ\text{C}$) as shown in following reaction:



The mixture is stored in the freezer for one week at -15°C . The low synthetic temperature and common ion effect of Na^+ , and increased supersaturation limit (effect of Mg^{2+}), assist in reducing the solubility of Na_2CO_3 and inhibit the formation of an amorphous intermediate. If Na_2CO_3 dissolves too quickly, then an amorphous intermediate is formed and the formation rate

of ikaite is limited by the subsequent dissolution of the intermediate. After one week ikaite crystals are recovered from the synthesis by thawing the frozen reaction vessel on ice (at 0°C), until no ice remains within the polyethylene container. The contents of the reaction vessel are vacuum filtered and washed and dried with ice-cold anhydrous methanol.

B. Characterization Methods

X-ray Diffraction (XRD)

Powder XRD experiments were performed on dry powders (ex-situ; subjected to methanol quenching) using several instruments at Alfred University, including the Bruker D2 Phaser and Bruker D8 Advance equipped with the "lynx-eye" detectors. Powder samples were prepared on 1 inch, circular, sapphire single crystal substrates as thin layers of material. In some cases a small amount of finger grease was utilized on the substrate to ensure that the sample was firmly adhered to the substrate. Diffraction experiments typically ranged from 5-50° (2 θ ; Cu K α) with variable count times (0.5-10 seconds/step) selected based on the stability of the sample and variable step sizes (0.02-0.5 degrees/step) depending on the crystallinity of the sample. Samples are rotated at 40 rotations per minute to avoid powder orientation effects. Diffraction patterns are plotted as the logarithm of XRD intensity throughout this work to emphasize evidence of structure in the background residual. Background subtraction was accomplished by manually scaling the background intensity for each sample until a qualitative best fit was obtained that sufficiently removed the background features. XRD experiments were also performed on the samples synthesized at Pacific Northwest National Laboratory (PNNL) immediately prior to and following NMR analysis using a Rigaku high power microbeam instrument (35 kV, 25mA) with particles dispersed onto a 0.25 inch, single crystal, silicon substrate. This instrument employed a

Cr rotating anode, 2D plate detector, and 0.3 mm spot collimator. XRD background conditions and reference materials are analyzed on all instruments to ensure reproducibility and to minimize instrument-to-instrument variability. These studies generated no data suggesting that more advanced data corrections were required.

Thermal Gravimetric Analysis- Differential Thermal Analysis (TGA-DTA)

TGA was performed on a TA-Instruments model 2960 Simultaneous TGA-DTA at Alfred University using Pt crucibles for samples and empty Pt crucibles as a reference. Samples were fired from ~25°C to 900°C at heating rates of 10°C/min. Weight loss as a function of temperature is normalized to the starting material mass (reported as weight percent of the original). The temperature difference between sample and reference is normalized by the continuously measured weight to give a mass-independent temperature difference. Water contents were calculated from the total weight loss below 250°C.

Scanning Electron Microscopy-Energy Dispersive Spectroscopy (SEM-EDS)

SEM at Alfred University was performed using both the FEI quanta and Amray instruments. The chemical compositions of the materials were determined by calibrated EDS using an FEI environmental SEM with optimized count rates of 2000/s and a 20% dead time. The samples were dried at 200°C before EDS. The accuracy of the EDS analyses was confirmed using mechanical mixtures of pure CaCO₃ and synthetic MgCO₃ in various ratios. The area over which the beam was scanned was on the order of 1 mm² and is sufficiently large to provide accurate average compositions. Automated ZAF corrections (Z atomic number, A absorption, F fluorescence) included Ca, Mg, Na, Cl, C, O, and H. Residual halite NaCl is estimated from the chlorine concentration, and residual Na (after subtraction of NaCl) is attributed to Na with carbonate coordination. EDS was chosen over the more accurate wavelength dispersive

spectroscopy (WDS) technique because a relatively wide compositional range ($0 < x < 1$) was explored that did not need highly precise values. WDS entails a more difficult sample preparation that was avoidable because of the acceptable precision of EDS.

Microscopic investigations of amorphous powders and protodolomite crystallizations were also conducted on an FEI Helios instrument at PNNL. Samples were carbon-coated and imaged from 2-5 keV using the Eberhard Thornley Detector or the immersion-mode “Through-the-Lens” detector at higher magnifications ($>10kX$).

Small Angle X-ray Scattering (SAXS)

Laboratory-scale SAXS measurements were explored for comparisons of similar ACMC materials ($x \sim 0.6$) that had been aged differently. The small angle scattering from ACMC were compared to crystalline calcite using a Bruker D8 advance using Cu K α radiation at 30 mA and 40 kV from 0.2 to 2 degrees (2θ) corresponding to a relatively small Q-range ~ 0.01 to 0.15 ($1/\text{\AA}$) or 100 to 5\AA . Samples were loaded into (1 mm diameter) glass capillary tubes and aligned by hand for capillary axis rotation during the analysis. The capillary tubes were rotated on axis at 40 rotations per minute, and analyzed with 0.005 degrees per step at a rate of 10 seconds per step. SAXS background was measured for air, empty glass capillary, crystalline calcite powder in glass and these are presented for comparison, although not subtracted from the sample data. Data is processed using the Porod plot [$y=Q^4 \cdot I(Q)$] approach.

NMR Overview

High-field solid-state NMR facilities capable of performing molecular-scale characterization of ^{43}Ca , ^{25}Mg , and ^{13}C at Pacific Northwest National Laboratory’s William R. Wiley Environmental Molecular Science Laboratory were used to perform the NMR experiments in this study. Many of these nuclei are insensitive due to low gyromagnetic ratio, low natural

abundance of the NMR active isotope, and large line-widths due to significant quadrupolar interactions, as discussed in the introduction. These limitations can be partly overcome by using the highest available external magnetic fields, as the signal intensity is directly proportional to the static magnetic field raised to some power (usually greater than 2). Also, for quadrupolar nuclei like ^{25}Mg and ^{43}Ca , line-width due to second-order quadrupolar interactions decreases with increasing external magnetic field. Several fundamental interactions lead to line broadening and limited sensitivity in solid-state NMR (dipole-dipole coupling, chemical shift anisotropy, the first and second order quadrupolar interaction); with the exception of second-order quadrupolar interaction, all of these interactions generate no effect on the NMR line shape under magic angle spinning conditions. However, the improved signal to noise ratio and resolution achieved by MAS NMR made it difficult to resolve different sites in our ^{25}Mg spectra (where the quadrupolar broadening was most significant). In the case of our nuclei of interest with low natural abundances (^{13}C , 1.1% abundant; ^{43}Ca , 0.145% abundant), sensitivity was also improved by preparing samples with isotopic enrichment up to 99% ^{13}C and 15-30% ^{43}Ca , as noted in the synthesis procedure above. One additional method traditionally used for sensitivity enhancement known as cross polarization was also employed in these studies. In cross polarization experiments, magnetization is transferred from an abundant spin system to a dilute spin system via dipole-dipole interactions. After allowing the abundant and dilute spins to interact for a specific time (dictated by several relaxation rates in the system), the resonance match condition is removed and the dilute spin system is detected at a much greater polarization than can be achieved by simple Bloch-decay experiments on the dilute system alone. However, cross polarization effectiveness is also a function of inter-nuclear distance, and thus ^1H - ^{13}C cross polarization experiments in ACCs/ACMCs/AMCs can be used to determine whether there is a

population of H₂O near in space to the carbonate group, shedding additional insights into the role of H₂O in these materials. The NMR experiments were all conducted on an Agilent Technologies DD2 spectrometer mated with a wide-bore 20.0 T (850 MHz ¹H resonance frequency) superconducting magnet, and used a 4.0 mm HXY T3 magic angle spinning probe. In our isotopically enriched samples, simple Bloch-decay magic-angle spinning NMR experiments were performed using ~90° tip angles, which maximize the signal intensity while sacrificing some ability to use the data quantitatively in the case of ⁴³Ca. For the ¹³C Bloch-decay experiments, high-powered proton decoupling was active during the acquisition period to minimize the effects of ¹H-¹³C dipolar broadening. The resonance frequencies of ⁴³Ca and ¹H are too different for ¹H-⁴³Ca dipolar coupling to be a significant concern (since the strength of dipolar coupling is proportional to the product of the resonance frequencies), negating the need for decoupling in these experiments. The ²⁵Mg NMR experiments did not require isotopic enrichment since ²⁵Mg is roughly 10% abundant, but this nucleus does experience the greatest line-widths due to its large nuclear quadrupole moment and subsequent strong quadrupolar interactions. In this case, sensitivity-enhancing pulse sequences like the quadrupolar version of the Carr-Purcell-Meiboom-Gill (CPMG) sequence were employed. The QCPMG increases sensitivity for nuclei with large quadrupolar line widths by discretizing the continuous signal into a series of narrow spikelets that map out the broad powder pattern one would obtain in a traditional Bloch decay experiment. In other words, the available signal intensity is contained within narrow spikelets and signal-to-noise ratio is improved by sacrificing some precision regarding the location of singularities. The spikelet spacing should be sufficiently small (high-spikelet density) as to capture the essential features of the static powder pattern that contain the useful structural information, but sufficiently wide to ensure that a suitable sensitivity

enhancement is achieved. This particular sequence can be used under static or magic angle spinning conditions, provided that signal refocusing due to the MAS rotational frequency is synchronized with CPMG spikelet frequency spacing. Examples of typical pulse sequences used in this work are diagramed in figure 6.

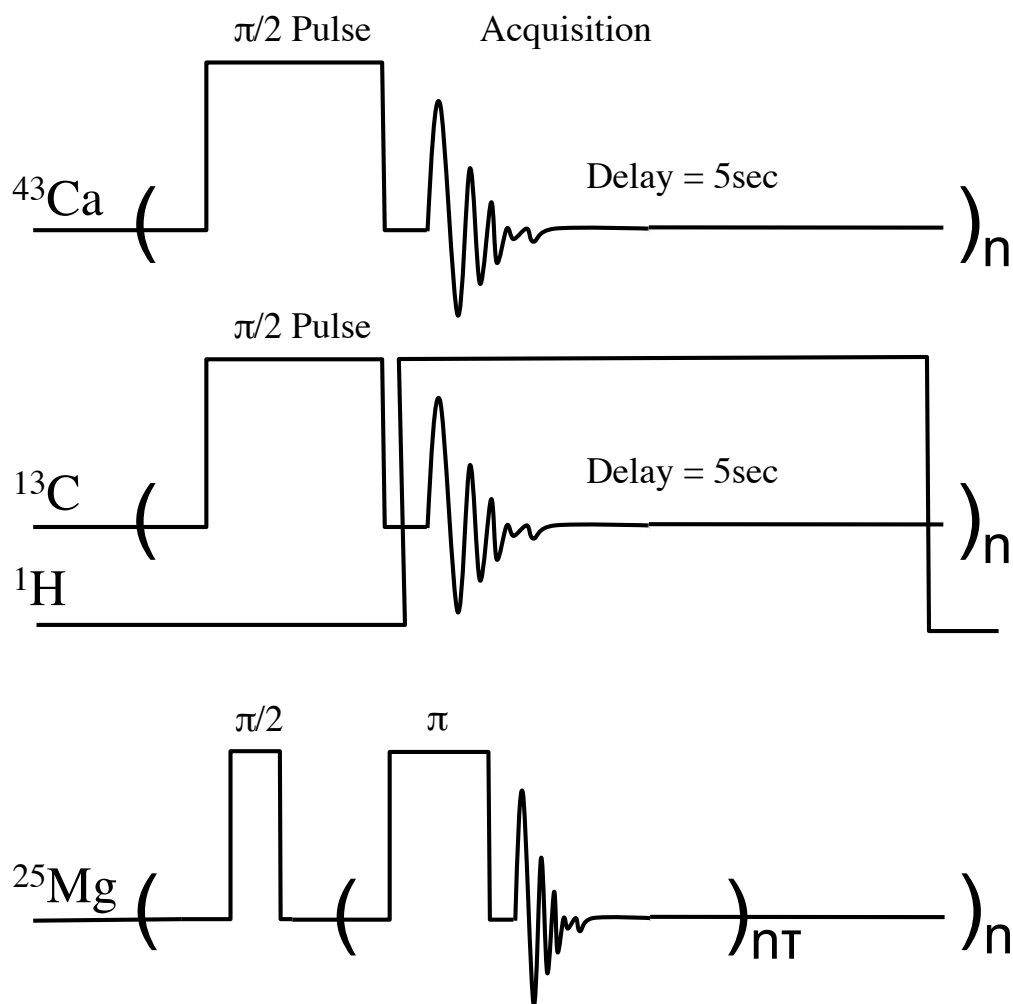


Figure 6. Pulse sequence diagrams for various sequences used throughout the work including Bloch decay, Proton-Carbon decoupling, and the quadrupolar Carr Purcell Meiboom Gill (CPMG) sensitivity enhancement.

Calcium (43) NMR

The ^{43}Ca Bloch-decay MAS NMR spectra were acquired at the synthesis temperature using a spinning frequency of 6 kHz, spectral width of ~ 40 kHz, and a recycle delay of 5s using the specialized low-noise low-frequency amplifier. Variations in sample temperature were minimized by immediately packing the ACC samples in standard 4mm ZrO_2 rotors after synthesis and transferring the samples to the NMR probe head with the probe and VT stack pre-equilibrated at the appropriate synthesis temperature. All experiments used a central transition selective $\pi/2$ pulse width of $3\mu\text{s}$ calibrated with a ^{43}Ca -enriched sample of calcium oxide, which was also used as a secondary reference standard (CaO resonates at +136.1 ppm relative to 1 M CaCl_2 (aq)). ^{43}Ca T_1 experiments using a sample composed of a physical mixture of ^{43}Ca -enriched CaO and calcite showed that a 60 s recycle delay is more than sufficient for complete relaxation of calcite under the conditions we employed, whereas CaO requires pulse delays of the order of several tens of minutes to achieve full relaxation. We performed multi-scan ^{43}Ca NMR experiments on the high-Mg, RT sample using pulse delays of 1s, 5s, 30s, and 60s and observed no difference in the final intensities. Thus, we used a 5 s pulse delay to acquire all subsequent ^{43}Ca spectra of the synthetic ACCs and ACMCs, which may bias our spectral intensities in favor of amorphous material. For the ACCs, spectra were collected in a series of consecutive one-hour blocks that were co-added to produce the spectra shown in this thesis. This approach allows for time resolution of possible phase transformations during long NMR experiments. To evaluate the crystallization behavior of the samples they were intermittently exposed to 50°C and 100% RH ex situ after the initial spectra were collected and subsequently reanalyzed by ^{43}Ca NMR over the course of a week. Ca spectra were processed using the Spinworks software for Fourier transformation of free induction decays, using 50 Hz exponential apodization without zerofill or left-shift.

The ^{43}Ca Bloch-decay NMR spectra of the ^{43}Ca -enriched ikaite were acquired under magic angle spinning (MAS) conditions at a 10 kHz spinning frequency. A central-transition selective $5\ \mu\text{s}\ \pi/2$ pulse width was used with a spectral width of 40.322 kHz, and pulse delay of 5 s to acquire 650 transients of 2048 complex data points. The pulse width, reference position, and effective pulse delay were established using a ^{43}Ca -enriched sample of calcite exhibiting a left edge at 20.96 ppm. The spectrum of ikaite was acquired at a temperature of -5°C . The spectrum was processed directly on the spectrometer using VNMRJ software with a 4-point left shift, 20 Hz of exponential apodization, and zero-filling to 16384 points. Ikaite spectra are included in the appendix.

Carbon (^{13}C) NMR

^{13}C MAS Bloch-decay experiments with proton decoupling were performed for 99% ^{13}C -enriched materials at the appropriate synthesis temperature (achieved according to the procedure described previously) on the same spectrometer setup, save use of the standard X-channel amplifier rather than the low-frequency version used for ^{43}Ca and ^{25}Mg . Each spectrum involved a spectral width of 100 kHz, 10 kHz MAS, and a $\pi/2$ pulse width of $4.25\ \mu\text{s}$ to acquire 2016 complex data points. A proton decoupling field of ~ 14 kHz was employed during the acquisition period only. The spectra of the enriched materials come from a single transient. However, our 'best' dolomite was not ^{13}C enriched and is the sum of <500 transients, with a 600 s recycle delay, which proved appropriate for a ^{13}C -enriched pure Ca-ACC sample.

^1H - ^{13}C variable contact time (VCT) cross polarization (CP) MAS spectra were acquired at -5°C using the same Agilent DD2 NMR spectrometer, 20.0 T magnet, and 4mm HXY probe. Cross polarization was achieved at 10kHz MAS using a $^1\text{H}\ \pi/2$ pulse of $4.5\ \mu\text{s}$ and a linear ramp with initial $\omega_{\text{H}} = \omega_{\text{C}} = 55.555$ kHz during the contact pulse. Contact times of 0.5, 1, 1.5, 2, 3,

and 5 ms were explored and showed an optimum signal enhancement at the shortest contact pulse. Proton decoupling at ~ 28 kHz was applied during the acquisition of 2016 complex data points. The spectral width was 100 kHz and the pulse delay 15 s. 100 transients were collected at each contact time. The spectra were processed directly on the spectrometer using VNMRJ software with 50 Hz of exponential apodization, zero-filling to 16384 data points, and a left-shift of 5 data points.

We note that there appears to be a difference in the ^{13}C chemical shift referencing in the current ACC/ACMC literature. In our work, all ^{13}C spectra are referenced with respect to TMS via a secondary standard of adamantane. The referencing was found to be consistent with the chemical shift referencing of Papenguth et al. (1998) cross-referenced to calcite at 167.6 and aragonite 169.9 ppm¹⁶⁹. We note that our referencing is -1.1ppm from that of Michel et al.¹¹².

Magnesium (25) NMR

Natural abundance ^{25}Mg NMR spectra were obtained using the quadrupolar Carr-Purcell Meiboom Gill (QCPMG) sensitivity enhancement pulse sequence discussed earlier in this methods section. These experiments involved a spectral width of 250 kHz, $\pi/2$ (90°) and π (180°) pulse widths of 3 μs and 6 μs , respectively; and 5 s pulse delay to acquire from 6,000 to 35,000 transients depending on the signal-to-noise ratio obtained for each sample. The pulse delay was calibrated on a sample of magnesium hydroxide. Spikelet conditions involved application of 40 refocusing pulses with inter-pulse delays of 200 μs to acquire 1,000 data points between each echo maximum, which generates a 250 Hz frequency spacing between spikelet maxima in the FT NMR spectrum. Spectra for all samples were acquired under static and MAS rotor-synchronized conditions. Static spectra are utilized to resolve quadrupolar couplings, because the larger line widths increase the resolution of the spectral singularities required to

quantitatively determine the NMR parameters of the resonances. The MAS spectra were performed at a spin rate of 10,000 Hz and are used in this work to verify agreement between the ^{25}Mg static spectra and the ^{25}Mg NMR spectra of reference phases. Magnesium chemical shifts are referenced to a 1 molar Mg-chloride solution (0 ppm, by definition). Additional references for ^{25}Mg -NMR can be found in the experimental¹⁷⁰ and theoretical¹⁷¹ works of others. All spectra were initially processed using the VNMRJ software available directly on the spectrometer. Spectra were given a zero-fill to a total of 128,000 data points after left shifting the first two data points, which were corrupted, likely due to ringing of the sample coil at the low ^{25}Mg resonance frequency (~ 50 MHz). The final FID also received 20 Hz of exponential apodization before Fourier transformation to the frequency domain.

C. Computational Methods

Quantum Mechanical Calculations

CASTEP NMR calculations make use of density functional theory (DFT) electron pseudopotentials, rather than the full description of core electronic states (Figure 7). This approximation enables a very high accuracy treatment of the valence electrons and excited states to very high energy cutoffs (viz. 610 eV). As the signal of NMR is dominated by valence and excited state interactions, the inaccuracy of the core treatment is of little consequence to the overall accuracy of the chemical shielding calculations. In all cases the Perdew-Burke-Ernzerhof (PBE) functional was used since this form best reproduces equilibrium crystal structure (required for this work) over a newer functional form (version PBE-sol). The newer functional is recommended for dynamics and transition path sampling rather than equilibrium properties.

Furthermore the potential function is evaluated using the generalized gradient approximation (GGA), which is preferred for accuracy over the method of steepest descent. Norm-conserving,

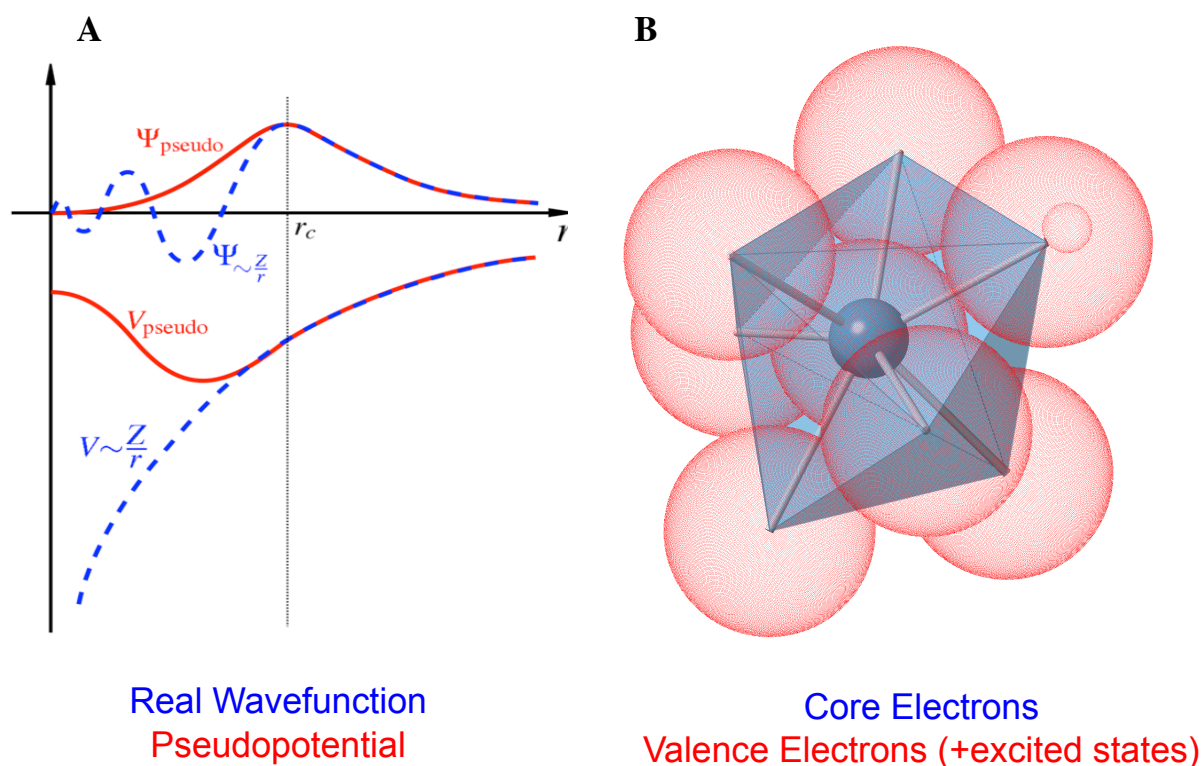


Figure 7. CASTEP NMR calculations make use of electron pseudopotentials that enable very high-level calculations of valence electrons and excited states.

on-the-fly potentials require very high-energy cutoffs but are required for the CASTEP NMR calculation. The CASTEP NMR calculations are performed for reference phases in the Ca-Mg-CO₃-H₂O system that have well-determined X-ray crystal structures and these theoretical calculations (combined with NMR simulations) provide important reference spectra for comparison with the ACC/ACMC/AMC NMR, since these and many of the crystalline phases have not been previously observed/reported by experimental NMR. The accuracy of the CASTEP calculated NMR parameters are verified by comparison of computational results for numerous phases that have been well-characterized experimentally by NMR using the

experimental parameters in the literature, including many of the anhydrous carbonates and calibration compounds such as the oxides and hydroxides of calcium and magnesium (lime, portlandite, brucite, and periclase). These latter compounds have the smallest unit cells and therefore were used for efficient development of appropriate CASTEP convergence criteria. The energy cutoffs and k-point densities were increased until the results of the CASTEP NMR calculation were converged for oxide and hydroxide phases. The k-point density values were similar to the fine/ultra-fine quality settings, but required an additional increase of the energy cutoff from the default value of ~400 to 610 eV. The oxides, hydroxides, and anhydrous carbonate species were used to correlate the isotropic portion of the CASTEP NMR shielding tensors to reported experimental chemical shifts using reference phases, thereby providing an empirical equation to convert the CASTEP absolute shielding to a chemical shift scale. This conversion is necessary for comparison between the calculation-derived and experimentally determined NMR parameters. For calcium chemical shifts the correlation was initially established using lime, portlandite, calcite, and aragonite. The regression between CASTEP NMR shielding tensors and chemical shift was then used to predict the isotropic chemical shift expected for phases where there is no literature NMR data (e.g. MHC, ikaite, dolomite, and Wang's vaterite). Note that although ikaite was not initially included in the correlation produced in 2010, we subsequently determined its ^{43}Ca -NMR spectrum experimentally in 2012 (see Appendix) and therefore ikaite could also be added to the correlation published previously¹⁰¹. All ^{43}Ca CASTEP NMR calculations were performed on the Cobalt supercomputer (of the National Center for Supercomputing Applications) using 8 cores in 2010-2011. CASTEP NMR calculations of calcium carbonate phases was repeated in 2012 by A. O. Yazaydin, for extending

the dataset to include relevant Ca-Mg-CO₃-H₂O phases under the conditions of open access to CASTEP for research in the United Kingdom.

NMR Simulation and Fitting

NMR line shapes at our H₀ magnetic field of 20.0 T were simulated for crystalline polymorphs using the SIMPSON solid-state NMR simulation software⁶³ using the outputs from CASTEP NMR calculations or experimentally determined parameters in the SIMPSON input file. These simulations are necessary extension of CASTEP NMR calculations that produces a simulated spectrum under the relevant experimental conditions. This is especially required for quadrupolar nuclei (⁴³Ca and ²⁵Mg), which have several interactions that scale with the applied magnetic field and MAS. These interactions lead to changes in the line-width (if the second order quadrupolar interaction is significant) and position (arising from the isotropic quadrupolar shift, which is field dependent) when the applied static magnetic field is varied. SIMPSON works by establishing a density matrix for the system of spins under investigation and evolving it through time under the influence of NMR interactions using the Liouville von Neumann equation. The user has control over which NMR interactions are active and what values their parameters have, as well as the typical experimental variables including the spectral width, field strength, spin rate, and the pulse sequence that is employed. In addition, SIMPSON includes pre-packaged “crystallite files”, which are related to the number of unique powder orientations in the sample. For experimental solid-state NMR, there are a nearly infinite number of crystal orientations sampled in the rotor (in the case of fine powders), but it has been well established that only a small subset of these orientations are required to obtain suitable agreement between SIMPSON simulations and experiment.

In this work, SIMPSON is used to visualize the spectra that corresponds to CASTEP NMR properties calculations, determine the appearance of a resonance under different experimental conditions for a given set of NMR parameters (say at a different field to correlate our results with those from lower fields in the literature), or to vary the NMR parameters in an attempt to match the resonance shape obtained from one of our NMR experiments. To calculate the NMR resonances of the reference phases at 20 T, the NMR parameters used as the SIMPSON input were those extracted from the CASTEP calculations discussed in the previous section or those taken from published experimental data. All calculations with SIMPSON were performed using the brute-force method, at the appropriate MAS spin rate with 40 γ -angles (fixed), and the pre-packaged ZCW4180 crystallite file. The simulated spectra all started with the magnetization in the x-y plane (representing an ideal 90° pulse) and assumed that only the central transition was detected, an assumption that is valid in the case of very broad resonances such as those of ^{25}Mg or in cases where MAS experiments are employed. All time-domain simulation results received the equivalent of 50 Hz of exponential apodization prior to performing the fast Fourier transform. SIMPSON calculations were performed at Alfred University using dual-core Intel iMac computers. Experimentally observed resonances for the ACCs were fit with Gaussian and Lorentzian functions using the Abscissa software, a freeware program for Macintosh written by Rudiger Bruhl.

Molecular Dynamics

Molecular dynamic (MD) calculations of pure calcium ACCs were performed in collaboration with A. Ozgur Yazaydin at Michigan State University in the research group of Prof. R. James Kirkpatrick. These were executed using the recently developed fully flexible force field of Raitieri and Gale^{19; 20} for the Ca-CO₃-H₂O system implemented in the DLPOLY

code. MD simulations to test the stability and structure of ACC were performed using the atomic positions determined from RMC modeling by Goodwin et al. as the initial atom positions, as mentioned in the introduction (figure 4). In the work of Goodwin et al., they reported two RMC models of ACC that differed in terms of the starting configuration for the RMC fitting routine, namely monohydrocalcite and a randomly generated mixture of Ca^{2+} , CO_3^{2-} , and water. Although the initial configurations in Goodwin et al.'s modeling were substantially different, both converged to similar structures in the RMC process. The initial configuration for our MD simulations was the final configuration of their model that began with the randomly generated mixture of Ca^{2+} , CO_3^{2-} , and water. This system contained 1620 CaCO_3 formula units and had a $\text{H}_2\text{O}/\text{CaCO}_3$ ratio of 1/1. The RMC-derived structure did not contain positions for the H-atoms of the water molecules, as this information is not available from the total X-ray scattering results that were used in the RMC fitting procedure. Two H-positions were added manually to oxygens of water with using the “Add Hydrogen” feature of Materials Studio. The hydrogen positions were added prior to our MD simulations and equilibrated prior to production runs while all other atom positions were held rigid. The simulations were performed at 298 K and 1 atm under 3-dimensional periodic boundary conditions with DL_POLY2.18, using a 1 fs time step and a 9 Å cutoff. All intermolecular potentials were tapered to zero over a range of 6-9 Å, as described by Raiteri and Gale.² Ewald summation was used to compute the energies resulting from all electrostatic interactions. We first equilibrated the system for 1 ns in the NVT ensemble using a Nose'-Hoover thermostat with a relaxation time of 0.1 ps for temperature control. The system was further equilibrated for 1 ns in the NPT ensemble followed by a 2 ns production run. The barostat of Melchionna et al.¹⁷² with a relaxation time of 1.0 ps was used for pressure control. The results presented in the discussion are from the 2 ns production run that was carried out in

the NPT ensemble. For calibration and validation of our ACC simulations, the forcefield was applied to reference phases of the Ca-CO₃-H₂O system including lime (CaO), portlandite (Ca(OH)₂), calcite (CaCO₃), Wang's vaterite (CaCO₃), Kamhi's vaterite (CaCO₃), aragonite (CaCO₃), monohydrocalcite (CaCO₃•H₂O), and ikaite (CaCO₃•6H₂O) and these crystalline phases were equilibrated and subsequently simulated for a period of 1 nanosecond. All MD simulations were performed on the Carbon supercomputing cluster located at the Argonne National Laboratory using 16 cores.

One important structural element of ACCs and ACMCs that are still a matter of some debate in the literature is the distances between the Ca²⁺ or Mg²⁺ and the oxygen atoms within their immediate coordination sphere. Previous ⁴³Ca NMR work with crystalline materials revealed a linear correlation between the isotropic chemical shift and the mean Ca-O bond distance in anhydrous calcium carbonate materials. This work was augmented and refined for application to amorphous carbonates in the Ca-CO₃-H₂O system as part of this dissertation. To compare the mean Ca-O bond distances from our experimental ⁴³Ca NMR results and from previously published Ca-XAS results for ACC to those determined from our MD simulations, we determined the distribution of mean polyhedral Ca-O bond distances from the RMC model of Goodwin et al. and from our MD simulation, in addition to the normal radial distribution functions (RDFs). The method of polyhedral averaging is illustrated for a single site (figure 8) and for a simulation of ACC based on the Goodwin et al model (figure 9). This “polyhedral averaging” is necessary because solid-state NMR chemical shifts (and their subsequent distribution in amorphous materials) for ⁴³Ca arise from the entire coordination shell, while the Ca-O distances determined from MD to construct an RDF are for individual Ca-O bonds. We calculated a more comparable polyhedral average Ca-O distance for each Ca coordination

polyhedron across the entire MD trajectory (saved every 10000 steps). In this averaging routine, we consider an O-atom from either a carbonate group (O_{CO_3}) or a water molecule ($\text{O}_{\text{H}_2\text{O}}$) to be part of the Ca-O polyhedron if the Ca-O distance is less than 3.0 \AA . This distance is the minimum between the peaks for nearest neighbor and next nearest neighbors in the calculated Ca-O RDFs.

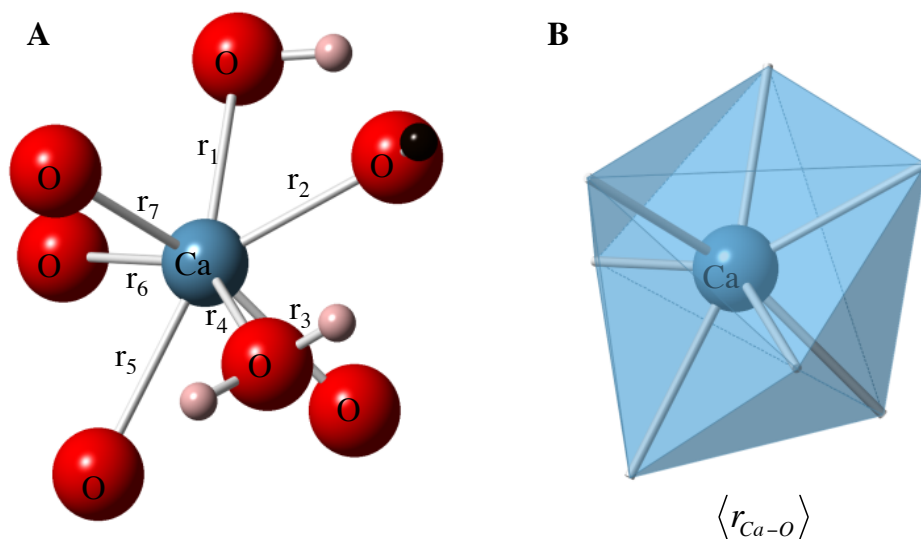


Figure 8. The method of polyhedral averages identifies the coordination environment of each Ca ion (A; illustrated for a single Ca), and produces a single valued bond distance for each Ca ion's coordination environment (B). This type of averaging is appropriate for comparison to NMR data, which inherently samples the mean coordination environment.

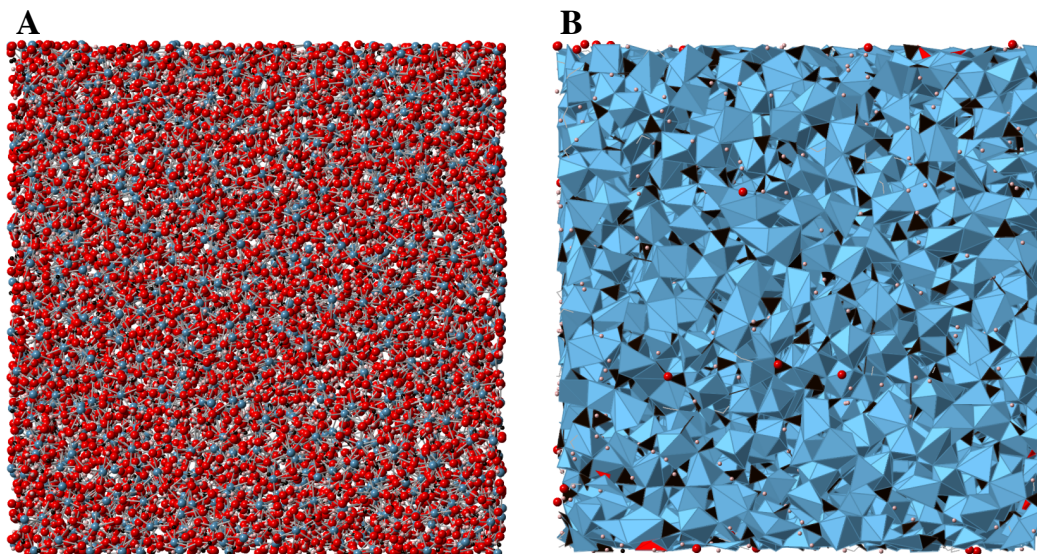


Figure 9. The method of polyhedral averages is extended to the Goodwin et al. structure of ACC shown as ball and stick model A, and as polyhedral representation in B. The method of polyhedral averages was also applied to crystalline reference phases (calcite, Wang's vaterite, Kamhi's vaterite, monohydrocalcite, and aragonite).

RESULTS AND DISCUSSION

A. CASTEP NMR Properties

The ^{43}Ca CASTEP NMR calculations for the reference phases in the $\text{Ca-CO}_3\text{-H}_2\text{O}$ system (Table 2) yield NMR parameters that are in overall agreement with previously published experimental parameters for the anhydrous calcium carbonates, oxides, and hydroxides^{173; 174}, suggesting that CASTEP NMR parameter calculations give good results for ^{43}Ca carbonate phases (Table 4 and 5). For example, figure 10A shows a strong correlation (R^2 of 0.99931) between the calculated ^{43}Ca isotropic shielding and the experimentally determined isotropic chemical shifts for lime, portlandite, calcite, ikaite, and aragonite (experimentally determined values taken from Bryce^{173; 174}).

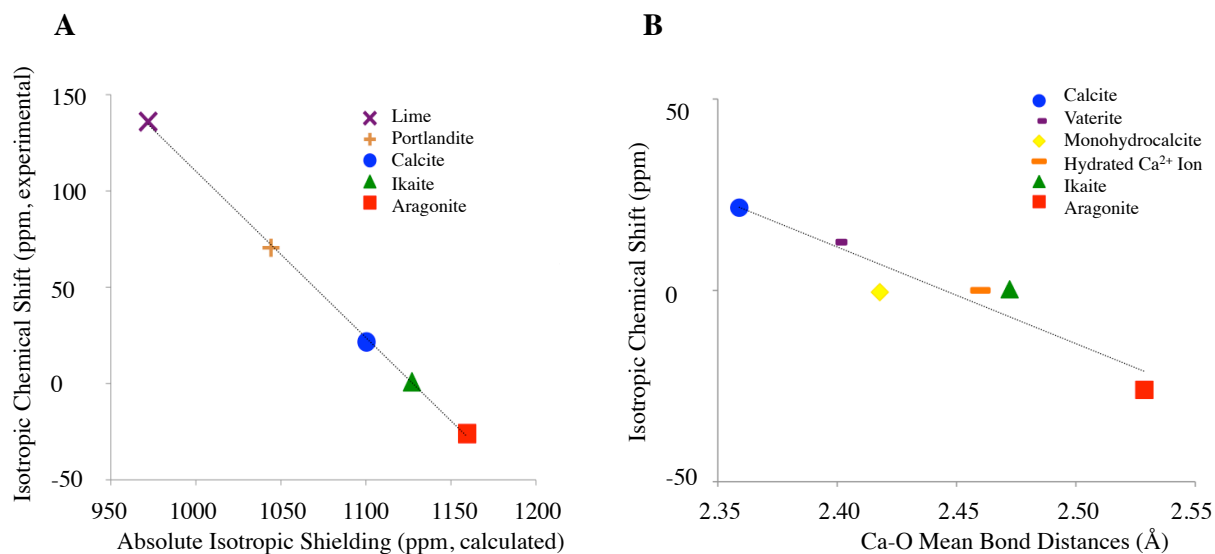


Figure 10. CASTEP calculated ^{43}Ca -NMR parameter (absolute isotropic shielding) correlated with experimentally determined isotropic shifts (A); the correlation coefficient ($y = -0.8639x + 974.1$; $R^2 = 0.99931$) is a testament to the accuracy of the CASTEP code. Mean Ca-O bond distance is also correlated with ^{43}Ca -NMR isotropic chemical shifts and gives good results for the entire $\text{Ca-CO}_3\text{-H}_2\text{O}$ system.

Ideally, like an experiment, one would compute the absolute shielding tensor of the experimental reference phase (often a 1.0 molar aqueous solution) and uses this to convert the computed shielding tensors to the relative chemical shift scale for other phases. However, using CASTEP to determine the NMR properties of liquids turns out to be a very demanding task that requires a large system size and dynamic sampling over many nanoseconds to microseconds. An alternative is to normalize the computational results by computing shielding tensors for several reference materials with high-quality crystal structures and published experimental NMR parameters that span the range of possible structures in your samples of interest. In this study such a correlation-based conversion was originally constructed for Ca-oxides, hydroxides, and the crystalline carbonate phases calcite and aragonite (Figure 10A). The resulting regression equation can then be used to convert the absolute shielding of any computed structure to a relative scale that compares with experimental values, or to predict the isotropic chemical shift of a phase where there is no existing NMR data but a quality structural model, as was done for ikaite prior to its experimental observation (^{43}Ca NMR spectrum of ikaite is included in the appendix). Notably the slope of the correlation differs slightly from the expected value of one; therefore it may always be advisable to use multiple phases for chemical shift referencing in this fashion. The strength of this correlation is largely dependent on the degree of accuracy of the structure determination (usually by X-ray diffraction) and assumes the structure of the NMR samples are sufficiently comparable to the X-ray diffraction-based structure. We note that vaterite and monohydrocalcite were not used to develop this correlation since there is controversy regarding their crystal structures as discussed in the introduction to the reference phases^{146; 147; 148; 149}. Thus any given natural or synthetic sample may not conform to the idealized structure. The potential for various types of disorder in these phases makes it difficult

to compare real materials, structural models, and NMR properties. Owing in part to the high quality ikaite structures determined by neutron diffraction, the ^{43}Ca CASTEP NMR calculations predicted ikaite's NMR properties with high accuracy by this theoretical approach in 2010 (see Appendix). Calcium quadrupolar parameters (quadrupolar coupling and quadrupolar asymmetry) are given here for completeness of the CASTEP results however these will not be greatly utilized in further discussions (Table 4) since the small quadrupole moment of Ca did not give rise to quadrupolar features in the experimentally observed data (see experimental results below). Notably the quadrupolar parameters calculated here for calcite, vaterite, and aragonite do agree with the experimental determinations of Bryce^{173; 174}. Also it is noted that the calculated quadrupolar parameters for ikaite do also agree with our recent experimental observations (see Appendix).

The isotropic chemical shift derived from our CASTEP NMR calculations can be combined with mean Ca-O bond distances of reference phases for an empirical correlation (Figure 10B) that facilitates simple analysis of bond distance information from molecular dynamic computational results. This type of correlation has been observed before for the anhydrous carbonates^{173; 174}, Ca-O distances in organic complexes¹⁷⁵, and across many chemical functionalities¹⁷⁶. In this work the correlation presented by Bryce^{173; 174} was extended beyond the anhydrous phases (calcite, vaterite, and aragonite) to include hydrated calcium ion, monohydrocalcite, and ikaite (Figure 10B; Table 5). This type of correlation has not been previously applied to the analysis of an unknown phase; applying the resulting correlation to our ^{43}Ca NMR data in ACCs and ACMCs allowed us to predict the mean Ca-O bond distance directly from the experimental NMR spectra (See ^{43}Ca NMR discussion below). Incorporation of ikaite, monohydrocalcite, and the hydrated Ca ion into this correlation was an important

advance given the theorized importance of H₂O in ACC/ACMC/AMC formation. Since no ⁴³Ca NMR parameters had been reported for ikaite and monohydrocalcite at the time the correlation was constructed, CASTEP NMR parameter calculations for ikaite and monohydrocalcite and the earlier described absolute-to-relative shielding correlation were key to their inclusion in the isotropic shift/mean Ca-O bond distance correlation.

Magnesium shielding tensors from CASTEP NMR can also be correlated against published experimentally determined isotropic chemical shifts for the anhydrous carbonates oxides and hydroxides with a high degree of agreement (Figure 11A), however there is no similarly straight-forward relationship between isotropic chemical shifts and Mg-O bond distances, as in the case of ⁴³Ca (Figure 11B). For the correlation between the absolute isotropic shielding and isotropic chemical shift (including periclase, brucite, magnesite, and dolomite) we obtain a correlation of $\delta_{\text{iso}} = -0.9099 * \sigma_{\text{iso}} + 511.6$; $R^2 = 0.9983$ (Figure 11A). This correlation differs slightly from the correlation derived from the comprehensive work of Pallister et. al. that correlates experimental and theoretically determined isotropic chemical shifts across many magnesium species (carbonates, sulfates, halides, silicates, nitrides, vanadates, etc...) ¹⁷¹. In spite of the great chemical diversity, the correlation of Pallister et al. has a relatively high correlation coefficient ($\delta_{\text{iso}} = -0.936 * \sigma_{\text{iso}} + 528$; $R^2=0.964$). The reference phases in the Mg-CO₃-H₂O system have relatively small range of bond distances (2.04-2.12Å), as compared to the Ca-CO₃-H₂O system (2.36-2.55Å), and the isotropic shifts regressed versus mean Mg-O bond distances do not provide a correlation with any useful statistical significance (Figure 11B). The calculated CASTEP NMR quadrupolar parameters of Mg-phases do not agree sufficiently with experimental determinations for dolomite, hydromagnesite, and brucite ^{171; 177}. The origin of the discrepancies is not precisely known, but is likely attributable to imperfect materials used in

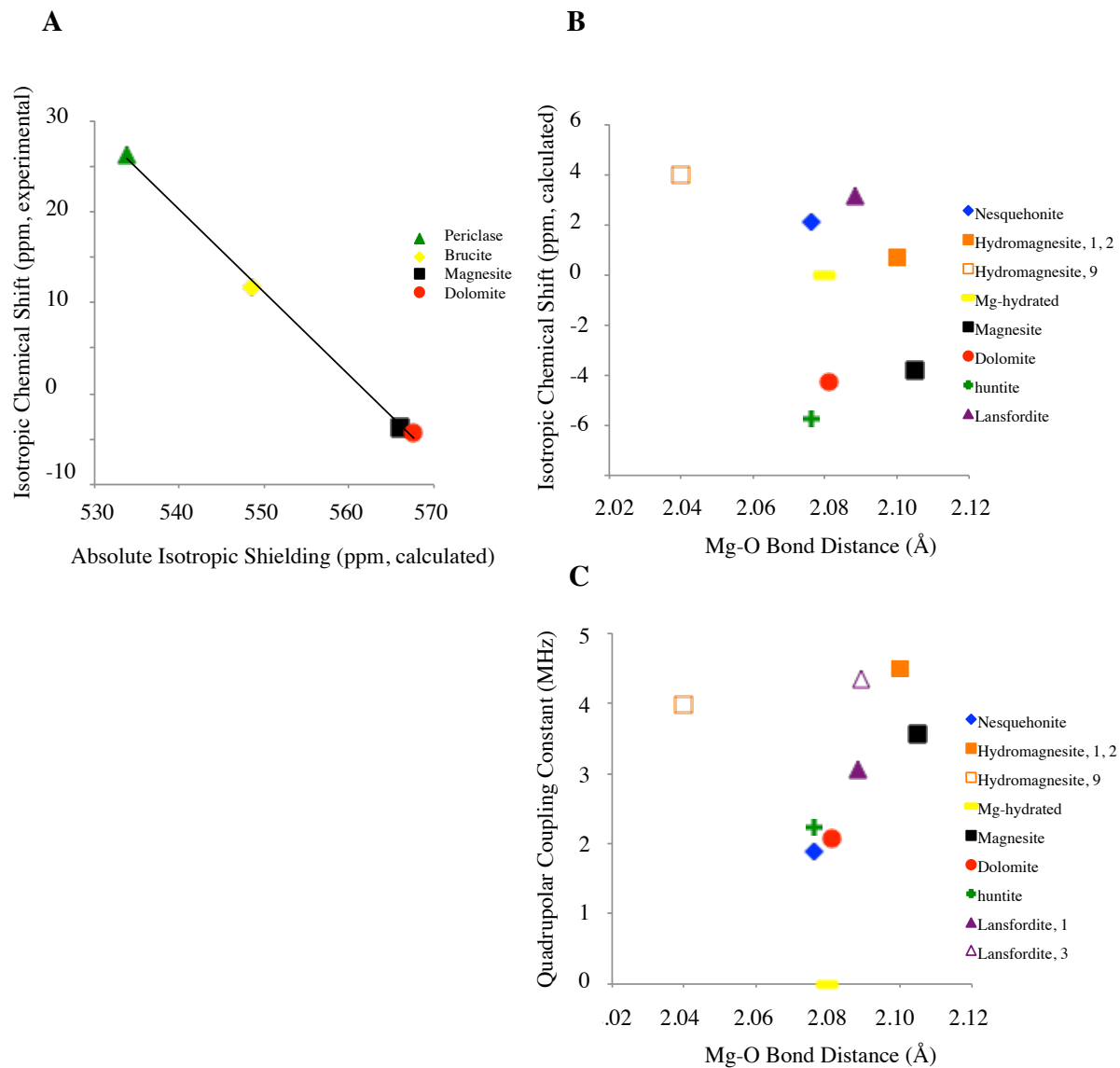


Figure 11. CASTEP calculated ^{25}Mg -NMR parameter (absolute isotropic shielding) correlated with experimentally determined isotropic shifts (A; $-0.909922x + 511.591110$; $R^2 = 0.998324$). Mean Mg-O bond distance is poorly correlated with ^{25}Mg -NMR isotropic chemical shifts (B) and poorly correlated with the quadrupolar coupling constant because geometric factors are increasingly important when the NMR active nuclei have large nuclear quadrupole moments. The Hydromagnesite, 9 site is somewhat of an outlier because it is coordinated by two hydroxyl groups.

the determination NMR parameters and/or limited knowledge of proton positions from X-ray structural studies.

Within the Mg-CO₃-H₂O system, there are structural discrepancies related to hydromagnesite, in addition to many unknown structures, that limit the confidence of Mg CASTEP NMR results and make their value in interpreting experimental NMR results challenging. The only available experimental NMR data for hydromagnesite was interpreted by MacKenzie and Meinhold in terms of two sites, M1 and M2, having isotropic chemical shifts of +14 and -4 ppm respectively¹⁷⁷. However the experimental ²⁵Mg NMR spectra for hydromagnesite were broad and poorly resolved at the relatively low magnetic field (11.7 Tesla). The two-site interpretation of their NMR spectrum was consistent with an older X-ray determination of the hydromagnesite structure¹⁷⁸ but is not in agreement with a later refinement of a three site model that includes the orientation of H-bonding within the structure¹⁷⁹. Our ²⁵Mg CASTEP NMR calculations are based upon the three-site model of hydromagnesite. Within the three-site model, two of the sites do have more similar NMR properties, while one of the sites is highly distinguishable (Table 4). Unfortunately at the lower magnetic field available to MacKenzie and Meinhold there is insufficient resolution in the experimental spectrum for quantitative deconvolution of a three site model. To further examine the inconsistencies we shall average NMR properties of the more similar sites and effectively reduce our three-site calculation results to a two-site model for comparison to the experimental results of Mackenzie and Meinhold. According to the CASTEP NMR calculations presented here for hydromagnesite and the regression from figure 11A, we estimate isotropic chemical shifts about +4 and +0.7 ppm for two distinguishable sites of hydromagnesite. Using the regression of Pallister, the situation is slightly improved giving estimate isotropic chemical shifts about +7.5 and +4 ppm for two distinguishable sites of hydromagnesite. But neither correlation applied to our ²⁵Mg

CASTEP NMR results is sufficient to find agreement with the experimental spectrum of hydromagnesite, which was modeled as to resonances at +14 and -4 ppm. The difference is not reconcilable and may be attributed to an imperfect material used by MacKenzie and Meinhold, or and imperfect structure used in the CASTEP NMR calculation. In addition to this discrepancy, there are several phases that can not be studied by the CASTEP NMR technique because there are no reliable x-ray diffraction based structures, including sergeevite, barringtonite, pokrovskite, artinite, dypingite, and giorgiosite. Future development could be directed toward synthesis and structural refinement of these phases by x-ray and neutron diffraction and by NMR tensor data¹⁸⁰, and enabling a multi-scale understanding of this challenging family of structures.

The CASTEP NMR calculations presented here also show that optimizing the positions of the hydrogen atoms (H-opt) before performing an NMR calculation significantly affects the calculated NMR parameters. This effect has been previously observed in the Mg-NMR work of Pallister¹⁷¹. Proton structural optimization prior to the NMR calculations makes intuitive sense since X-ray structure determinations are inherently insensitive to light elements, meaning that many of the reported and accepted X-ray structures have inadequate information regarding the positions and behaviors of protons. It was further found that some of the reported H-O bond distances in the reference structural refinements were unreasonably short (viz. 0.7 Å) and that these misplaced protons lead to inaccurate CASTEP NMR parameters for all elements in the structure. Neutron scattering is ideally suited for determination of proton positions, however these data are not available for a vast majority of these phases and access to facilities appropriate for performing neutron scattering refinements was not available. In our studies, we opted to optimize the hydrogen positions (H-opt) while maintaining an invariant rigid lattice for all other

atomic positions using the DFT CASTEP geometry optimization routine. The effects on the NMR property calculations can be seen for all hydrated phases (Table 4; see comparison with experimental values for ikaite in the appendix), however there are no general trends observed since the authors of various X-ray structure determination have not all applied proton positions according to a similar scheme.

In general CASTEP NMR property calculations are especially limited with respect to dynamic and disordered phases. Since CASTEP calculations are executed under periodic boundary conditions an exceedingly large cell of many hundreds of atoms is required to capture the "unit cell" of a disordered phase without boundary effects. The computational expense scales super-exponentially with the number of atoms considered since each atom may contain explicit descriptions of several electrons. Pseudopotential calculations and efficient parallelization of the CASTEP code have enabled these calculations for some large systems, but the expense is great. Additionally since quantum calculations are static (effectively 0 Kelvin), there is no allowance for the effects of dynamics. Therefore if dynamic averaging is an important aspect of the structure (such as for liquids), then the static calculation may differ substantially from experimental NMR observations. For example the hydrated-Ca²⁺ cluster calculations (with 6 and 9 water molecules) do not have similar calculated properties as expected for a solvated Ca ion in aqueous solution (zero ppm chemical shift, by definition). Although the geometric configuration of both clusters was optimized before the NMR parameter calculations, the clusters are isolated in vacuum and the NMR properties calculated for these clusters do not reflect time averaging associated with dynamic behavior that would affect the NMR spectrum of real hydrated ions. Since the NMR acquisition period is on the order of micro- to milliseconds, time averaging by processes with correlation times much shorter than these ranges is an important component to

consider in dynamic systems such as a solution or other fluid. Hence, the structures obtained for these systems and the calculated NMR properties do not reflect the experimental expectations for solvated ions. Another emerging solution that can address the effects of both dynamics and disorder from first principals is the work of T. Charpentier and his FPNMR (First Principals NMR) software package^{62; 181; 182; 183; 184}. This approach relies on massive molecular dynamics simulations of very large systems to effectively capture the effects of disorder and defects, followed by CASTEP geometry optimization, and a brute-force CASTEP NMR calculation on such a large system. Time averaged structures might also be used to address the influence of dynamics. Although the technique is very costly in terms of required computer resources, the future application of this approach to chemical simulation of disordered systems can be easily appreciated with growing accessibility to massive computer clusters. On the other hand this approach relies (in part) on the accuracy of the MD force field and complete sampling of phase space on limited MD (ns) timescales.

Table 4. Calcium (43) and Magnesium (25) CASTEP NMR properties calculations for reference phases in the Ca-Mg-CO₃-H₂O system.

Reference Phase Name	Species/Site	Isotropic Shielding (ppm)	Anisotropic Shielding (ppm)	Chemical Shift Asymmetry	Quadupolar Coupling (MHz)	Quadrupolar Shift Asymmetry
Aragonite	Ca	1159.5	47.6	0.41	0.40	0.37
Calcite	Ca	1100.4	11.0	0.00	1.57	0.00
Dolomite	Ca	1113.3	28.6	0.00	1.57	0.00
Huntite	Ca	1135.2	5.4	0.00	1.67	0.00
Ca ²⁺ •6H ₂ O	Ca	1139.7	13.8	0.67	0.45	0.17
Ca ²⁺ •9H ₂ O	Ca	1136.3	27.5	0.61	0.75	0.81
Ikaite	Ca	1131.2	28.6	0.67	2.45	0.39
Ikaite H-opt	Ca	1127.1	23.4	0.54	2.23	0.28
Lime	Ca	971.9	0.0	N/A	0.00	N/A
Monohydrate H-opt	Ca1	1126.7	-26.4	0.25	1.65	0.16
Monohydrate H-opt	Ca2	1128.5	-16.8	0.55	1.67	0.29
Monohydrate H-opt	Ca3	1128.2	-23.7	0.26	1.63	0.14
Monohydrate	Ca1	1122.4	-35.2	0.29	1.94	0.93
Monohydrate	Ca2	1127.5	23.0	0.94	1.61	0.94
Monohydrate	Ca3	1119.8	34.8	0.45	2.34	0.10
Portlandite	Ca	1044.2	-41.0	0.00	2.03	0.00
Brucite	Mg	548.5	-12.3	0.07	-3.19	0.00
Dolomite	Mg	567.6	-6.0	0.00	-2.08	0.00
Huntite	Mg	568.6	-4.2	0.04	-2.23	0.86
Hydromagnesite	Mg1	558.3	12.2	0.50	-3.34	0.67
Hydromagnesite	Mg2	557.4	16.0	0.72	4.62	0.90
Hydromagnesite	Mg9	561.5	19.5	0.09	4.50	0.27
Hydromagnesite H-opt	Mg1	557.3	12.8	0.67	-3.13	0.95
Hydromagnesite H-opt	Mg2	556.0	14.8	0.66	-4.01	0.93
Hydromagnesite H-opt	Mg9	560.3	21.3	0.20	4.48	0.58
Lansfordite	Mg1	558.8	-7.2	0.98	-3.06	0.41
Lansfordite	Mg3	558.8	8.3	0.21	-4.35	0.85
Landsfordite H-opt	Mg1	555.3	12.4	0.63	-4.51	0.34
Landsfordite H-opt	Mg3	556.4	-7.0	0.81	2.16	0.88
Magnesite	Mg	566.1	-3.2	0.00	-3.58	0.00
Nesquehonite	Mg	559.9	-8.2	0.83	1.89	0.89
Nesquehonite H-opt	Mg	559.5	-9.8	0.18	1.48	0.21
Periclase	Mg	533.8	0.0	0.00	0.00	N/A

Table 5. NMR and crystallographic data used in the correlation between Ca-O bond distance (Å) and isotropic chemical shift (ppm) for hydrous and anhydrous Ca carbonates. Our own CASTEP calculations give similar results to previous work by Bryce^{173; 174}. Mean Ca-O bond distances are taken from the literature with work on hydrates (monohydrate and ikaite) attributable to Swainson et al.^{146; 185}, vaterite to Wang and Becker¹⁵⁰, hydrated Ca²⁺ to Politi et al.^{34; 56}, and ion pair to Di Tomasso and De Leeuw⁹⁹. Bold values highlight the data used in the correlation for determination of maximum bond distances.

Phase	Mean Ca-O Distance (Å)	This work**		$\delta_{\text{iso, EXP}}$
		Bryce* $\delta_{\text{iso, CALC}}$	$\delta_{\text{iso, CALC}}$	
calcite	2.36	17.79	23.42	21.6
vaterite	2.40			12.6
monohydrate	2.42	-4.37	-0.47	
ikaite	2.47	-3.68	0.28	
aragonite	2.53	-29.75	-27.83	-26.0
CaO	2.40	120.94	134.62	136.0
CaOH	2.37	62.92	72.07	70.5
Ca ²⁺ 6H ₂ O	2.46			0***
CaCO ₃ ion pair	2.39			

*previously reported by Bryce, 2010: $\sigma_{\text{iso}} = -1.245 \times \delta_{\text{iso}} + 1122.5$ ppm

**original correlation (Figure 10A) used calcite, aragonite, CaOH, and CaO in 2010. Ikaite added in 2012 without significant change. $\sigma_{\text{iso}} = -1.1549 \times \delta_{\text{iso}} + 1127.4$ ppm ($R^2 = 0.9992$)

***arbitrary designation as the zero point reference

Table 6. NMR and crystallographic data used in the correlation between Mg-O bond distance (Å) and isotropic chemical shift (ppm) for anhydrous and hydrous Mg carbonates. Our own CASTEP calculations differ substantially from certain results experimental results of Pallister et al. and MacKenzie and Meinhold^{171; 177}. Particularly the three site model for hydromagnesite (Table 4) is reduced to a two-site model for comparisons discussed within the text.

Phase, Site	Mean Mg-O Distance (Å)	CASTEP $\delta_{iso,CALC}$	Experiment $\delta_{iso,EXP}$	CASTEP $C_{Q,CALC}$ (MHz)	Experiment $C_{Q,EXP}$ (MHz)
Magnesite	2.105	-3.48	-3.8	3.58	2.244
Dolomite	2.081	-4.90	-4.3	2.08	0.9
Nesquehonite	2.076	2.11		1.89	
Lansfordite, 1	2.0885	3.17		3.06	
Lansfordite, 3	2.0894	3.17		4.35	
Hydromagnesite, 9	2.04	0.70	-4	3.98	3.1
Hydromagnesite, 1, 2	2.1	3.99	14	4.50	3.6
Mg-hydrated*	2.08	0.00		0.00	
Huntite	2.076	-5.78		2.23	

*Hydrated Mg is defined as having zero valued isotropic chemical shift and has zero valued C_Q by dynamic averaging in solution. Hydrated Mg bond distance taken from Mg-EXAFS of Politi et al.^{34; 57}.

B. Carbon (13) NMR

The compositional span from Ca-rich (x=0) to Mg-rich (x=1) ACC/ACMC/AMC does show a small, but statistically significant change in the ^{13}C chemical shift between ACC and AMC of ~5 ppm, with the peak maxima for the ACMC resonances positioned intermediate to the endmembers (Figure 12). The total ^{13}C isotropic chemical shift range amongst all carbonate containing species is rather small¹⁶⁹ due to the shielding of the ^{13}C by the oxygen in the carbonate polyatomic ion. Therefore all structural effects in ^{13}C NMR of carbonate compounds arises indirectly from second nearest-neighbors. Qualitatively the ^{13}C NMR spectra of the carbon environments indicates the ionicity at the center of the CO_3 polyatomic ion (whether the environment pushes, pulls, or distorts the carbonate polyatomic ion). To explain the trend in ^{13}C

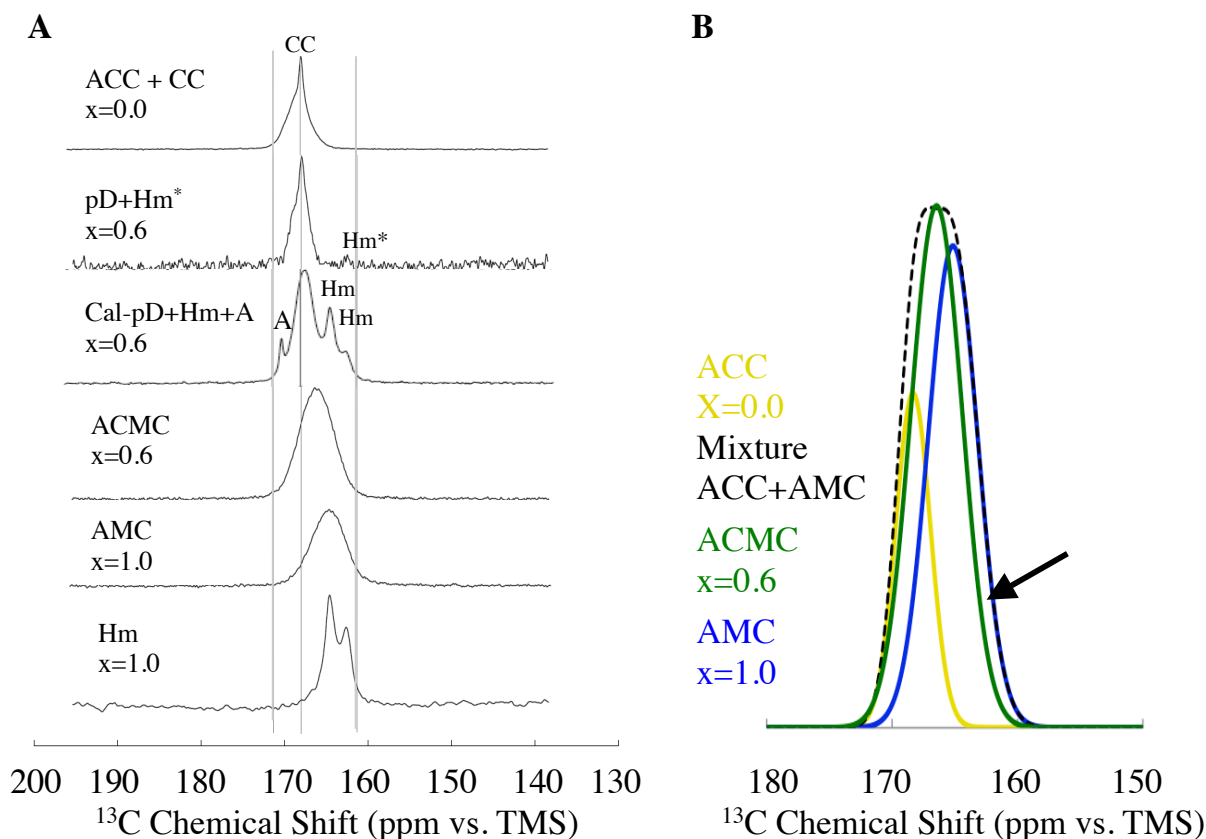


Figure 12. Carbon (¹³) NMR of amorphous carbonates and crystalline reference phases (A) and comparison of ACC, ACMC, and AMC to a mechanical mixing model (B). Arrow denotes the region of low-frequency mismatch between ACMC (green) and AMC (blue). This region of mismatch challenges the nano- phase separation model of ACMC $x < 0.5$ put forth by Radha et al.¹⁰². ACC=amorphous calcium carbonate; CC=calcite; pD=stoichiometric protodolomite ($x=0.5$); Hm*=defective hydromagnesite; Hm=hydromagnesite; Cal-pD=calcian protodolomite ($x=0.47$); A=aragonite; ACMC=mixed magnesium calcium carbonate ($x=0.6$); AMC=amorphous magnesium carbonate ($x=1.0$).

chemical shift with Mg/(Mg+Ca) ratio observed in our experiments, we might (incorrectly) think of the different influence of Mg and Ca on the carbonate polyatomic ion. However, this trend appears to be opposite some of the existing literature, for example, the isostructural series of rhombohedral carbonates including calcite CaCO_3 , dolomite $\text{CaMg}(\text{CO}_3)_2$, and magnesite $\text{Mg}(\text{CO}_3)$ show very small chemical shift range that depends on the fraction of magnesium (from 167.5 to 169 ppm¹⁶⁹), but magnesite is shifted slightly in the high frequency direction—opposite

to the trend observed for increasing fractions of magnesium in the amorphous compounds. Alternatively, there are several other ways to explain this deviation in ^{13}C chemical shift trend with increasing Mg content in our ACC/ACMC/AMC samples. One is that we would expect the asymmetry of the carbon site to influence the chemical shift to some degree, and the ACC/ACMC/AMC samples are very likely to be far less symmetric than the rhombohedral phases, which are the most symmetric structures. Mg-content in the amorphous phase is also likely coupled to structural water content in the ACMCs and AMCs. Water interacts strongly with carbonate ions and therefore water-carbonate hydrogen bonding is also likely to affect the carbon shielding. This second option is supported by our results showing hydromagnesite resonances at the lowest ^{13}C resonance frequencies. Hydromagnesite possesses carbonate-water hydrogen bonding ¹⁷⁹ which is a likely source of the Mg-related carbon deshielding in ACMCs. However, we note that ikaite's ^{13}C spectrum does not follow this rule (ikaite ^{13}C NMR spectrum not shown in figure 12, see Appendix) and therefore the ^{13}C chemical shift cannot be interpreted accurately in terms of a single structural variable. As discussed earlier, proton cross polarization experiments can shed some independent perspective on the spatial proximity of H to C. Thus anhydrous structures will show no signal with proton CP and the rates of CP (variable contact time) are proportional to the ^1H - ^{13}C distances. Proton-carbon cross polarization (^1H - ^{13}C CP) showed that there is H_2O within a small distance of carbonate groups in all the ACMC samples, however the variable contact time profiles are essentially identical for the ACC-ACMC-AMC phases. Notably the ^1H - ^{13}C CP data of the sharpened protodolomite resonance does not show any H_2O near the carbonate groups. We will revisit Figure 12 with respect to the specific details of protodolomite (pD) and calcian protodolomite (cal-pD) and their assemblages with hydromagnesite (Hm) in section E. Dolomite Crystallization.

The ^{13}C NMR spectra also suggest that the ACMCs produced from synthetic seawater have Mg/Ca present as a solid solution above $\text{Mg}/(\text{Mg}+\text{Ca}) = 0.6$ rather than a phase-separated mixture. As mentioned in the introduction, Radha et al. proposed a theory suggesting that ACMCs in the compositional range of the work in this thesis exist as either Mg/Ca solid solution or separate phases depending on the $\text{Mg}/(\text{Mg}+\text{Ca})$ ratio¹⁰². ^{13}C NMR spectra of the endmember compositions are compared to an ACMC spectrum in figure 12B. The endmember compositions are well resolved, and their simple summation is equivalent to a mechanical mixing model

$$f_1x_1 + f_2x_2 = \langle x \rangle \quad \left| \quad \sum_i f_i = 1 \quad \text{Equation 1} \right.$$

using arbitrary fractional intensities to produce a 'flat-topped' resonance shown as a black dotted line. In addition, if the intensities of these endmembers are reduced such that they do fall within the span of the green ACMC resonance, there is a substantial fraction of the total intensity that cannot be described as a mixture of phase-separated ACC and AMC. The ACMC spectra are well fit by single Gaussian functions, suggesting that a multi-peak fit of the ACMC intensity is unnecessary and that a Mg/Ca solid solution exists at this ACMC composition. We also note that the AMC and ACMC resonances are notably wider than ACC, and hypothesize that the additional width may be due to a wider range of structural environments (increased numbers of H-bonds, stronger H bonding) which are also convoluted with the effects of H dipolar broadening. The spectra also show that the low frequency tail of AMC extends beyond the limits of the ACMC resonance, suggesting that there is not phase-separation of pure Mg domains in ACMC $x=0.6$. Admittedly, if our hypothesis is correct regarding the influence of hydration on chemical shift, then these observations could be induced by subtle differences in sample processing (aggregation and mesoporosity, MeOH wash efficiency, subsequent exposure to

atmosphere, etc..). Although the generality of Radha et al.'s results are questionable this experiment would require further elaboration for a definitive comment on phase separation.

The ^{13}C NMR chemical shift of pure Ca ACC is centered on calcite, rather than on vaterite as observed and predicted by Gebauer for ACC synthesized at high supersaturation⁵⁵. Our ACC data are shifted to even lower frequency than those of Michel et al. who argued based on ^{13}C data that their ACC was intermediate between calcite- and vaterite-like¹¹². Our data presented here suggests that ^{13}C NMR chemical shifts may be significantly affected by the presence of hydrogen bonding with water, and this is likely to induce a comparable range of chemical shifts to that observed for all 'nominally' anhydrous phases¹⁶⁹. The ^{13}C NMR of ACC data that has been previously interpreted in terms of calcite-vaterite polyamorphism is more likely a function of water content and therefore very sensitive to sample handling (drying agent, drying time, ambient temperature and relative humidity, etc...). Thus these authors must be exceedingly cautious to not interpret their ^{13}C data of ACC in simple terms of anhydrous geometric arrangements.

C. Calcium (^{43}Ca) NMR

Studies involving solid-state ^{43}Ca NMR are rarely found in the literature prior to the year 2000 due to extreme sensitivity limitations associated with the only NMR-active calcium isotope (^{43}Ca). However, ^{43}Ca NMR remains a promising technique for understanding the molecular-scale structural and dynamical behavior of alkaline earth metals in inorganic, organic, and hybrid materials because ^{43}Ca has the smallest nuclear quadrupole moment of any of the alkaline earth metals (-4.08 mQ/barn versus magnesium at -199.4 mQ/barn). This means that ^{43}Ca generates relatively narrow resonances that enhance our ability to resolve unique structural environments

and presents lesser sensitivity challenges than the other alkaline earth metals (provided you can overcome the abundance issues). With the development of high field magnets that eliminate many of the problems associated with the low gyromagnetic ratio of ^{43}Ca (causing a low resonance frequency that challenges spectrometer electronics), the last ten years have seen an explosion of ^{43}Ca NMR studies at both natural abundance and in ^{43}Ca -enriched materials including the crystalline Ca-carbonates, apatites, and many other inorganic and organic solids (101; 173; 174; 175; 176; 186; 187; 188). Due to the large widths that arise from chemical shift dispersion in amorphous materials, ^{43}Ca enrichment is especially required to study poorly crystalline materials in any detail via ^{43}Ca NMR. Given that 1g of 60% $^{43}\text{CaCO}_3$ costs ~\$60,000-\$100,000, the ^{43}Ca enriched ACC and APMC samples studied in this work represent a challenging and promising step forward in our understanding of structure in these important amorphous materials.

The ^{43}Ca -NMR spectra of four ACC/APMC samples obtained immediately after sample synthesis are essentially identical (Figure 13, NMR results; Table 7) despite their wide-ranging compositional differences (Table 8), suggesting that the structural environment of Ca^{2+} in ACC and APMC synthesized by our route is not substantially affected by Mg^{2+} or water content of the solid phase. The spectra consist of broad, featureless resonances with weighted mean chemical shifts between 0.0 and -0.8 ppm (Figure 13; Table 7) that depend on the Mg^{2+} content of the parent solution rather than Mg content of the solid. The line widths of the resonances cover a large frequency range (FWHM = 26.5 – 28.9 ppm) and overlap with the full line shapes of all the known crystalline anhydrous and hydrated calcium carbonate species in the Ca-CO₃-H₂O system (Figure 13, CASTEP+SIMPSON results). Although the number of samples is insufficient for a rigorous analysis, it appears that the resonance width may narrow slightly at lower temperatures (Table 7), but more than two synthetic temperatures would be required to test this weakly

Table 7. Peak positions and line widths for the ACC samples in this study determined by fitting the resonances to single Gaussian functions, corresponding to spectra in Figure 13. *After subtraction of Lorentzian fit for calcite ingrowth. **After subtraction of Lorentzian fit for coexisting calcite and aragonite.

	a) High-Mg, Low-T		b) High-Mg, RT		c) Low-Mg, RT		d) Mg-free, low-T*		e) Low-Mg, RT**	
	Mean	Error	Mean	Error	Mean	Error	Mean	Error	Mean	Error
mean chemical shift (ppm)	-0.77	0.07	-0.77	0.04	-0.12	0.04	0.01	0.04	4.42	0.04
FWHH (ppm)	28.88	0.04	26.50	0.04	26.91	0.06	28.06	0.09	14.55	0.04
Chi²	5.29		1.51		3.38		5.83		0.78	

Table 8. Synthesis conditions and compositions of ACC of Figure 13.

*replicate samples synthesized at Alfred University for compositional analysis

Notes: Cation determination is normalized such that Ca+Mg+Na=1; H₂O determination (<250°C) is given as weight percent of total.

Sample Description	Mg/Ca_{solution}	T°C	Ca	Mg	Na	H₂O	Cl	Si
Low-Mg, RT	>0.05	20-25	0.93	0.05	0.03	10%	<0.01	<0.01
Mg-free, low-T	0	2-5	NA	NA	NA	NA	NA	NA
Mg-free, low-T*	0	2-5	0.99	0.01	0.01	15%	ND	ND
Mg-free, low-T*	0	2-5	0.99	0.00	0.00	15%	<0.01	ND
High-Mg, RT	5	20-25	0.44	0.51	0.05	40%	<0.01	<0.01
High-Mg, low-T	5	2-5	0.99	0.00	0.01	30%	<0.01	<0.01

supported observation. The peak maxima for the amorphous carbonates are near the centers of intensity for monohydrocalcite and ikaite at 20 T. In their breadth and lack of singularities, however, the resonances resemble the NMR spectra of many glasses, indicating that ACCs synthesized by our route are highly disordered at the molecular scale and that a continuum of Ca²⁺ environments is present. The line shapes are best fit by single Gaussians (Table 7),

supporting these conclusions. Spectral resolution was calculated to be 0.04 ppm and is used as a minimum fit error in Table 7 in cases where smaller errors were calculated during the fitting procedure. Unfortunately due to instrument time limitations, multiple syntheses for the various samples could not be compared to quantitatively evaluate the combined synthetic-analytical precision of these results.

These symmetrical line shapes and lack of quadrupolar features suggest that the second-order quadrupolar interactions do not greatly affect the observed resonances. Data from a second magnetic field or multiple quantum NMR experiments are needed to directly quantify any residual influence of the quadrupolar interaction on the observed peak maxima and widths, however even without such quantification the results are immediately significant in regards to the prediction of "vaterite-like" ACC at high degrees of supersaturation. The work of Gebauer et al. has suggested that with increasing supersaturation, there is a conversion from calcite-like to vaterite-like ACC and under these experimental conditions one might reasonably infer that we are beyond the quasi-equilibrium of the calcite-like region⁵⁵. As can be seen from the CASTEP NMR calculations (figure 13; CASTEP+SIMPSON results) the large quadrupolar coupling is the salient distinguishing feature of a vaterite-like local environment. Hence, the lack of significant quadrupolar features positively excludes a vaterite-like local environment and calls into question the appropriate nature of *polyamorphisms* that are "coined" after crystalline analogs. It appears that under our experimental conditions that the ⁴³Ca local environments are entirely indistinguishable. A very recent review acknowledges the existence of the unstructured variety of ACC, without recanting the existence of vaterite-like ACC. Further NMR experiments are needed that utilize the exact methods of Gebauer to establish the transition between vaterite-like ACC and one that is totally unstructured.

Although the range of mean chemical shifts is small (0.0 to -0.8 ppm), it is systematically related to the [Mg] of the parent solution rather than the actual amount of Mg incorporated into the ACC precipitate (Table 7, Table 8). This highlights the possibility of the indirect mechanism by which Mg in solution affects the CaCO₃ cluster through moderation of kinetics. At low synthetic temperatures Mg is effectively excluded from the solid, yet the subtle change in the ⁴³Ca chemical shift (-0.8 ppm) and the overall water content (Table 7 and 8) are most similar to room temperature ACCM that contains the highest Mg concentration in the solid. From the previous ¹³C data (figure 12) and inferences taken from ¹H-¹³C cross polarization, it is highly likely that water becomes hydrogen bonded to carbonate (in increasing numbers and/or stronger H-bonds) for all intermediate ACCM compositions. Because of Mg's high hydration energy, the dynamics of H₂O within the hydration shell of Mg are dramatically different from those of bulk water and of other less strongly hydrated cations like Ca. We might infer that hydration shell of Mg facilitates the formation of stronger carbonate-water hydrogen bonding. This H-bonding that initially requires Mg may persist in the ACC particle with or without the Mg ultimately being incorporated into the solid structure. The strength and/or number of water-carbonate H-bonds does not occur to the same degree under Mg-free parent solution.

The ⁴³Ca-NMR spectra of our ACC samples acquired after aging provide new insight into the transformation of ACC to the crystalline phases and show that the composition of the sample has significant effects on the transformation and crystallization behavior. The High-Mg, RT sample, which has a high Mg-content and the largest H₂O-content, is the most stable, exhibiting an unchanged ⁴³Ca NMR spectrum after intermittent exposure at 50°C and 100% RH ex situ for 1 week. It remained amorphous by X-ray diffraction after storage under ambient conditions for

~100 days (Figure 14c) and after more than one year the sample shows poorly crystalline aragonite.

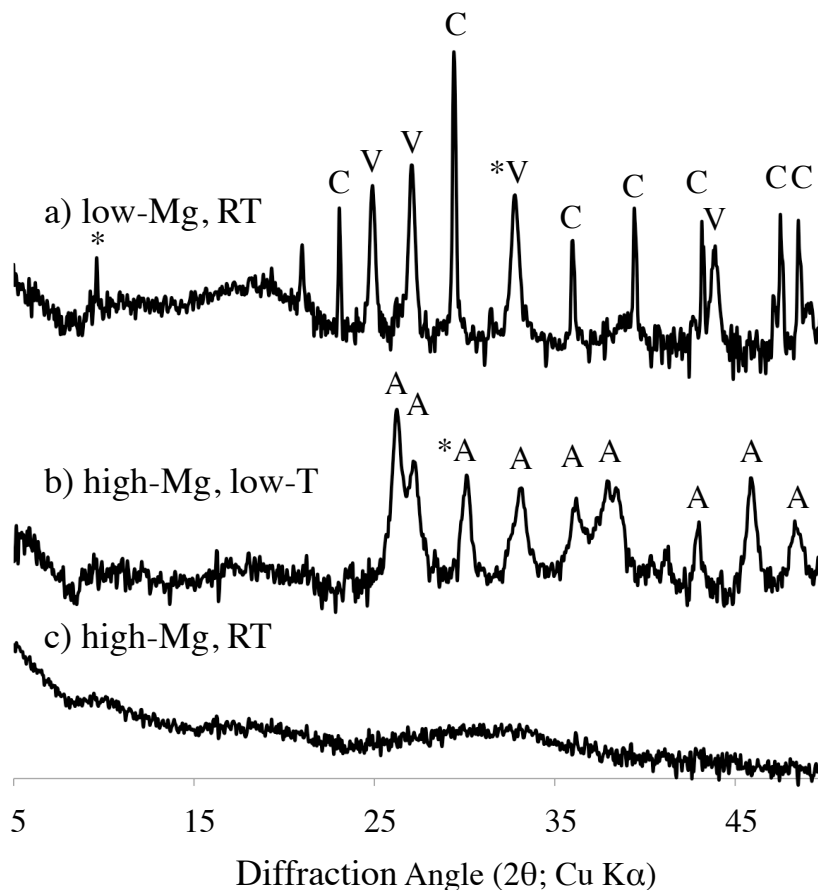


Figure 14. Logarithm of background corrected XRD patterns for ACC samples synthesized at PNNL after storage in ambient conditions for ~100 days. Unusual peak positions or relative intensities are denoted by *.

The ^{43}Ca -NMR spectra of the High-Mg, low-T sample, which contains virtually no Mg or Na but has a relatively high H_2O -content, do not change after intermittent exposure to 50°C and 100% RH for one week (redundant NMR-spectrum is not shown), but after ~100 days of storage at ambient conditions it transformed to a poorly crystalline aragonite as observed by XRD (Figure 14b). The low-Mg, RT sample, which has a Ca/Mg/Na ratio of 93/05/03 and a water content of 5% crystallized when held overnight at 50°C and 100% RH. Its spectrum contains resonances

for calcite at +20.1 ppm (FWHH = 1.9 ppm) and aragonite at -26 ppm (FWHH = 1.1 ppm) along with a relatively broad resonance centered at 4.4 ppm (FWHH = 14.6 ppm) (Figure 13). This medium-sized resonance is nearly featureless and symmetric. Its width is much less than the resonance of the initial amorphous sample. Its center of mass is near the expected chemical shift of vaterite (Figure 13). Using the correlations of Figure 10 one can compare the chemical shift of this unknown site to MD polyhedral averaging of Kamhi's vaterite. The comparison (shown in purple dashed line) reveals a close correspondence between Kamhi's vaterite and the experimentally observed phase. After ~100 days of storage at room conditions, X-ray diffraction shows the presence of only calcite and vaterite in this sample (314a). This further confirms that the broad resonance in the crystallized product represents the local environments of the disordered vaterite structure. Although no aragonite is observed in the XRD of the low Mg, RT sample by XRD, because aragonite is the preferred high pressure phase it is possible that aragonite could form reversibly in the sample during MAS at 10,000 Hz (equivalent G-force of 112), or that the aragonite crystallites are too small for detection by diffraction techniques. The Mg-free, low-T ACC began crystallization to calcite during the initial 5 hours of NMR analysis at 0°C, as shown by the low intensity resonance at 19.6 ppm in Figure 13 (NMR: Mg-Free, LT). The spectrum of this sample does not show the presence of vaterite as an intermediate phase, as observed in a recent in-situ synchrotron XRD study of Mg-free and Mg-rich ACC crystallization at 7.5°C by Rodriguez-Blanco et al ^{106; 189}. Although our data suggest that the rate of transformation of our ACC samples depends on the Mg- and H₂O-contents, one must be cautious in interpreting the transformation rates obtained from MAS NMR since conditions in the MAS rotor are different than what one would observe in the field or in other experimental studies. For example, there was excess water (parent solution) present in the in-situ X-ray study of

Rodriguez-Blanco et al.,^{106; 189} whereas our NMR samples were in contact with the dry nitrogen atmosphere of the NMR probe head. Therefore it might be inferred that the availability of free water directs a different structural pathway, than what we have observed in the NMR. The effects of a dry nitrogen atmosphere on the water content of the ACC is uncertain and it is known that continuous exposure to the parent solution or excess moisture accelerates ACC crystallization. Thus, the experimental conditions may direct the specific crystallization mechanism in the experiments of Rodriguez-Blanco et al. The ¹³C NMR results of Gebauer et al.⁵⁵ suggest that ~kHz sample rotation in an NMR probe may influence the transformation rate and presumably the mechanism. The effects of temperature and humidity cycling are also difficult to evaluate and likely influence any quantitative measurement of transformation rates and mechanisms.

Within the range of experimental conditions relevant to the Ca-NMR spectra, H₂O contents of amorphous carbonates (calculated as TGA weight loss below 250°C) ranges widely from 10–40 wt. %, with large water contents correlating with high Mg²⁺ concentration in the parent solution but not necessarily in the sample (Figure 15; Table 8). The high-Mg, RT sample contains 40 wt. % H₂O, which corresponds to a H₂O/CO₃⁻² ratio of 2.0 for the Ca/Mg/Na 44/51/05 composition. The high-Mg, low-T sample (Ca/Mg/Na = 99/00/01) is also highly hydrated (30% wt. %), corresponding to a H₂O/CO₃⁻² ratio of 1.67. In both cases the dehydration (<250°C) occurs in multiple steps that are different between the High-Mg samples. The low temperature synthesis shows chemical water that decomposes characteristically similar to monohydrocalcite at 210°C; meanwhile the high-Mg, RT sample shows some evidence of multiple types of water that dehydrate gradually at different rates. The Mg-free, low-T sample (Ca/Mg/Na = 99/00/01) and low-Mg, RT sample (Ca/Mg/Na = 93/05/03) have 15 and 10 wt. %

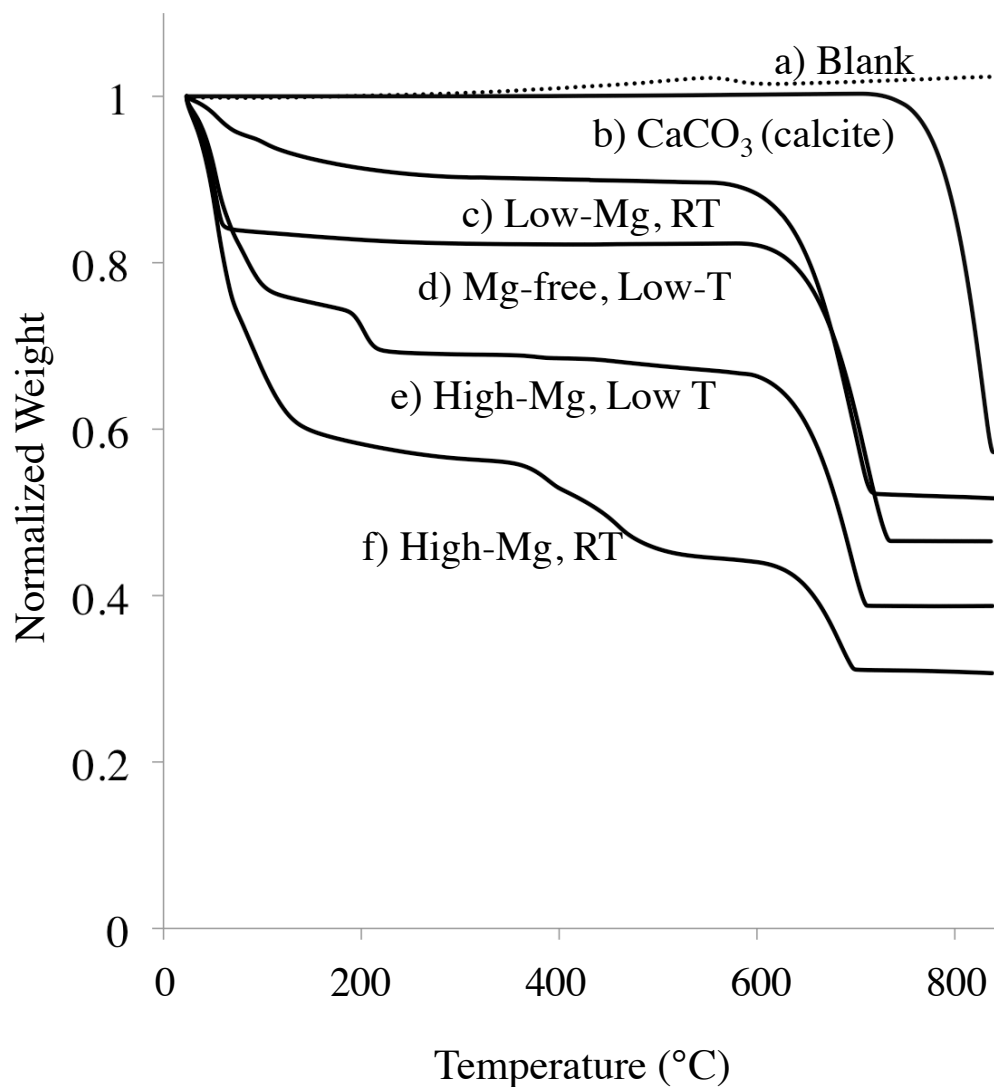


Figure 15. TGA of samples associated with Figure 10. TGA of synthetic ACC indicating labile water contents ranging from 10-40 weight percent (<250°C), monohydrate decomposition (~210°C), and multi-stage decomposition of mixed Na, Mg, Ca carbonates (350-500°C).

H₂O, corresponding to H₂O/CO₃⁻² ratios of 0.83 and 0.28 respectively. Both samples synthesized at RT show the most rapid dehydration below 100°C and have the highest Na contents. Thus, the water molecules in the various ACC-ACMC exist in multiple states including free water, hydration of Mg²⁺, and possibly hydrated Ca²⁺ environments such as

those in ikaite or monohydrocalcite (MHC), or in larger Ca-deficient domains as proposed by Goodwin et al.²¹.

The TGA results also provide some evidence regarding the location of residual Na observed in the EDS compositional analysis. The residual Na content may be related to physically trapped water from the parent solution and some similarity can be seen in the earliest dehydration of the two Na-bearing samples [high-Mg, RT (Ca/Mg/Na 44/51/05) and low-Mg, RT sample (Ca/Mg/Na = 93/05/03)] that were both synthesized at room temperature conditions. This initial dehydration behavior is faster for samples synthesized at room temperature than for those synthesized at high temperatures (Figure 15).

The thermal decarbonation of the ACCs and ACMCs via TGA at higher temperatures (>250°C) reveal the presence of several decarbonation steps (Figure 15), suggesting a segregation of Mg and Ca domains during decomposition or crystallization behavior induced by the TGA process for samples that contain high Mg in the solid phase. The thermal decarbonation of the high-Mg, RT sample occurs in multiple steps that includes decomposition similar to Mg-carbonate domains at 400-500°C¹⁹⁰ and with complete CaCO₃ decomposition occurring near 700°C—lower than for other amorphous carbonates and well below that of crystalline calcite. The well-separated decarbonation events may imply that a phase separation has occurred (either during dehydration or immediately prior to decarbonation via a distillation-type mechanism or zone refinement). This may also be explained by the inferences of Radha et al, that Mg-rich ACMC ($x > 0.5$) are phase separated¹⁰², although our ¹³C and ⁴³Ca NMR have not given similar evidence. It is generally thought of ACC and ACMC that during the dehydration process rearrangements are possible that lead to crystallizations or phase separations. However for the high Mg, low-T sample the subtle variations around 400-500°C

may also indicate a phase separation of trace magnesium. For the remaining samples, the decarbonation is not characteristic of pure Mg-carbonates, implying that any trace of Mg is included in solid solution with Ca or completely absent from the sample (consistent with expectation based upon the EDS compositional analysis).

Ca-O Bond Distances in ACC

The ^{43}Ca isotropic NMR chemical shifts (δ_{iso}) of crystalline phases are known to correlate with mean Ca-O bond distances of nearest neighbors, with the chemical shift becoming progressively more negative with increasing mean Ca-O bond distance.^{173; 174; 175; 176; 191} The correlation we obtain for just the hydrous and anhydrous calcium carbonate phases (Figure 10) [$\delta_{\text{iso}} = -252.68 * x_0 + 617.77$, $R^2 = 0.888$, where x_0 is the mean Ca-O for the crystalline phase and δ_{iso} is the isotropic chemical shift] is a substantial improvement over that presented in the work of Bryce^{173; 174} that includes only the anhydrous phases calcite, vaterite, and aragonite. The inclusion of hydrated phases (monohydrocalcite, ikaite, and hydrated Ca) greatly improves the confidence of bond-length determinations in the Ca-CO₃-H₂O system and highlights the structural similarity of carbonate-Ca and water-Ca interactions. Based on this correlation the maximum mean Ca-O distance for our ACC samples is $2.45 \pm 0.01 \text{ \AA}$, independent of the Mg/Ca/Na ratio and water content. The small difference in the ACC-ACMC chemical shift that is related to [Mg] of the parent solution (0.8 ppm range) propagates no statistically significant difference to the mean bond distance determination within the scatter in the correlation (Figure 10). Mean bond distance determination is within and near the upper end of the range of mean Ca-O bond distances observed for many different synthetic and biogenic ACCs using Ca-XAS (2.27 to 2.49Å; Figure 16; Table 9)^{31; 49; 52; 53; 56; 140; 192}. Use of our correlation in this way assumes that residual second-order quadrupolar effects do not significantly affect the peak

Table 9. XAS-determinations of Ca-O bond distances and coordination numbers from natural samples of amorphous carbonates previously reported in the literature.

Sample Description	Mean Ca-O (Å)	CN	Reference
synthetic ACC	2.43±<0.01	7±0.6	[129]
Ca ²⁺ _(aq)	2.46	8	[129]
Woodlouse	2.38	3.8	[134]
Woodlouse	2.27	NA	[134]
Woodlouse	2.31	NA	[134]
Woodlouse	2.36	NA	[134]
Woodlouse	2.37	NA	[134]
Woodlouse	2.44	NA	[134]
Synthetic, Vacuum	2.41	5.3	[135]
Synthetic, 100°C	2.4	5.7	[135]
Synthetic, 190°C	2.39	6.4	[135]
Snail Eggs, 72 hrs.	2.44	9	[136]
Lobster Carapace	2.35	5.8	[137]
Lobster Carapace	2.35	6 (fixed)	[137]
Plant Cystolith	2.32	5.6	[137]
Plant Cystolith	2.32	6 (fixed)	[137]
Monohydrocalcite	2.42	8.2	[91]
Ficus cystolith	2.49	8	[31]

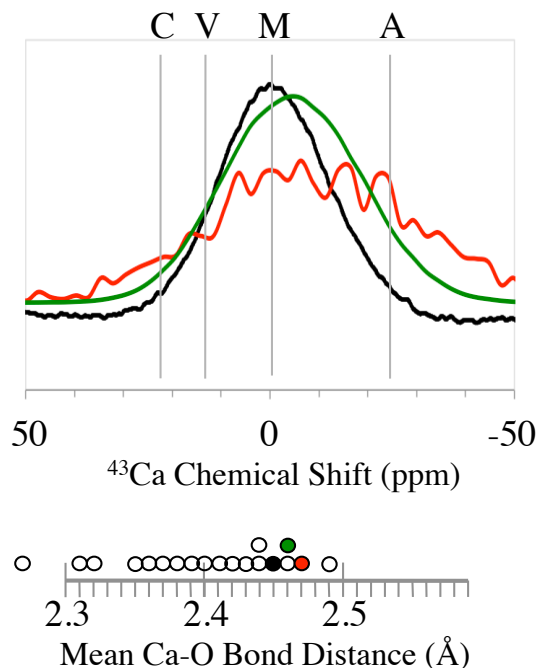


Figure 16. Comparison of experimental NMR with results derived from models and X-ray Absorption Spectroscopy. Previously published mean Ca-O bond distances and coordination numbers for synthetic and naturally occurring amorphous carbonates determined by X-ray Absorption Spectroscopy (Table 9)^{31; 49; 52; 53; 56; 140; 192}.

position and shape, which is consistent with the data and discussion presented earlier. The presence of minor second order quadrupolar shift effects would cause a systematic error in the calculated Ca-O bond distances. Since the sign of the second-order quadrupolar shift is always negative, the observed positions of our resonances are the most negative that the ⁴³Ca isotropic chemical shifts could be, and thus the interpreted mean Ca-O bond distance is the largest it could be. The effect of a second-order quadrupolar shift would move the calculated mean Ca-O bond distance towards the center of the range of values determined from XAS. Our maximum mean

bond distance is quite similar to that from the RMC model of Goodwin et al.²¹ (~2.47Å). The Gaussian shape of the observed ⁴³Ca resonances suggests that second-order quadrupolar effects may be negligible, and thus that our value of 2.45Å is close to the true mean Ca-O bond distance for our ACC samples. Other errors associated with the use of this correlation include uncertainty in the slope and intercept, although smaller values observed by XAS bond distance determinations are likely attributable to real differences between samples. In addition to replication of Gebauer's methods (in search of vaterite- and calcite- like ACC), the natural abundance NMR of naturally occurring ACCs should prove to be an interesting comparison to the results presented here (albeit with acquisition periods that are massively time consuming).

D. Magnesium (25) NMR

In an attempt to identify Mg domains in the ACCM and AMC ²⁵Mg NMR spectra that are similar to crystalline materials in the Mg-CO₃-H₂O system, theoretical spectra of reference phases in the Mg-CO₃-H₂O system (only those having well-known crystal structures) were calculated using the CASTEP NMR + SIMPSON approach under both static (Figure 17) and MAS (10,000 Hz; Figure 18) conditions with proton equilibration. The Mg-reference phases including sergeevite, barringtonite, pokrovskite, artinite, dypingite, and giorgiosite were excluded from these comparisons because these minerals lack adequately known crystal structures. As in the case of Ca-CASTEP NMR results, the isotropic shielding tensor was converted to a chemical shift scale by developing a correlation between the calculated absolute shielding and relative chemical shift scales using well-known compounds having large range of experimentally determined isotropic shifts, including periclase MgO, brucite MgOH, and magnesite MgCO₃ from the work of Pallister¹⁷¹ and dolomite MgCa(CO₃)₂ from the work of

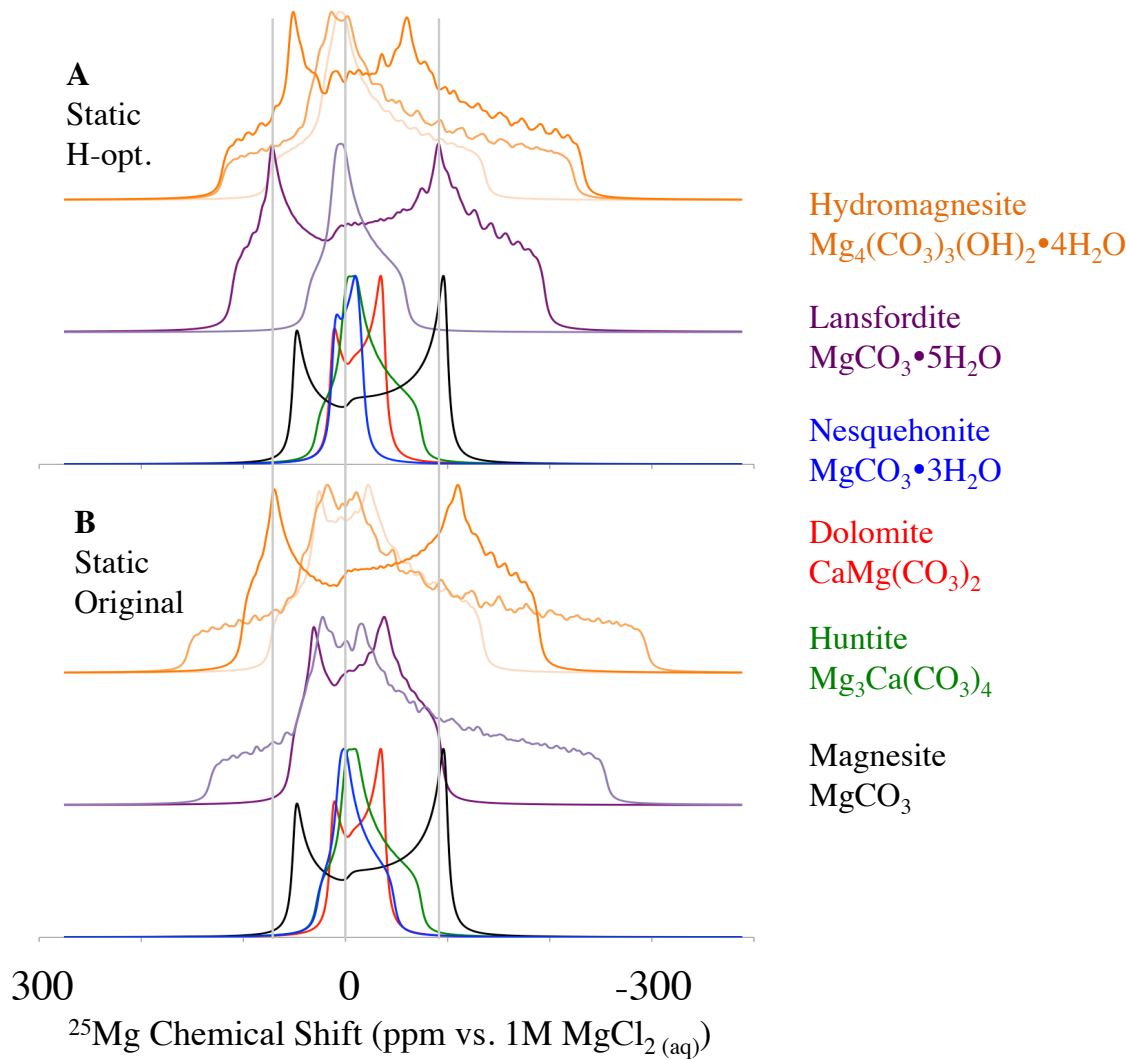


Figure 17. CASTEP-SIMPSON simulated reference phases in the Mg-CO₃-H₂O system, with and without proton equilibration under static conditions at 20T.

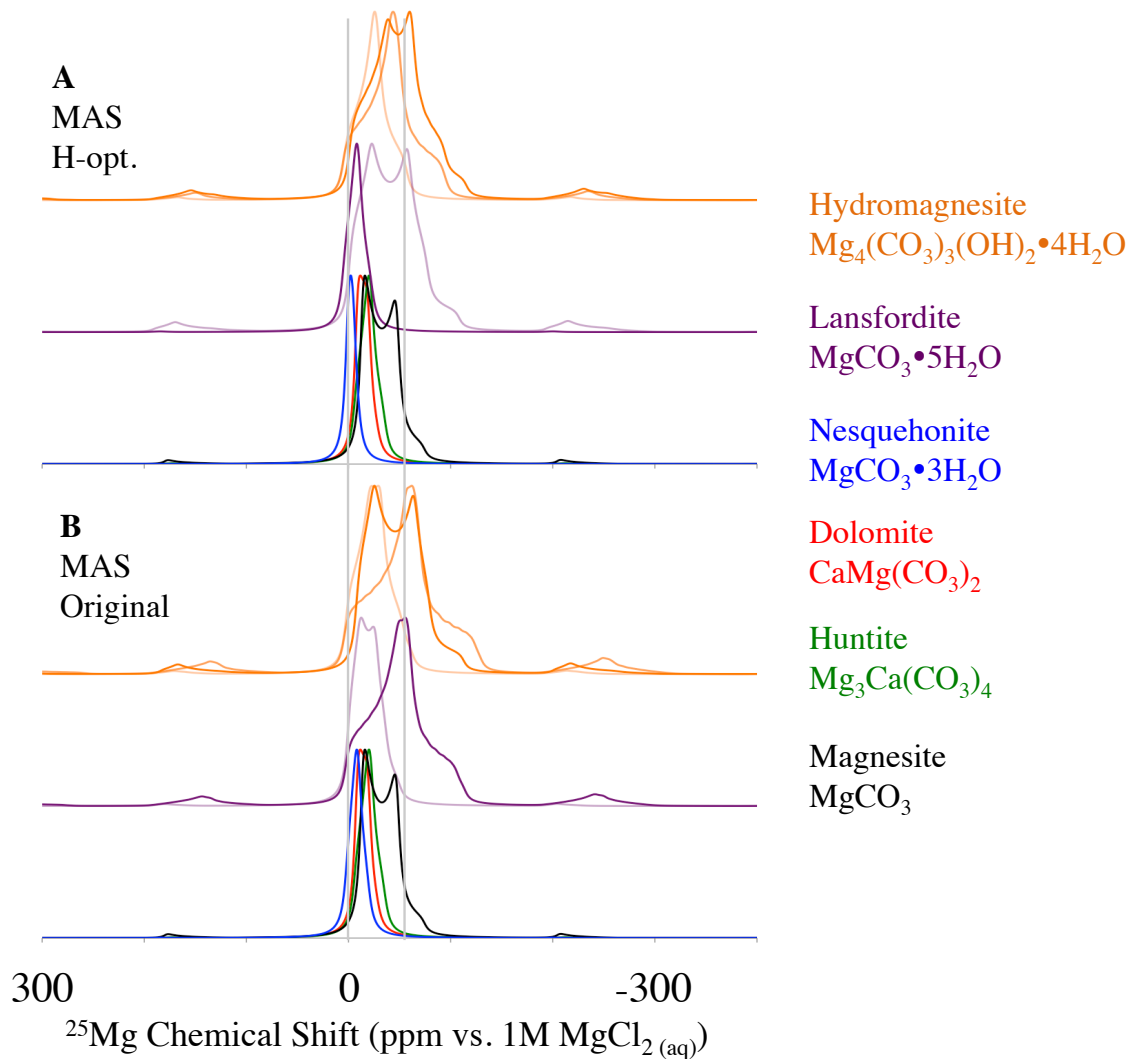


Figure 18. CASTEP-SIMPSON simulated reference phases in the Mg-CO₃-H₂O system, with and without proton equilibration under MAS (10 kHz) conditions at 20T.

MacKenzie^{170; 193} (Figure 11A). The correlation between calculated isotropic shielding tensor and experimental isotropic shift has a slope that is significantly different from unity although the correlation coefficient R^2 is very close to one [$y = -0.9099x + 511.59$ $R^2 = 0.99832$]. The deviation in the slope from the ideal value of one has been attributed to systematic error in the pseudopotential construction by others who have developed similar correlations^{174; 176; 186}. However, since the systematic error is applied in a consistent fashion to all phases and is further regressed with experimental data, the effect is essentially insignificant in light of the high correlation coefficient. As mentioned above related to CASTEP NMR results, Pallister et. al has published a similar correlation including a huge diversity of Mg compounds, and the slope and intercept do differs slightly from our more limited study (comparison of correlation presented in Table 6).

The spectra generated from the computational results of CASTEP NMR+SIMPSON (Figures 17A and 18A) suggest that geometric effects make a large contribution to the ²⁵Mg NMR properties and so no simple correlation with Mg-O bond distance (or any other single variable) is possible. In figures 17 and 18, the simulated spectra are organized into categories based on spectral similarities to aide in interpreting the APMC and AMC experimental resonances. Several types of local Mg²⁺ environments exist in the Mg-CO₃-H₂O system including highly symmetric phases (magnesite, dolomite, and nesquehonite) and highly asymmetric phases (huntite, lansfordite, and hydromagnesite). Isotropic chemical shifts (center of mass for each resonance) in the Mg-CO₃-H₂O system are clustered within 10 ppm for all phases and are consistent with a relatively small range of mean Mg-O bond distances known from X-ray diffraction studies (2.04-2.12Å; see also Table 6). Unlike in Ca-NMR (which was interpreted primarily in terms of isotropic shift distributions), the dominant spectral features of

^{25}Mg -NMR are governed by the quadrupolar interactions that arise from the large nuclear quadrupole moment of ^{25}Mg (199.4 Q/mBarn; 2 orders of magnitude larger than that of ^{43}Ca), which is strongly coupled to the electric field gradient near the magnesium nucleus of non-spherically symmetric coordination environments. Thus, for highly symmetric Mg coordination environments the ellipsoid will be nearly spherical and the asymmetry parameter zero, such that the overall breadth of the resonance and breath of the horns will be similar, as typified by the sharp edges of magnesite, dolomite, and nesquehonite spectra (Figure 17A). Of these more symmetric phases we see that short Mg-O bond distances induce smaller quadrupole couplings (Nesquehonite (2.076\AA ¹⁹⁴) < Dolomite (2.081\AA ³⁹) < Magnesite (2.105\AA ¹⁹⁵). For asymmetric coordination environments the electric field gradient ellipsoid along the minor axes is asymmetric and approaches a value of one, and hence the central singularities of the powder pattern merge toward the middle of a quadrupolar powder pattern, as is observed for Mg-local environments in huntite, lansfordite, and hydromagnesite. The Mg-O bond distance relationship with quadrupolar coupling again holds roughly true for asymmetric phases (hydromagnesite (2.10 ¹⁷⁸) > lansfordite (2.0894) > hydromagnesite (2.04 ¹⁷⁸) > lansfordite (2.0885) > huntite ($2.1+2.1+2.03=2.076$ ¹⁵⁶). If one attempts to correlate bond distance with quadrupole couplings across these phases, one finds that the intensity of the quadrupolar coupling is also sensitive to the geometry and polarization of the Mg environment, making simple correlations with the Mg-O bond distance with high statistical confidence impossible. Notably upon H-only equilibration using the CASTEP DFT code, nesquehonite becomes more symmetric, while sites of hydromagnesite and lansfordite become more asymmetric. Since the original X-ray structure determinations do not all apply proton positions in an identical manner, there is no systematic explanation for the structural evolutions under proton-only equilibration. H-only equilibrations

will be used for all subsequent comparisons to experimental data. The MAS spectra (Figure 17B and 18B) are shown for comparison with static spectra. The simulated MAS spectra of crystalline reference phases show a narrower resonance that results from MAS conditions and the presence of weak spinning sidebands that result from the satellite transitions. The H-opt MAS simulations will be subsequently used for comparison to experimental MAS NMR spectra at 10kHz.

While ^{43}Ca -NMR of X-ray amorphous materials shows Gaussian line shapes, ^{25}Mg -NMR of AMC and APMC gives rise to superposition of many quadrupolar line shapes (Figure 19 and 20). If the local Mg-environments exist in an ideally disordered continuum (as interpreted for Ca-sites of ACC and APMC) the superposition of infinitely many local environments would smear the quadrupolar singularities and the net result would be Gaussian or an asymmetric Gaussian. Instead, the existence of singularities indicates a constructive statistical preference for certain local configurations. It is also worth mentioning that between various samples having different compositions, the positions of many certain singularities can be traced vertically from sample to sample and in phases that are both crystalline and non-crystalline (Figure 21). This observation suggests that a theory of polyamorphisms framed according to crystalline polymorphs may be more appropriate for AMC materials than was observed for ACC materials. As for our previous analysis of ^{43}Ca -NMR, the combined CASTEP NMR+SIMPSON simulation of Mg-bearing crystalline phases provides a positional reference for ^{25}Mg -NMR under static (Figure 19) and MAS (Figure 20) conditions. Many of the experimentally observed features are not directly comparable to any known equilibrium crystal phase. The large number of singularities in the experimental ^{25}Mg -NMR spectra precludes any quantitative deconvolution.

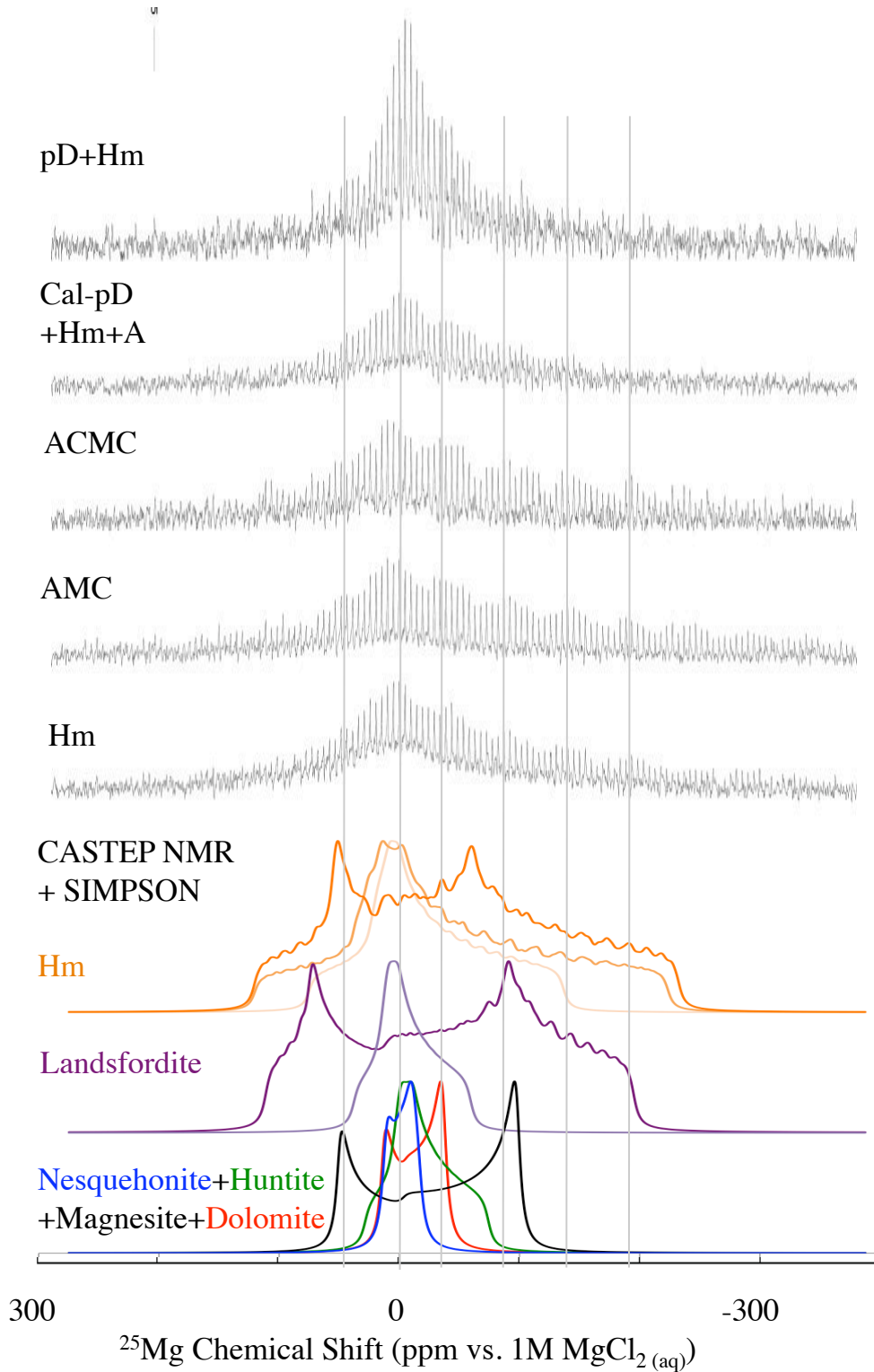


Figure 19. Static ^{25}Mg NMR spectra of synthetic phases in the $\text{Mg-CO}_3\text{-H}_2\text{O}$ system compared to proton-only equilibrated CASTEP NMR reference spectra.

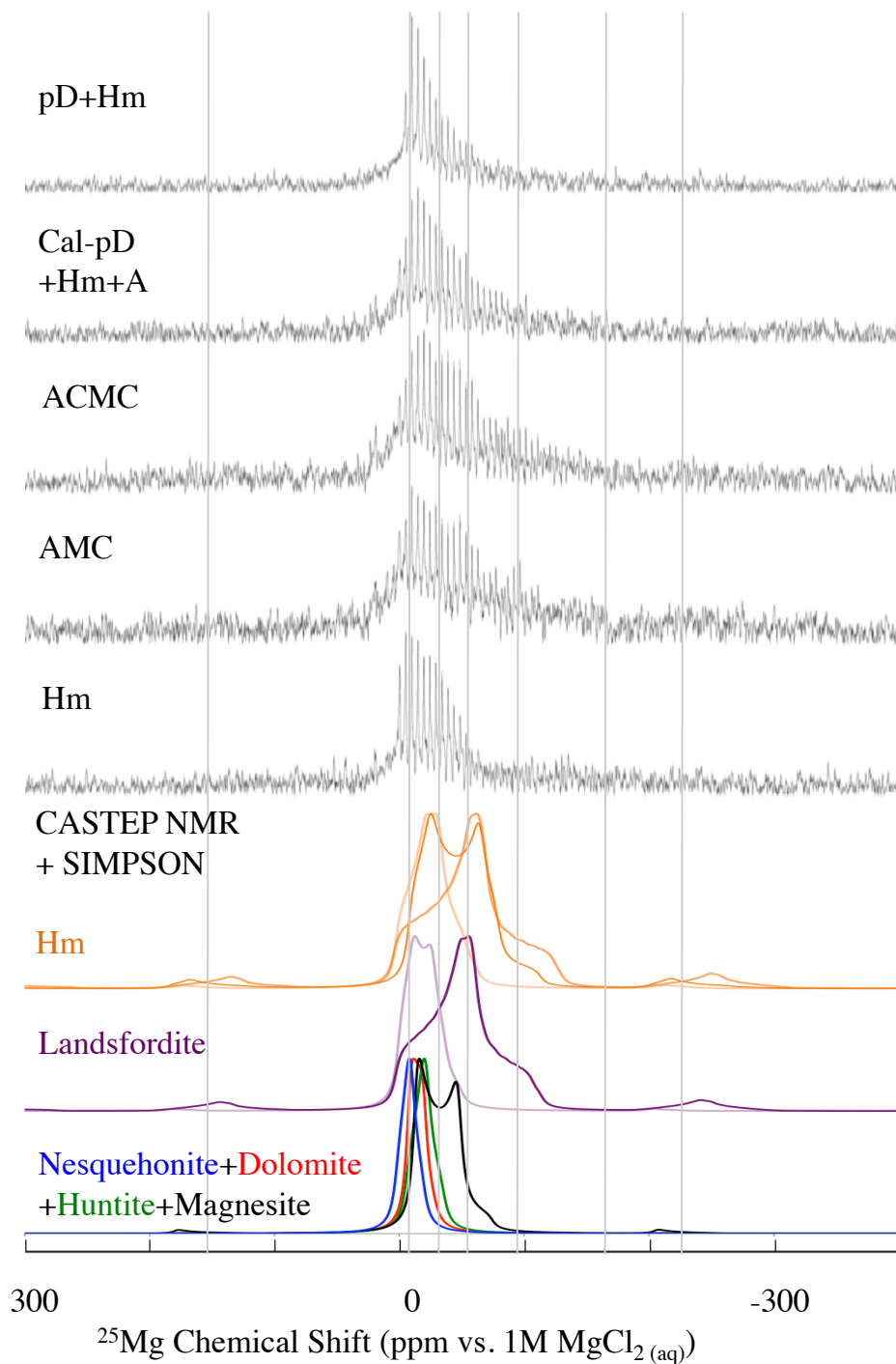


Figure 20. MAS (10 kHz) ^{25}Mg NMR spectra of synthetic phases in the $\text{Mg-CO}_3\text{-H}_2\text{O}$ system compared to proton equilibrated CASTEP NMR reference spectra.

Quantitative deconvolution in terms of reference phases would not be appropriate since many of the phases in the Mg-CO₃-H₂O system do not yet have adequately known structures and therefore the reference set is essentially incomplete. From the experimental ²⁵Mg-NMR spectra presently at hand, it is impossible to uniquely distinguish NMR properties like quadrupolar coupling, asymmetry, chemical shift anisotropy and asymmetry, isotropic shifts since the convolution of features is so severe. The structural variables like bond distance and coordination number also cannot yet be quantitatively assigned to each feature present in the experimental spectra. It is notable that we observe significant signal intensity that extends to low resonance frequencies (negative chemical shifts) far beyond the known equilibrium phases in the Mg-CO₃-H₂O system (of those phase for which crystal structures are well known). From our previous categorization of site geometry and the properties of well-known reference phases, these sites would have very large bond distances (>2.12Å) and have large quadrupolar couplings, high coordination numbers, or there is a small probability that we are observing intensity from the satellite transitions. The latter possibility of satellite transitions is weakly plausible since MAS spinning side bands (that arise from satellite transitions) are not observed in the corresponding MAS spectra (Figure 20). The possibility of high coordination numbers is consistent with Mg-EXAFS studies of Mg-stabilized ACC that reported a coordination number of 8.2³⁴. It remains to be seen if the other reference phases in the Mg-CO₃-H₂O system (sergeevite, barringtonite, pokrovskite, artinite, dypingite, and giorgiosite) account for some of these low frequency features in our ²⁵Mg NMR spectra. It is interesting that this sample of hydromagnesite shows a crystalline diffraction pattern (Figure 21) but appears most similar to the disordered ACMC and AMC compounds with respect to its ²⁵Mg NMR local structure (compare NMR of Hm in Figure 19 and 20 with XRD in Figure 21). The sample of crystalline hydromagnesite is finely

powdered and therefore may not represent ideally ordered or phase pure hydromagnesite. We do not propose any particular explanation for the appearance of hydromagnesite's ^{25}Mg NMR resonance. However as discussed above in the CASTEP results, the earlier experimental observations of MacKenzie and Meinhold at lower magnetic fields are inconsistent with CASTEP calculations of the ideal hydromagnesite and inconsistent with our own experimental observation. It seems that there is may be multiple structural variants of hydromagnesite that may be related in their long-range average, but differ with respect to local and intermediate scale arrangements.

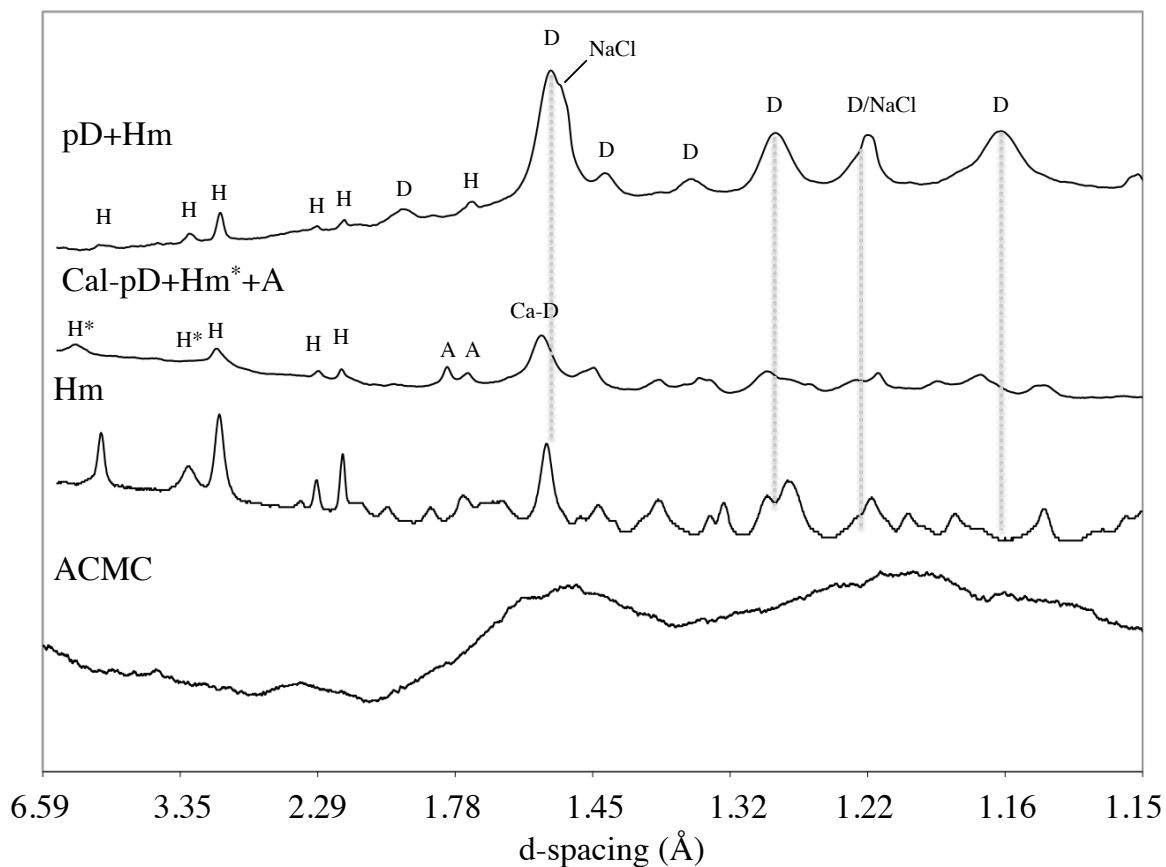


Figure 21. Logarithm of XRD Intensities for samples relevant to Mg-NMR spectra. Vertical lines trace the salient features attributable to dolomite (D) to highlight differences between protodolomite (pD), calcian protodolomite (cal-pD) and hydromagnesite (Hm).

structure, while differing on the local arrangements. A multi-scale crystallography using local NMR tensor data, and long-range diffraction techniques (x-ray and neutron) should be combined for future studies of the Mg-CO₃-H₂O system to sort out these discrepancies.

A detailed integration molecular modeling will be an invaluable addition to the interpretation of these data, however MD simulation that was possible for ACC is not yet possible for AMC and mixed phase APMC, and thus interpretation of the Mg-NMR remains somewhat more limited than in the previous case of Ca-NMR. There has been no RMC-total scattering study for APMC and AMC analogous to the study of Goodwin et al. on ACC. Alternatively we have considered model generation from a purely modeling perspective; unfortunately the water exchange dynamics of Mg hydration are so slow there is no practical means to equilibrate model structures that contain magnesium and water on MD timescales. Monte Carlo methods would be a time-independent technique for equilibrating an amorphous Ca-Mg-CO₃-H₂O structural model, however the Monte Carlo codes available were not amenable to dense, amorphous phases and therefore had very low acceptance rates for reinsertion moves. Thus, any artificial or arbitrary starting point for the model would be effectively mired in an unrealistic local minimum. Future studies and developments to overcome these limitations will be discussed below in section F.

E. Dolomite Crystallization

We have observed a hydrated, stoichiometric, protodolomite (pD)-hydromagnesite (Hm) assemblage that crystallizes at 50°C and 100% relative humidity from the APMC having an initial chemical composition of Ca_{0.4}Mg_{0.6} CO₃ • 2H₂O (Figure 22). After crystallization and

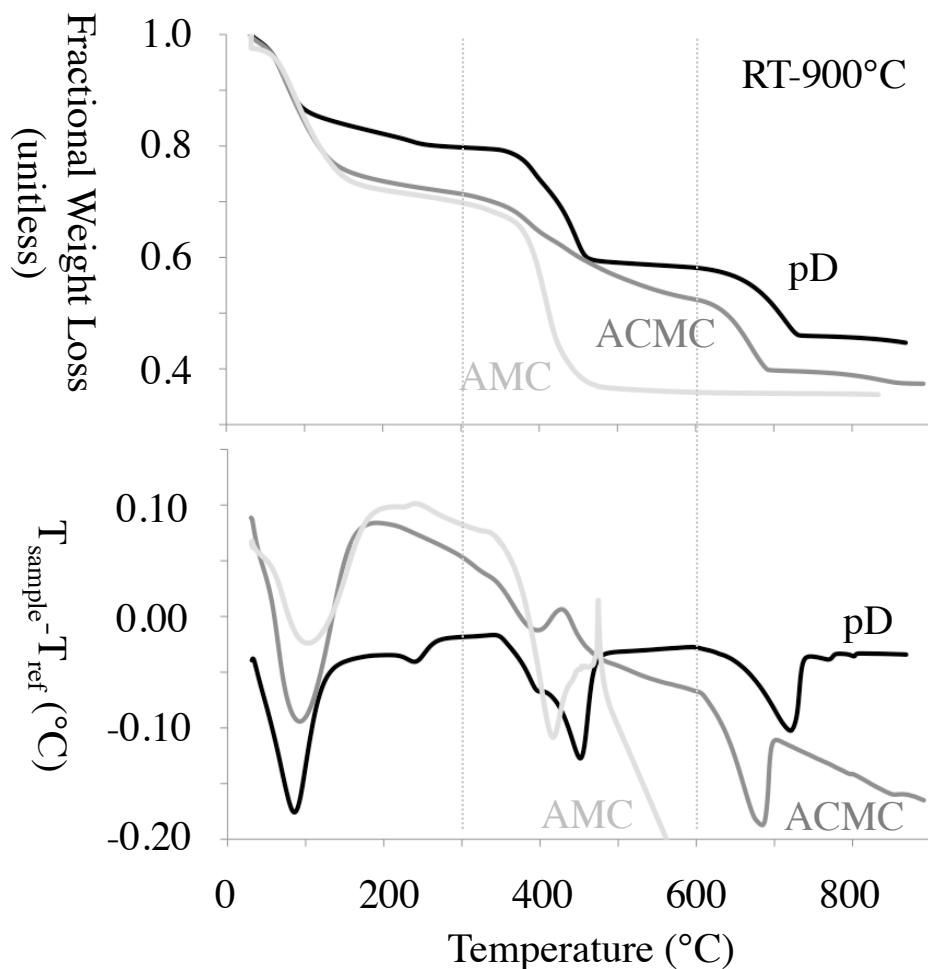


Figure 22. TGA and DTA from RT to 900°C for AMC, ACMC, and protodolomite (pD). DTA can not be quantitatively converted to the energy of the transition because of unknown sample densities and heterogeneous sample contact with the platinum electrode during shrinkage and cracking.

drying, the crystallized protodolomite+hydromagnesite still shows ~1 formula unit of chemically bound water that dehydrates steadily up to 250°C (Figure 22). The AMC and ACMC samples that were not subjected to conditions of recrystallization have the greater labile water content than the crystallized assemblage, which is generally consistent with the prevailing view that ACC crystallization is related to dehydration of the chemically incorporated waters.

Hydromagnesite also loses some of its chemical water below 250°C, however we shall argue that hydromagnesite is a minor component of this assemblage and that much of this chemically bound water must be associated with a protodolomite phase. Although the XRD might qualitatively suggest that protodolomite is a major component of the assemblage relative to a minor phase of hydromagnesite (Figure 21), it is noted from electron microscopy (Figure 23) that these phases have crystallite sizes that are near to the limits of size-dependent intensity effects in XRD (<100 nm). Therefore, the integrated XRD intensities may not quantitatively reflect the relative phase abundances between protodolomite and hydromagnesite. Additional evidence from ¹³C NMR also confirms that hydromagnesite is a very minor component of this sample assemblage (Figure 12, pD+Hm*). The hydromagnesite (Hm*) is hardly detected by ¹³C NMR. Therefore we might estimate that the sample is >80% protodolomite. Thus for subsequent discussions we will attribute the ~1 formula unit of water to the stoichiometric protodolomite phase.

Thermal decarbonation occurs in the protodolomite sample in two major steps that occur around 400°C and 700°C. The thermal decomposition behavior of hydromagnesite has been studied previously and is known to decarbonate from (350-500°C) in a single step¹⁹⁰. If a minor component of hydromagnesite is present (as suggested by XRD and ¹³C), then the decarbonation at 400°C can be partially accounted for by hydromagnesite, but a substantial portion of the decarbonation at 400°C must be accounted for by the protodolomite phase. Indeed this interval of weight loss appears to have contributions from two components--which for an initial guess may be attributed to a small difference between hydromagnesite and protodolomite decarbonation. Since anhydrous dolomite shows only decarbonation in a single event around 700-800°C, the hydration of protodolomite must be responsible for the significant decarbonation

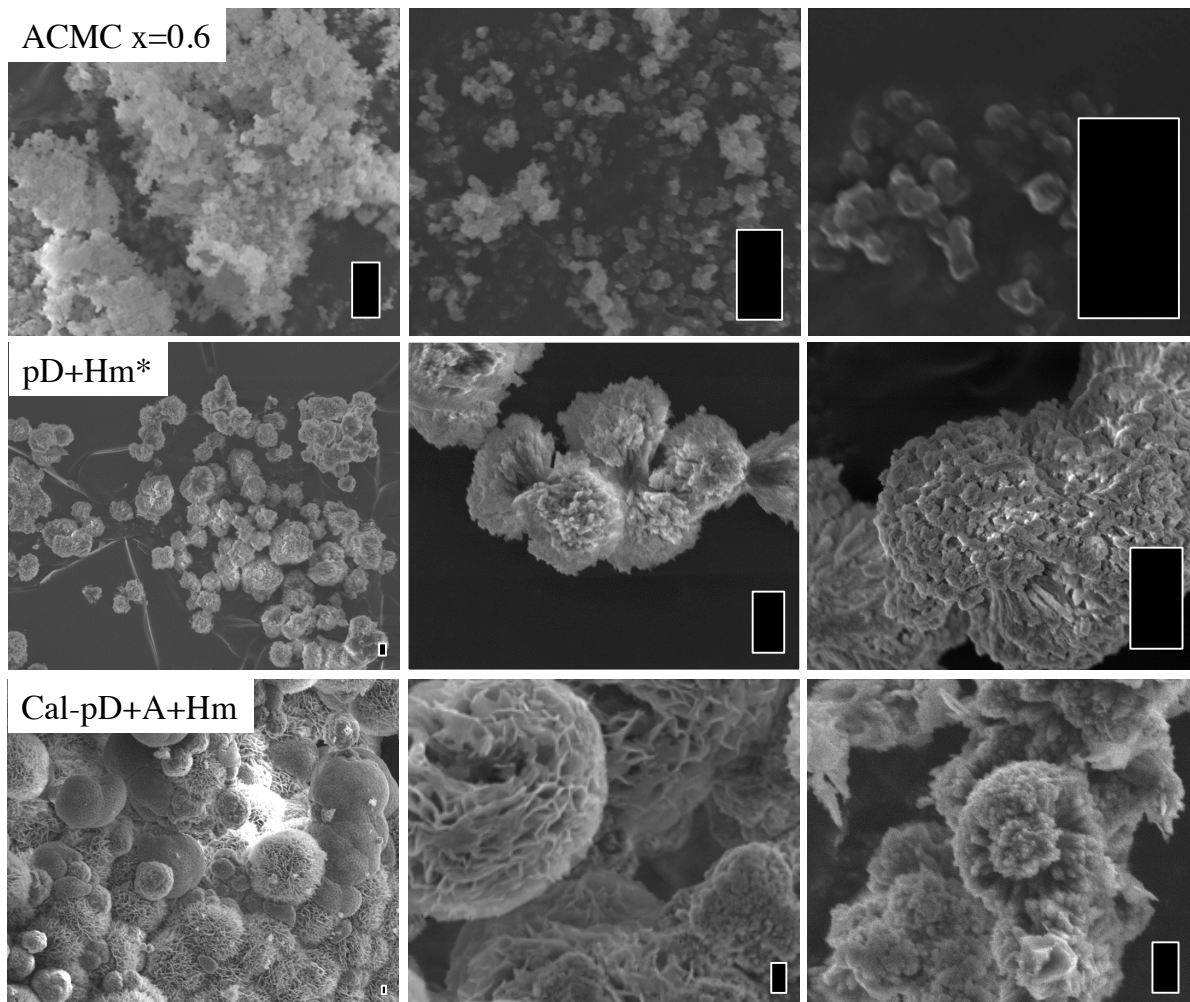


Figure 23. SEM of the ACMC precursor, protodolomite (pD+Hm), and calcian-pD and company. Scale represents 1 micrometer in all images. The amorphous particles of ACMC ($x=0.6$) are aggregates that are $<100\text{nm}$ in diameter. Proto-dolomite (pD) has dumbbell shaped floret structures with rods on the order of 100 nm thickness however the structural relationship between pD and hydromagnesite is not evident in these images. The multiphase nature of the calcian protodolomite (cal-pD) is clearly evident and differs greatly from that of protodolomite, including aragonite (A) and hydromagnesite (Hm).

characteristic of pure-Mg carbonate compounds. Overall, the decarbonation behavior of the protodolomite is similar to the decarbonation of the uncrystallized ACMC sample and that some kind of Ca-Mg phase separation may occur upon dehydration of the chemical water, like a distillation of ions with higher hydration energy (Mg). High temperature structural studies

during the decomposition of this phase should provide additional insight into the structural evolutions on heating.

^{13}C -NMR spectrum of crystalline protodolomite-hydromagnesite is significantly narrowed and relaxed to a less ionic environment than the ACCM sample (Figure 12). The carbon spectrum of the protodolomite is very similar to that reported in the literature for anhydrous dolomite by Papenguth et al ¹⁶⁹ appearing to have little influence of carbonate-water hydrogen bonding as was inferred from the more negative frequency of samples with higher degrees of hydration. The carbon NMR spectrum of protodolomite also includes a small signal at low frequencies (noted as Hm*) that overlaps with the less intense resonance of hydromagnesite. It can be seen by comparison to a pure hydromagnesite (Hm), and to hydromagnesite in assemblage with calcian protodolomite (Cal-dD+Hm), that the hydromagnesite in assemblage with stoichiometric protodolomite (pD+Hm*) is a very minor component of the assemblage from the perspective of ^{13}C NMR. There is a notably broad base around the sharpened ^{13}C resonance of protodolomite and it remains unclear if this reflects the structural disorder within the protodolomite phase or should be considered as an anhydrous amorphous phase that is somehow related to the unusual appearance of the Hm* resonance. The calcian protodolomite (cal-pD) ^{13}C resonance shows a much broader resonance than does pD and coexists with resonances attributable to typical hydromagnesite and aragonite. This three-phase assemblage shows that the two-phase unmixing model of Radha ¹⁰² insufficiently explains the complexity of ACC recrystallization (finding coexistence of $x=0$, $x=0.5$, and $x=0.1$ materials). This assemblage is consistent with expectations of equilibrium thermodynamics that predicts immiscibility gaps between $x=0.0-0.5$ and $x=0.5-1.0$. The calcian protodolomite ^{13}C NMR resonance is broader than that of the stoichiometric protodolomite and shifted toward lower

resonance frequency possibly indicating that the calcian protodolomite hydration hydrogen bonds with carbonate. XRD demonstrates that there is less Mg in the calcian-pD phase¹⁵¹ and therefore the some of these waters may be partially interacting more weakly with Ca ions. ¹H-¹³C CP of calcian protodolomite confirms the presence of water-carbonate hydrogen bonding (because there is a strong H-C CP signal). In contrast the strong CP signals of calcian protodolomite and APMC phases, the CP of stoichiometric protodolomite produces no signal indicating the Mg is tightly hydrated and does not participate in any water-carbonate hydrogen.

Magnesium NMR of the protodolomite indicates a significantly narrower distribution of Mg environments in the crystallized protodolomite with respect to all other phases observed including the calcian protodolomite, the uncrystallized APMC, AMC, and a crystalline hydromagnesite (figure 19 and 20). The ²⁵Mg-NMR of protodolomite exhibits a highly asymmetric quadrupolar character that is most similar to that predicted for the asymmetric site of lansfordite $[\text{Mg}(\text{CO}_3)_2(\text{H}_2\text{O})_4]^{2-}$ or the local Mg^{2+} environment in huntite, rather than the quadrupolar parameters predicted for ideal dolomite (Figure 19). The asymmetric site of lansfordite is the most suitable candidate for hydrated Mg in protodolomite (Figure 24).

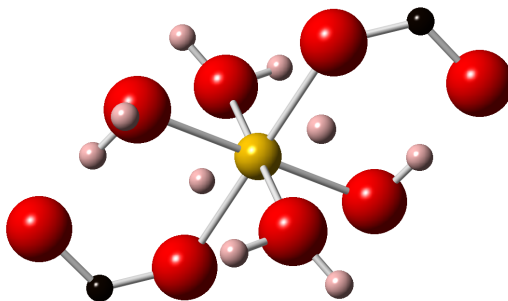


Figure 24. The asymmetric site in lansfordite may provide an analogy to protodolomite.

Although sufficiently asymmetric, the Mg-site of huntite does have the proper symmetry for direct analogy to the local Mg^{2+} environments in dolomite (isostuctural with calcite and magnesite). Given the degree of protodolomite hydration (1 formula unit of H_2O per metal ion), there could be up to two formula units of H_2O per Mg ion. A partially hydrated Mg ion within a dolomite like site would have an expanded effective radius (much larger than non-hydrated Ca) and this effect may facilitate a driving force required to ultimately achieve dolomite-like ordering. It is known for mixed metal compounds that if the difference in radii is small then they will tend toward solid solution. If the difference in radii is great then an ordered compound will form with segregation of the mixed metal species to unique sites. In the case of ordered dolomite, it has been argued that the difference between the atomic radii of Mg (160 pm) and Ca (197pm) is sufficient to favor an ordered phase but kinetically inhibited^{155; 164} thereby explaining the extreme difficulty of ordered dolomite synthesis. The hydrated radius of magnesium can be up to 400 times larger¹⁹⁶ and would provide an exceptional driving force for ordering of protodolomite. The ^{25}Mg NMR of calcian pD is wider as compared to that of stoichiometric dolomite (pD) and interestingly the sample of hydromagnesite that appears to be very crystalline by XRD (Figure 21) shows a relatively disordered ^{25}Mg NMR spectrum. The X-ray refinement of Althoff³⁹ compares Mg-O bond distances in stoichiometric dolomite, magnesian calcites, and calcian protodolomites. Mg-O in stoichiometric, ordered dolomite adopts an ideally compact octahedral structure (Mg-O=2.078 Å) having a minimum bond distance, while in contrast Mg-substitution in calcite distorts the octahedra, reduces cation shielding, weakens Mg-O bonding, and increases thermal motions of the cations. The mean metal-O bond distances found by Althoff (2.33 Å) in magnesian calcite ($x=\text{Mg}/(\text{Mg}+\text{Ca})=0.1$) were near to those expected for pure Ca-calcite (2.36 Å) and decreased in a fashion linearly proportional to the amount of Mg present

in the structure. Thus if one extrapolates this trend to disordered, stoichiometric dolomite ($x=0.5$) one would predict a mean Mg-O distance of 2.21 Å which is much greater than that for the ordered dolomite (2.078 Å). The findings of Althoff are consistent with the thermodynamic energies of these phases as seen by Navrotsky and others (Figure 5). Although dolomite ordering is not observed by the existence of substructural reflections in the XRD of protodolomite (Figure 21) the narrow ^{13}C - (Figure 12) and ^{25}Mg - (Figure 19) NMR line shapes may indicate reduced thermal motions in our stoichiometric protodolomite and some degree of nano-scale ordering that does not produce ordered diffraction. The temporal dynamics of this motion is not known and this kind of distortion and [possibly slow] dynamics may be responsible for the broadened structures observed for calcian protodolomite and hydromagnesite. There is a great need for chemical simulations of the ACCM phases to understand and further comment on the role of H_2O within the protodolomite structure. In the future Cryo-TEM of these phases could provide a visual insight to the states of order and disorder near the molecular scale and bridge the scale gap between XRD and NMR.

F. Next Steps and Future Work

There is much more synthetic and characterization work to bridge this study with the synthetic efforts of Gebauer et al.^{23;55}, the intermediate range models of Goodwin et al.²¹, and to understand the natural occurrences of amorphous carbonates (Table 9). The occurrences of prestructured polyamorphisms is said to occur under slight degrees of supersaturation (under a quasi-equilibrium condition) that is only possible through robotic control of reagents and buffers. Repeating the methods of Gebauer with isotope enrichment sufficient for NMR would provide a decisive distinction between the prestructured and unstructured amorphous regimes.

We have made some attempt here using small angle x-ray scattering SAXS to determine the intermediate-range inhomogeneities of our ACMC samples from ~ 5 to 100 nm which partially bridges the scale gap between SEM of Figure 23 (down to 100 nm) and the local structures of NMR. Indeed all of the amorphous samples did produce significant small angle scattering that was unlike crystalline materials, and these samples did also show some differences in the overall intensity of small angle scattering and the scale of inhomogeneity (Figure 25 and 26). ACC showed the greatest scattered intensity down to $\sim 0.4^\circ$ (2θ), being overtaken by the scattered intensity of ACMC and pD. This indicates that Mg-rich phases possess a larger scale of heterogeneity than in ACC and we might infer that PNCs in Mg-rich parent solutions grow to larger sizes. The crystallized protodolomite shows greater scattered intensity at all angles as compared to its ACMC precursor but no distinct difference in line shape. This indicates the scale of heterogeneity remains the same but the sharpness of the boundaries are increased during the crystallization to protodolomite. Thus the crystallization is likely to nucleate within the original PNC rather than at PNC-PNC interfaces. The distinctions between samples at small angles (0.2° , 2θ , equivalent to 100 nm) becomes convoluted with scattering of the incident beam. A more reliable comparison of these samples should be done using a high intensity synchrotron source that can improve the signal intensity and effectively reduced the beam scattering to ultra-small angles (USAXS) and thereby create a region of overlap with the scale of SEM images of Figure 23.

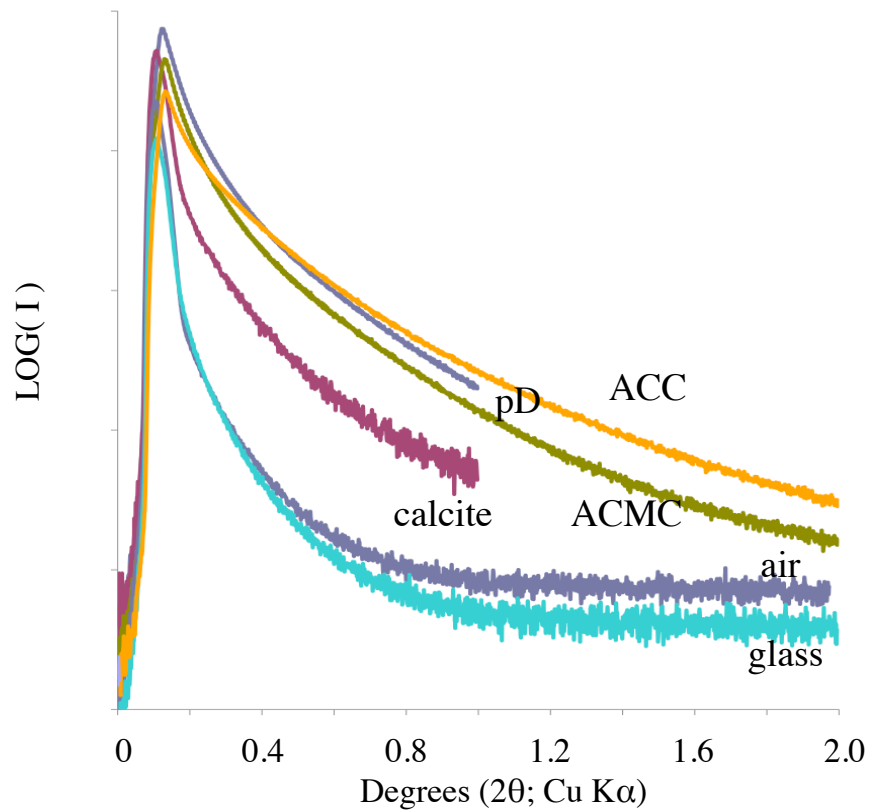


Figure 25. SAXS raw data for several samples ACC ($x \sim 0$), ACMC ($x \sim 0.6$), and protodolomite (pD, $x \sim 0.6$) as compared to crystalline calcite and glass and air backgrounds. Backgrounds are not explicitly subtracted from the sample data. The small angle scattering becomes convoluted with scattering from the primary beam around 0.2 degrees.

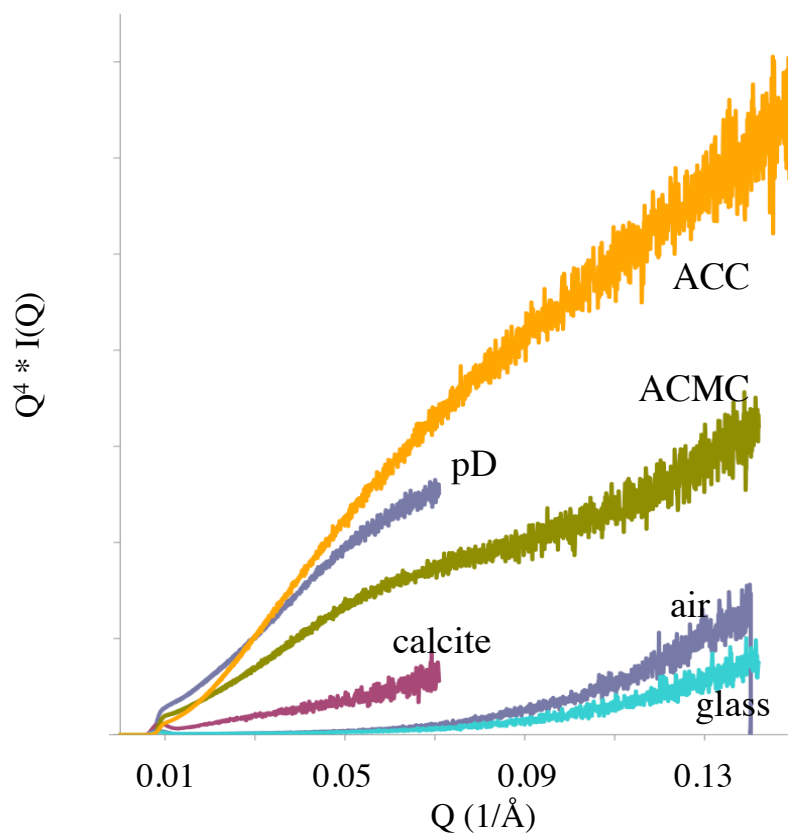


Figure 26. Porod plot of SAXS data ACC ($x \sim 0$), ACMC ($x \sim 0.6$), and protodolomite (pD, $x \sim 0.6$) as compared to crystalline calcite and glass and air backgrounds. Backgrounds are not explicitly subtracted from the sample data.

Time resolved spectroscopies have not yet been applied toward the study of carbonate materials however in the near future the availability of ultra-fast (femto-second) IR laser pulses and time-resolved infra-red spectroscopy will be able to distinguish the vibrational perturbation-relaxation dynamics of various polymorphs and ACC without many of the technical restrictions that limit NMR. This emerging technique will also give local structural information (on the scale of chemical bonds) with higher time resolution and lower cost than NMR. This technique should

prove highly useful to determine the evolution of ACC aging and transformation on timescales of seconds to minutes.

There is much work to be done in the field of carbonate crystallization. For the Ca-CO₃-H₂O system there remains outstanding questions regarding vaterite and monohydrocalcite structures—especially regarding the order-disorder transitions. The disordered forms of these phases are relatively long lived, but in actuality the time resolved details of disorder-order transitions for *all* of the crystalline polymorphs is a natural extension of this work that requires further study by both experimental and computational approaches. We have observed only a few ex-situ glimpses into the molecular scale nature of these transformations and there remains much to be discovered. Within the Mg-CO₃-H₂O system there are many phases that are poorly understood and much greater volume of work than compared to the calcium system. A comprehensive understanding of these phases must be first based upon synthetic control, and then move forward with XRD and neutron diffraction Rietveld refinements, in addition to tensor-based NMR studies that provide experimental determinations of the local site symmetry¹⁸⁰. The details of nucleation and crystallization of these phases must be approached with a multiscale perspective.

Computational simulation of amorphous phases and transformations are challenged with respect to both time and spatial scales. The brute force computational approach requires both large system sizes (currently possible) over time-scales that are currently inaccessible to molecular dynamics much less so to ab initio molecular dynamics (AIMD). Development of time-independent techniques like Monte-Carlo equilibration, simulated annealing, and directed meta-dynamics will undoubtedly improve the exploration of phase space, give new insights to the fundamental mechanisms, and may be used to test the mechanisms put forth here that are too

fast to observe experimentally (nanosecond to seconds). Molecular dynamics is also limited with respect to accuracy. Many of the currently available water models are not sufficiently sophisticated to capture the diversity of behaviors in liquid, confined, and solid states. Molecular dynamics is also not well suited for flexible ion parameters that are capable of simulating a diversity of aqueous matrix ions in solution, at interfaces, and in their corresponding crystalline phases.

CONCLUSION

The formation and transformation of calcium-magnesium amorphous carbonates occurs by nonclassical aggregation and leads to a diversity of disordered environments. The relatively long bond distances of Ca-O bonding (2.3-2.5 Å) and weak affinity for water (relative to Mg) leads to continuous distribution of disorder that is inconsistent with a theory of polyamorphisms. We find a maximum mean bond distance (2.45 Å) that suggests a locally expanded environment around Ca. Structural differences between various ACC are more likely to occur according to the length scales of aggregation and CO₃-H₂O hydrogen bonding rather than Ca local environments. The short bond distances typical of Mg-O (2.04-2.12 Å) and its relatively high affinity for water leads to a more polarized ¹³C environment than in hydrated ACC. ²⁵Mg-NMR also indicates that APMC and AMC have discrete preference for local site geometries. However the types of local sites do not exactly correspond to any known reference phases and extend toward low frequency far beyond the equilibrium environments. By comparison to the properties of reference phases, the low frequencies and skew toward low frequencies can be interpreted as high mean coordination number >6 (up to 8 as determined by XAS studies of others) and potentially mean bond distances >2.12 Å. Due to the number of superimposed ²⁵Mg resonance features and uncertainties regarding the actual structures of reference phases, no quantitative deconvolution is possible with respect to reference phase analogs. The differential affinity for water (Mg>Ca) in addition to CO₃ H₂O hydrogen bonding leads to a variety of competitive factors that shape the energetic landscape of ACC-APMC-AMC formation and crystallization.

REFERENCES

- ¹A. Becker, "Structural Characterisation of Biominerals and Biomimetic Crystallisation of Calcium Carbonate." in Institut für Anorganische Chemie der Universität Duisburg-Essen, **Doctoral Dissertation** Universität Duisburg-Essen, 2005.
- ²C.-L. Chen, J. Qi, R. N. Zuckermann, and J. J. DeYoreo, "Engineered Biomimetic Polymers as Tunable Agents for Controlling CaCO₃ Mineralization," *Journal of the American Chemical Society*, **133**[14] 5214-17 (2011).
- ³L. B. Gower, "Biomimetic Model Systems for Investigating the Amorphous Precursor Pathway and Its Role in Biomineralization," *Chemical Reviews*, **108**[11] 4551-627 (2008).
- ⁴W. Li and C. Gao, "Efficiently Stabilized Spherical Vaterite CaCO₃ Crystals by Carbon Nanotubes in Biomimetic Mineralization," *Langmuir*, **23**[8] 4575-82 (2007).
- ⁵B. J. McKenna, J. H. Waite, and G. D. Stucky, "Biomimetic Control of Calcite Morphology with Homopolyanions," *Crystal Growth & Design*, **9**[10] 4335-43 (2009).
- ⁶I. Sondi, S. D. Skapin, and B. Salopek-Sondi, "Biomimetic Precipitation of Nanostructured Colloidal Calcite Particles by Enzyme-Catalyzed Reaction in the Presence of Magnesium Ions," *Crystal Growth & Design*, **8**[2] 435-41 (2007).
- ⁷K. Calderia, "Ocean Acidification: Adaptive Challenge or Extinction Threat?," in American Geophysical Union, **Fall Meeting, December 2012.**, San Francisco, CA, 2012.
- ⁸J. A. Kleypas, R. A. Feely, V. Farby, C. Langdon, C. L. Sabine, and L. L. Robbins, "Impacts of Ocean Acidification on Coral Reefs and Other Ocean Calcifiers." in A Report of a Workshop Sponsored by NSF NOAA USGS. 2006.
- ⁹S. Krief, E. J. Hendy, M. Fine, R. Yam, A. Meibom, G. L. Foster, and A. Shemesh, "Physiological and isotopic responses of scleractinian corals to ocean acidification," *Geochimica et Cosmochimica Acta*, **74**[17] 4988-5001 (2010).
- ¹⁰J. C. Orr, V. J. Fabry, O. Aumont, L. Bopp, S. C. Doney, R. A. Feely, A. Gnanadesikan, N. Gruber, A. Ishida, F. Joos, R. M. Key, K. Lindsay, E. Maier-Reimer, R. Matear, P. Monfray, A. Mouchet, R. G. Najjar, G.-K. Plattner, K. B. Rodgers, C. L. Sabine, J. L. Sarmiento, R. Schlitzer, R. D. Slater, I. J. Totterdell, M.-F. Weirig, Y. Yamanaka, and A. Yool, "Anthropogenic ocean acidification over the twenty-first century and its impact on calcifying organisms," *Nature*, **437**[7059] 681-86 (2005).
- ¹¹S. Rahmstorf and A. Ganopolski, "Long-Term Global Warming Scenarios Computed with an Efficient Coupled Climate Model," *Climatic Change*, **43**[2] 353-67 (1999).

- ¹²W. S. Broecker, "The great ocean conveyor," *AIP Conference Proceedings*, **247**[1] 129-61 (1992).
- ¹³D. R. Cole, A. A. Chialvo, G. Rother, L. Vlcek, and P. T. Cummings, "Supercritical fluid behavior at nanoscale interfaces: Implications for CO₂ sequestration in geologic formations," *Philosophical Magazine*, **90**[17] 2339 - 63 (2010).
- ¹⁴"Carbon Sequestration Atlas of the United State and Canada." in Department of Energy, 2010.
- ¹⁵R. T. Wilkin and D. C. DiGiulio, "Geochemical Impacts to Groundwater from Geologic Carbon Sequestration: Controls on pH and Inorganic Carbon Concentrations from Reaction Path and Kinetic Modeling," *Environmental Science & Technology*, **44**[12] 4821-27 (2011).
- ¹⁶F. Bruneval, D. Donadio, and M. Parrinello, "Molecular Dynamics Study of the Solvation of Calcium Carbonate in Water," *The Journal of Physical Chemistry B*, **111**[42] 12219-27 (2007).
- ¹⁷D. D. Di Tommaso and N. H. de Leeuw, "Structure and Dynamics of the Hydrated Magnesium Ion and of the Solvated Magnesium Carbonates: Insights from First Principles Simulations," *Physical Chemistry Chemical Physics*, **12**[4] 894-901 (2010).
- ¹⁸G. A. Tribello, F. Bruneval, C. Liew, and M. Parrinello, "A Molecular Dynamics Study of the Early Stages of Calcium Carbonate Growth," *The Journal of Physical Chemistry B*, **113**[34] 11680-87 (2009).
- ¹⁹P. Raiteri, J. D. Gale, D. Quigley, and P. M. Rodger, "Derivation of an Accurate Force-Field for Simulating the Growth of Calcium Carbonate from Aqueous Solution: A New Model for the Calcite-Water Interface," *The Journal of Physical Chemistry C*, **114**[13] 5997-6010 (2010).
- ²⁰P. Raiteri and J. D. Gale, "Water Is the Key to Nonclassical Nucleation of Amorphous Calcium Carbonate," *Journal of the American Chemical Society*, **132**[49] 17623-34 (2010).
- ²¹A. L. Goodwin, F. M. Michel, B. L. Phillips, D. A. Keen, M. T. Dove, and R. J. Reeder, "Nanoporous Structure and Medium-Range Order in Synthetic Amorphous Calcium Carbonate," *Chemistry of Materials*, **22**[10] 3197-205 (2010).
- ²²R. Demichelis, P. Raiteri, J. D. Gale, D. Quigley, and D. Gebauer, "Stable Prenucleation Mineral Clusters are Liquid-Like Ionic Polymers," *Nat Commun*, **2** 590 (2011).
- ²³D. Gebauer, A. Volkel, and H. Colfen, "Stable Prenucleation Calcium Carbonate Clusters," *Science*, **322**[5909] 1819-22 (2008).

- ²⁴E. Beniash, R. A. Metzler, R. S. K. Lam, and P. U. P. A. Gilbert, "Transient Amorphous Calcium Phosphate in Forming Enamel," *Journal of Structural Biology*, **166**[2] 133-43 (2009).
- ²⁵Y. Li and W. Weng, "In Vitro Synthesis and Characterization of Amorphous Calcium Phosphates with Various Ca/P Atomic Ratios," *Journal of Materials Science: Materials in Medicine*, **18**[12] 2303-08 (2007).
- ²⁶Y.-W. Wang, Y.-Y. Kim, H. K. Christenson, and F. C. Meldrum, "A New Precipitation Pathway for Calcium Sulfate Dihydrate (Gypsum) Via Amorphous and Hemihydrate Intermediates," *Chemical Communications*, **48**[4] 504-06 (2012).
- ²⁷D. Langmuir, J. Mahoney, and J. Rowson, "Solubility Products of Amorphous Ferric Arsenate and Crystalline Scorodite and their Application to Arsenic Behavior in Buried Mine Tailings," *Geochimica et Cosmochimica Acta*, **70**[12] 2942-56 (2006).
- ²⁸J. Johnston, "The Several Forms of Calcium Carbonate," *American Journal of Science*, **41**[246] 473-512 (1916).
- ²⁹T. Tarutani, R. N. Clayton, and T. K. Mayeda, "The Effect of Polymorphism and Magnesium Substitution on Oxygen Isotope Fractionation Between Calcium Carbonate and Water," *Geochimica et Cosmochimica Acta*, **33**[8] 987-96 (1969).
- ³⁰K. Sawada, T. Ogino, and T. Suzuki, "The Distribution Coefficients of Mg²⁺ Ion Between CaCO₃ Polymorphs and Solution and the Effects on the Formation and Transformation of CaCO₃ in Water," *Journal of Crystal Growth*, **106**[2-3] 393-99 (1990).
- ³¹M. G. Taylor, K. Simkiss, G. N. Greaves, M. Okazaki, and S. Mann, "An X-Ray Absorption Spectroscopy Study of the Structure and Transformation of Amorphous Calcium Carbonate from Plant Cystoliths," *Proceedings of the Royal Society of London. Series B: Biological Sciences*, **252**[1333] 75-80 (1993).
- ³²E. Loste, R. M. Wilson, R. Seshadri, and F. C. Meldrum, "The Role of Magnesium in Stabilising Amorphous Calcium Carbonate and Controlling Calcite Morphologies," *Journal of Crystal Growth*, **254**[1-2] 206-18 (2003).
- ³³H. Nebel and M. Epple, "Continuous Preparation of Calcite, Aragonite and Vaterite, and of Magnesium-Substituted Amorphous Calcium Carbonate (Mg-ACC)," *Zeitschrift für Anorganische und Allgemeine Chemie*, **634**[8] 1439-43 (2008).
- ³⁴Y. Politi, D. R. Batchelor, P. Zaslansky, B. F. Chmelka, J. C. Weaver, I. Sagi, S. Weiner, and L. Addadi, "Role of Magnesium Ion in the Stabilization of Biogenic Amorphous Calcium Carbonate: A Structure, Function Investigation," *Chemistry of Materials*, **22**[1] 161-66 (2009).

- ³⁵D. Wang, A. F. Wallace, J. J. De Yoreo, and P. M. Dove, "Carboxylated Molecules Regulate Magnesium Content of Amorphous Calcium Carbonates During Calcification," *Proceedings of the National Academy of Sciences*, **106**[51] 21511-16 (2009).
- ³⁶J. R. O'Neil and S. Epstein, "Oxygen Isotope Fractionation in the System Dolomite-Calcite-Carbon Dioxide," *Science*, **152**[3719] 198-201 (1966).
- ³⁷O. Liebermann, "Synthesis of Dolomite," *Nature*, **213**[5073] 241-45 (1967).
- ³⁸J. C. Deelman, "Dolomite Synthesis and Crystal Growth," *Geology*, **3**[8] 471-72 (1975).
- ³⁹Althoff, "Structural Refinements of Dolomite and a Magnesian Calcite and Implications for Dolomite Formation in the Marine Environment " *American Mineralogist*, **62** 772-83 (1977).
- ⁴⁰L. S. Land, "Failure to Precipitate Dolomite at 25°C from Dilute Solution Despite 1000-Fold Oversaturation after 32 Years," *Aquatic Geochemistry*, **4**[3] 361-68 (1998).
- ⁴¹R. S. Arvidson and F. T. Mackenzie, "The Dolomite Problem; Control of Precipitation Kinetics by Temperature and Saturation State," *American Journal of Science*, **299**[4] 257-88 (1999).
- ⁴²R. Warthmann, Y. van Lith, C. Vasconcelos, J. A. McKenzie, and A. M. Karpoff, "Bacterially Induced Dolomite Precipitation in Anoxic Culture Experiments," *Geology*, **28**[12] 1091-94 (2000).
- ⁴³N. H. de Leeuw and S. C. Parker, "Surface-water Interactions in the Dolomite Problem," *Physical Chemistry Chemical Physics*, **3**[15] 3217-21 (2001).
- ⁴⁴N. Nassif, N. Pinna, N. Gehrke, M. Antonietti, C. Jager, and H. Colfen, "Amorphous Layer Around Aragonite Platelets in Nacre," *Proceedings of the National Academy of Sciences of the United States of America*, **102**[36] 12653-55 (2005).
- ⁴⁵G.-T. Zhou, Q.-Z. Yao, J. Ni, and G. Jin, "Formation of Aragonite Mesocrystals and Implication for Biomineralization," *American Mineralogist*, **94**[2-3] 293-302 (2009).
- ⁴⁶J. H. E. Cartwright, A. G. Checa, J. D. Gale, D. Gebauer, and C. I. Sainz-Díaz, "Calcium Carbonate Polyamorphism and Its Role in Biomineralization: How Many Amorphous Calcium Carbonates Are There?," *Angewandte Chemie International Edition*, **51**[48] 11960-70 (2012).
- ⁴⁷M. D. White, B. P. McGrail, H. T. Schaefer, and D. H. Bacon, "Numerically Simulating Carbonate Mineralization of Basalt with Injection of Carbon Dioxide into Deep Saline Formations," in *Proceedings of the XVI International Conference on Computational Methods in Water Resources*.

- ⁴⁸T. Xu, J. A. Apps, and K. Pruess, "Mineral Sequestration of Carbon Dioxide in a Sandstone and Shale System," *Chemical Geology*, **217**[3,Äi4] 295-318 (2005).
- ⁴⁹B. Hasse, H. Ehrenberg, J. C. Marxen, W. Becker, and M. Epple, "Calcium Carbonate Modifications in the Mineralized Shell of the Freshwater Snail *Biomphalaria glabrata*," *Chemistry – A European Journal*, **6**[20] 3679-85 (2000).
- ⁵⁰B. C. Bostick, M. A. Vairavamurthy, K. G. Karthikeyan, and J. Chorover, "Cesium Adsorption on Clay Minerals: An EXAFS Spectroscopic Investigation," *Environ Sci. Technol*, **36**[12] 2670 (2002).
- ⁵¹B. Hasse, J. C. Marxen, W. Becker, H. Ehrenberg, and M. Epple, "A Crystallographic Study of the Love Dart (*Gypsobelum*) of the Land Snail *Helix Pomatia*," *Journal of Molluscan Studies*, **68**[3] 249-54 (2002).
- ⁵²Y. Levi-Kalisman, S. Raz, S. Weiner, L. Addadi, and I. Sagi, "Structural Differences Between Biogenic Amorphous Calcium Carbonate Phases Using X-ray Absorption Spectroscopy," *Advanced Functional Materials*, **12**[1] 43-48 (2002).
- ⁵³A. Becker, U. Bismayer, M. Epple, H. Fabritius, B. Hasse, J. Shi, and A. Ziegler, "Structural Characterisation of X-ray Amorphous Calcium Carbonate (ACC) in Sternal Deposits of the Crustacea *Porcellio Scaber*," *Dalton Transactions*[4] 551-55 (2003).
- ⁵⁴A. A. Finch and N. Allison, "Coordination of Sr and Mg in Calcite and Aragonite," *Mineralogical Magazine*, **71**[5] 539-52 (2007).
- ⁵⁵D. Gebauer, P. N. Gunawidjaja, J. Y. P. Ko, Z. Bacsik, B. Aziz, L. Liu, Y. Hu, L. Bergström, C.-W. Tai, T.-K. Sham, M. Edén, and N. Hedin, "Proto-Calcite and Proto-Vaterite in Amorphous Calcium Carbonates," *Angewandte Chemie International Edition*, **49**[47] 8889-91 (2010).
- ⁵⁶Y. Politi, Y. Levi-Kalisman, S. Raz, F. Wilt, L. Addadi, S. Weiner, and I. Sagi, "Structural Characterization of the Transient Amorphous Calcium Carbonate Precursor Phase in Sea Urchin Embryos," *Advanced Functional Materials*, **16**[10] 1289-98 (2006).
- ⁵⁷Y. Politi, R. A. Metzler, M. Abrecht, B. Gilbert, F. H. Wilt, I. Sagi, L. Addadi, S. Weiner, and P. U. P. A. Gilbert, "Transformation Mechanism of Amorphous Calcium Carbonate into Calcite in the Sea Urchin Larval Spicule," *Proceedings of the National Academy of Sciences*, **105**[45] 17362-66 (2008).
- ⁵⁸Y. Ma, B. Aichmayer, O. Paris, P. Fratzl, A. Meibom, R. A. Metzler, Y. Politi, L. Addadi, P. U. P. A. Gilbert, and S. Weiner, "The Grinding Tip of the Sea Urchin Tooth Exhibits Exquisite Control Over Calcite Crystal Orientation and Mg Distribution," *Proceedings of the National Academy of Sciences*, **106**[15] 6048-53 (2009).

- ⁵⁹P. U. P. A. Gilbert, A. Young, and S. N. Coppersmith, "Measurement of C-Axis Angular Orientation in Calcite (CaCO₃) Nanocrystals Using X-ray Absorption Spectroscopy," *Proceedings of the National Academy of Sciences*, **108** 11350-55 (2011).
- ⁶⁰Y. U. T. Gong, C. E. Killian, I. C. Olson, N. P. Appathurai, A. L. Amasino, M. C. Martin, L. J. Holt, F. H. Wilt, and P. U. P. A. Gilbert, "Phase Transitions in Biogenic Amorphous Calcium Carbonate," *Proceedings of the National Academy of Sciences*, **109** 6088-93 (2012).
- ⁶¹B. Meyer, "The Pseudopotential Plane Wave Approach," pp. 71-83. in *Computational Nanoscience: Do It Yourself! NIC Series*. Edited by S. B. g. J. Grotendorst, D. Marx. John von Neumann Institute for Computing, Ju'lich, 2006.
- ⁶²T. Charpentier, "The PAW/GIPAW Approach for Computing NMR Parameters: A New Dimension Added to NMR Study of Solids," *Solid State Nuclear Magnetic Resonance*, **40**[1] 1-20 (2011).
- ⁶³M. Bak, J. T. Rasmussen, and N. C. Nielsen, "SIMPSON: A General Simulation Program for Solid-State NMR Spectroscopy," *Journal of Magnetic Resonance*, **147**[2] 296-330 (2000).
- ⁶⁴L. Addadi, S. Raz, and S. Weiner, "Taking Advantage of Disorder: Amorphous Calcium Carbonate and Its Roles in Biomineralization," *Advanced Materials*, **15**[12] 959-70 (2003).
- ⁶⁵L. Addadi and S. Weiner, "Control and Design Principles in Biological Mineralization," *Chem. Int. Ed. Engl.*, **31**[2] 153-69 (1992).
- ⁶⁶E. Beniash, J. Aizenberg, L. Addadi, and S. Weiner, "Amorphous Calcium Carbonate Transforms Into Calcite During Sea Urchin Larval Spicule Growth," *Proc Biol Sci.* , **264**[1380] 461-65 (1997).
- ⁶⁷J. Aizenberg, G. Lambert, S. Weiner, and L. Addadi, "Factors Involved in the Formation of Amorphous and Crystalline Calcium Carbonate: A Study of an Ascidian Skeleton," *J. Am. Chem. Soc.*, **124**[1] 32-39 (2002).
- ⁶⁸X.-R. Xu, A.-H. Cai, R. Liu, H.-H. Pan, R.-K. Tang, and K. Cho, "The Roles of Water and Polyelectrolytes in the Phase Transformation of Amorphous Calcium Carbonate," *Journal of Crystal Growth*, **310**[16] 3779-87 (2008).
- ⁶⁹S. Eloneva, S. Teir, J. Salminen, C.-J. Fogelholm, and R. Zevenhoven, "Fixation of CO₂ by Carbonating Calcium Derived from Blast Furnace Slag," *Energy*, **33**[9] 1461-67 (2008).
- ⁷⁰J. W. Johnson, J. J. Nitao, C. I. Steefel, and K. G. Knauss, "Reactive Transport Modeling of Geologic CO₂ Sequestration in Saline Aquifers: The Influence of Intra-Aquifer Shales and the Relative Effectiveness of Structural, Solubility, and Mineral Trapping During

Prograde and Retrograde Sequestration." in Lawrence Livermore National Laboratory Geosciences and Environmental Technologies Division. 2012.

- ⁷¹M. D. White, B. P. McGrail, J. Gale, and Y. Kaya, "Numerical Investigations of Multifluid Hydrodynamics During Injection of Supercritical CO₂ into Porous Media," pp. pp. 449-56. in 6th International Conference on Greenhouse Gas Control Technologies. 2003.
- ⁷²Y. Fang, B. Baojun, T. Dazhen, S. Dunn-Norman, and D. Wronkiewicz, "Characteristics of CO₂ Sequestration in Saline Aquifers," *Journal of Petroleum Science and Engineering*, **7** 83-92 (2010).
- ⁷³O. Sel, A. V. Radha, K. Dideriksen, and A. Navrotsky, "Amorphous iron (II) carbonate: Crystallization energetics and comparison to other carbonate minerals related to CO₂ sequestration," *Geochimica et Cosmochimica Acta*, **87**[0] 61-68 (2012).
- ⁷⁴D. Baer, N. Hess, D. Hoyt, A. S. Lea, and C. Wang, "Developing Unique Research Tools to Study Carbon Sequestration and Energy Storage," *Meeting Abstracts*, **MA2011-01**[4] 155 (2011).
- ⁷⁵E. H. Oelkers, S. R. Gislason, and J. Matter, "Mineral Carbonation of CO₂," *Elements*, **4**[5] 333-37 (2008).
- ⁷⁶D. P. Schrag, D. J. DePaolo, and F. M. Richter, "Reconstructing Past Sea Surface Temperatures: Correcting for Diagenesis of Bulk Marine Carbonate," *Geochimica et Cosmochimica Acta*, **59**[11] 2265-78 (1995).
- ⁷⁷M. Cusack, A. Perez-Huerta, M. Janousch, and A. A. Finch, "Magnesium in the Lattice of Calcite-Shelled Brachiopods," *Chemical Geology*, **257**[1-2] 59-64 (2008).
- ⁷⁸D. J. DePaolo, "Surface Kinetic Model for Isotopic and Trace Element Fractionation During Precipitation of Calcite from Aqueous Solutions," *Geochimica et Cosmochimica Acta*, **75**[4] 1039-56 (2011).
- ⁷⁹L. C. Foster, N. Allison, A. A. Finch, and C. Andersson, "Strontium Distribution in the Shell of the Aragonite Bivalve *Arctica islandica*," *Geochem. Geophys. Geosyst.*, **10**[3] Q03003 (2009).
- ⁸⁰A. C. Gagnon, J. F. Adkins, and J. Erez, "Seawater Transport During Coral Biomineralization," *Earth and Planetary Science Letters*, **329-330** 150-61 (2012).
- ⁸¹B. C. Gill, T. W. Lyons, and T. D. Frank, "Behavior of Carbonate-Associated Sulfate During Meteoric Diagenesis and Implications for the Sulfur Isotope Paleoproxy," *Geochimica et Cosmochimica Acta*, **72**[19] 4699-711 (2008).

- ⁸²M. Cusack, J. England, P. Dalbeck, A. Tudhope, A. Fallick, and N. Allison, "Electron Backscatter Diffraction (EBSD) as a Tool for Detection of Coral Diagenesis," *Coral Reefs*, **27**[4] 905-11 (2008).
- ⁸³A. E. Hofmann, I. C. Bourg, and D. J. DePaolo, "Ion Desolvation as a Mechanism for Kinetic Isotope Fractionation in Aqueous Systems," *Proceedings of the National Academy of Sciences* (2012).
- ⁸⁴D. J. Sinclair, "Correlated Trace Element "Vital Effects" in Tropical Corals: A New Geochemical Tool for Probing Biomineralization," *Geochimica et Cosmochimica Acta*, **69**[13] 3265-84 (2005).
- ⁸⁵S. Bentov, S. Weil, L. Glazer, A. Sagi, and A. Berman, "Stabilization of Amorphous Calcium Carbonate by Phosphate Rich Organic Matrix Proteins and by Single Phosphoamino Acids," *Journal of Structural Biology*, **171**[2] 207-15 (2010).
- ⁸⁶H. Li, H. L. Xin, D. A. Muller, and L. A. Estroff, "Visualizing the 3D Internal Structure of Calcite Single Crystals Grown in Agarose Hydrogels," *Science*, **326**[5957] 1244-47 (2009).
- ⁸⁷S. B. Mukkamala, C. E. Anson, and A. K. Powell, "Modelling Calcium Carbonate Biomineralisation Processes," *Journal of Inorganic Biochemistry*, **100**[5-6] 1128-38 (2006).
- ⁸⁸S. Ouhenia, D. Chateigner, M. A. Belkhir, E. Guilmeau, and C. Krauss, "Synthesis of Calcium Carbonate Polymorphs in the Presence of Polyacrylic Acid," *Journal of Crystal Growth*, **310**[11] 2832-41 (2008).
- ⁸⁹L. Gago-Duport, M. J. I. Briones, J. B. Rodríguez, and B. Covelo, "Amorphous Calcium Carbonate Biomineralization in the Earthworm's Calciferous Gland: Pathways to the Formation of Crystalline Phases," *Journal of Structural Biology*, **162**[3] 422-35 (2008).
- ⁹⁰S. Raz, P. C. Hamilton, F. H. Wilt, S. Weiner, and L. Addadi, "The Transient Phase of Amorphous Calcium Carbonate in Sea Urchin Larval Spicules: The Involvement of Proteins and Magnesium Ions in Its Formation and Stabilization," *Advanced Functional Materials*, **13**[6] 480-86 (2003).
- ⁹¹M. Seorale-Pose, C. Chalar, Y. Dauphin, P. Massard, P. Pradel, and M. Marín, "Monohydrocalcite in Calcareous Corpuscles of *Mesocestoides Corti*," *Experimental Parasitology*, **118**[1] 54-58 (2008).
- ⁹²V. Mattigod Shas and G. Sposito, "Chemical Modeling of Trace Metal Equilibria in Contaminated Soil Solutions Using the Computer Program GEOCHEM," pp. 837-56. in *Chemical Modeling in Aqueous Systems*, Vol. **93**. *ACS Symposium Series*. American Chemical Society, 1979.

- ⁹³C. M. Carey, T. M. Gregory, A. Tatevossian, and G. L. Vogel, "The Buffer Capacity of Single-Site, Resting, Human Dental-Plaque Fluid," *Archives of Oral Biology*, **33**[7] 487-92 (1988).
- ⁹⁴W. E. Brown and L. C. Chow, "Chemical Properties of Bone Mineral," *Annual Review of Materials Science*, **6**[1] 213-36 (1976).
- ⁹⁵L. L. Hench, "Genetic Design of Bioactive Glass," *Journal of the European Ceramic Society*, **29**[7] 1257-65 (2009).
- ⁹⁶J. R. Jones, E. Gentleman, and J. Polak, "Bioactive Glass Scaffolds for Bone Regeneration," *Elements*, **3**[6] 393-99 (2007).
- ⁹⁷S. Camprasse, G. Camprasse, M. Pouzol, and E. Lopez, "Artificial Dental Root Made of Natural Calcium Carbonate (Bioracine)," *Clinical Materials*, **5**[2-4] 235-50 (1990).
- ⁹⁸P. Fratzl, F. D. Fischer, J. Svoboda, and J. Aizenberg, "A Kinetic Model of the Transformation of a Micropatterned Amorphous Precursor into a Porous Single Crystal," *Acta Biomaterialia*, **6**[3] 1001-05 (2010).
- ⁹⁹D. Di Tommaso and N. H. de Leeuw, "Theoretical Study of the Dimerization of Calcium Carbonate in Aqueous Solution Under Natural Water Conditions," *Geochimica et Cosmochimica Acta*, **73**[18] 5394-405 (2009).
- ¹⁰⁰A. F. Wallace, J. F. Banfield, and J. D. Yoreo, "Liquid-liquid Separation Explains "Non-classical" Behavior During Calcium Carbonate Crystallization." in American Geophysical Union, **Vol. Fall 2012**. San Fransisco, CA, 2012.
- ¹⁰¹J. W. Singer, A. O. Yazaydin, R. J. Kirkpatrick, and G. M. Bowers, "Structure and Transformation of Amorphous Calcium Carbonate: a Solid-State ⁴³Ca NMR and Computational Molecular Dynamics Investigation," *Chemistry of Materials*, **24**[10] 1828-36 (2012).
- ¹⁰²A. V. Radha, A. Fernandez-Martinez, Y. Hu, Y.-S. Jun, G. A. Waychunas, and A. Navrotsky, "Energetic and Structural Studies of Amorphous (Ca,Mg) CO₃ nH₂O," *Geochimica et Cosmochimica Acta*, **90**[0] 83-95 (2012).
- ¹⁰³E. M. Pouget, P. H. H. Bomans, J. A. C. M. Goos, P. M. Frederik, G. de With, and N. A. J. M. Sommerdijk, "The Initial Stages of Template-Controlled CaCO₃ Formation Revealed by Cryo-TEM," *Science*, **323**[5920] 1455-58 (2009).
- ¹⁰⁴F. Zhang, H. Xu, H. Konishi, E. S. Shelobolina, and E. E. Roden, "Polysaccharide-Catalyzed Nucleation and Growth of Disordered Dolomite: A Potential Precursor of Sedimentary Dolomite," *American Mineralogist*, **97**[4] 556-67 (2012).

- ¹⁰⁵Y. W. Wang, Y. Y. Kim, C. J. Stephens, F. C. Meldrum, and H. K. Christenson, "In Situ Study of the Precipitation and Crystallization of Amorphous Calcium Carbonate (ACC)," *Crystal Growth & Design*, **12**[3] 1212-17 (2012).
- ¹⁰⁶J. D. Rodriguez-Blanco, S. Shaw, and L. G. Benning, "The Kinetics and Mechanisms of Amorphous Calcium Carbonate (ACC) Crystallization to Calcite, via Vaterite," *Nanoscale*, **3** 265-71 (2011).
- ¹⁰⁷L. C. Jacobson, W. Hujo, and V. Molinero, "Amorphous Precursors in the Nucleation of Clathrate Hydrates," *Journal of the American Chemical Society*, **132**[33] 11806-11 (2010).
- ¹⁰⁸L. C. Jacobson, W. Hujo, and V. Molinero, "Nucleation Pathways of Clathrate Hydrates: Effect of Guest Size and Solubility," *The Journal of Physical Chemistry B*, **114**[43] 13796-807 (2010).
- ¹⁰⁹R. Isopescu, C. Mateescu, M. Mihai, and G. Dabija, "The Effects of Organic Additives on Induction Time and Characteristics of Precipitated Calcium Carbonate," *Chemical Engineering Research and Design*, **88**[11] 1450-54 (2009).
- ¹¹⁰L. Fernandez-Diaz, C. M. Pina, J. M. Astilleros, and N. Sanchez-Pastor, "The Carbonatation of Gypsum: Pathways and Pseudomorph Formation," *American Mineralogist*, **94**[8-9] 1223-34 (2009).
- ¹¹¹D. Quigley and P. M. Rodger, "Free Energy and Structure of Calcium Carbonate Nanoparticles During Early Stages of Crystallization," *The Journal of Chemical Physics*, **128**[22] 221101-4 (2008).
- ¹¹²F. M. Michel, J. MacDonald, J. Feng, B. L. Phillips, L. Ehm, C. Tarabrella, J. B. Parise, and R. J. Reeder, "Structural Characteristics of Synthetic Amorphous Calcium Carbonate," *Chemistry of Materials*, **20**[14] 4720-28 (2008).
- ¹¹³B. Njagic-Dzakula, G. Falini, L. Brecevic, Z. Skoko, and D. Kralj, "Effects of Initial Supersaturation on Spontaneous Precipitation of Calcium Carbonate in the Presence of Charged Poly-l-Amino Acids," *Journal of Colloid and Interface Science*, **343**[2] 553-63 (2010).
- ¹¹⁴S. Dupraz, M. Parmentier, B. Menez, and F. Guyot, "Experimental and Numerical Modeling of Bacterially Induced pH Increase and Calcite Precipitation in Saline Aquifers," *Chemical Geology*, **265**[1-2] 44-53 (2009).
- ¹¹⁵E. Griesshaber, K. Kelm, A. Sehrbrock, W. Mader, J. Mutterlose, U. Brand, and W. W. Schmahl, "Amorphous Calcium Carbonate in the Shell Material of the Brachiopod *Megerlia truncata*," *Eur J Mineral*, **21**[4] 715-23 (2009).

- ¹¹⁶D. E. Jacob, R. Wirth, A. L. Soldati, U. Wehrmeister, and A. Schreiber, "Amorphous Calcium Carbonate in the Shells of Adult Unionoida," *Journal of Structural Biology*, **173**[2] 241-49 (2011).
- ¹¹⁷X.-H. Guo, A.-W. Xu, and S.-H. Yu, "Crystallization of Calcium Carbonate Mineral with Hierarchical Structures in DMF Solution under Control of Poly(Ethylene Glycol)-bPoly(L-Glutamic Acid): Effects of Crystallization Temperature and Polymer Concentration," *Crystal Growth & Design*, **8**[4] 1233-42 (2008).
- ¹¹⁸W. K. Park, S.-J. Ko, S. W. Lee, K.-H. Cho, J.-W. Ahn, and C. Han, "Effects of Magnesium Chloride and Organic Additives on the Synthesis of Aragonite Precipitated Calcium Carbonate," *Journal of Crystal Growth*, **310**[10] 2593-601 (2008).
- ¹¹⁹M. Barabas, A. Bach, M. Mudelsee, and A. Mangini, "Influence of the Mg-Content on ESR-Signals in Synthetic Calcium Carbonate," *International Journal of Radiation Applications and Instrumentation. Part A. Applied Radiation and Isotopes*, **40**[10-12] 1105-11 (1989).
- ¹²⁰T. Chen, A. Neville, and M. Yuan, "Assessing the Effect of Mg²⁺ on CaCO₃ Scale Formation-Bulk Precipitation and Surface deposition," *Journal of Crystal Growth*, **275**[1-2] e1341-e47 (2005).
- ¹²¹F. Dejehet, S. Idrissi, and R. Debuys, "Magnesium and Occluded Water in Calcium Carbonate Monohydrate," *J. Chim. Phys.*, **96**[4] 741-53 (1999).
- ¹²²L. Fernandez-Diaz, A. Putnis, M. Prieto, and C. V. Putnis, "The Role of Magnesium in the Crystallization of Calcite and Aragonite in a Porous Medium," *Journal of Sedimentary Research*, **66**[3] 482-91 (1996).
- ¹²³M. M. Reddy and G. H. Nancollas, "The Crystallization of Calcium Carbonate : IV. The Effect of Magnesium, Strontium and Sulfate Ions," *Journal of Crystal Growth*, **35**[1] 33-38 (1976).
- ¹²⁴R. Wollast, "Rate and Mechanism of Dissolution of Carbonates in the System CaCO₃-MgCO₃," pp. 431-45. in *Aquatic Chemical Kinetics*. Edited by W. Stumm. Wiley, 1990.
- ¹²⁵N. Folliet, C. Roiland, S. Begu, A. Aubert, T. Mineva, A. Goursot, K. Selvaraj, L. Duma, F. Tielens, F. Mauri, G. Laurent, C. Bonhomme, C. Gervais, F. Babonneau, and T. Azaos, "Investigation of the Interface in Silica-Encapsulated Liposomes by Combining Solid State NMR and First Principles Calculations," *Journal of the American Chemical Society*, **133**[42] 16815-27 (2011).
- ¹²⁶M. Kellermeier, E. Melero-Garcia, F. Glaab, R. Klein, M. Drechsler, R. Rachel, J. M. Garcia-Ruiz, and W. Kunz, "Stabilization of Amorphous Calcium Carbonate in Inorganic Silica-Rich Environments," *Journal of the American Chemical Society*, **132**[50] 17859-66 (2010).

- ¹²⁷A. Becker, U. Bismayer, M. Epple, H. Fabritius, B. Hasse, J. Shi, and A. Ziegler, "Structural Characterisation of X-ray Amorphous Calcium Carbonate (ACC) in Sternal Deposits of the Crustacea *Porcellio Scaber*," *Dalton Transactions*[4] (2003).
- ¹²⁸R. S. K. Lam, J. M. Charnock, A. Lenniec, and F. C. Meldrum, "Synthesis-Dependant Structural Variations in Amorphous Calcium Carbonate," *Crystal Engineering Communication*, **9** 1226–36 (2007).
- ¹²⁹V. Pipich, M. Balz, S. E. Wolf, W. Tremel, and D. Schwahn, "Nucleation and Growth of CaCO₃ Mediated by the Egg-White Protein Ovalbumin: A Time-Resolved in situ Study Using Small-Angle Neutron Scattering," *Journal of the American Chemical Society*, **130**[21] 6879-92 (2008).
- ¹³⁰S. E. Wolf, J. Leiterer, V. Pipich, R. Barrea, F. Emmerling, and W. Tremel, "Strong Stabilization of Amorphous Calcium Carbonate Emulsion by Ovalbumin: Gaining Insight into the Mechanism of Polymer-Induced Liquid Precursor Processes," *Journal of the American Chemical Society*, **133**[32] 12642-49 (2011).
- ¹³¹W. D. Bischoff, F. T. Mackenzie, and F. C. Bishop, "Stabilities of Synthetic Magnesian Calcites in Aqueous Solution: Comparison with Biogenic Materials," *Geochimica et Cosmochimica Acta*, **51**[6] 1413-23 (1987).
- ¹³²W. D. Bischoff, S. K. Sharma, and F. T. Mackenzie, "Carbonate Ion Disorder in Synthetic and Biogenic Magnesian Calcites: a Raman Spectral Study," *Am. Mineral.*, **70**[5-6] 581-9 (1985).
- ¹³³V. T. C. Chang, R. J. P. Williams, A. Makishima, N. S. Belshaw, and R. K. O'Nions, "Mg and Ca Isotope Fractionation During CaCO₃ Biomineralisation," *Biochemical and Biophysical Research Communications*, **323**[1] 79-85 (2004).
- ¹³⁴L. C. Foster, A. A. Finch, N. Allison, C. Andersson, and L. J. Clarke, "Mg in Aragonitic Bivalve Shells: Seasonal Variations and Mode of Incorporation in *Arctica Islandica*," *Chemical Geology*, **254**[1-2] 113-19 (2008).
- ¹³⁵Y. Kitano, A. Tokuyama, and T. Arakaki, "Magnesian Calcite Synthesis from Calcium Bicarbonate Solution Containing Magnesium and Barium Ions," *Geochemical Journal*, **13** 181-85 (1979).
- ¹³⁶S. D. Skapin and I. Sondi, "Homogeneous Precipitation of Mixed Anhydrous Ca,Mg and Ba,Sr Carbonates by Enzyme-Catalyzed Reaction," *Crystal Growth & Design*, **5**[5] 1933-38 (2005).
- ¹³⁷G. A. Gaetani and A. L. Cohen, "Element Partitioning during Precipitation of Aragonite from Seawater: A Framework for Understanding Paleoproxies," *Geochimica et Cosmochimica Acta*, **70**[18] 4617-34 (2006).

- ¹³⁸P. K. Ajikumar, L. G. Wong, G. Subramanyam, R. Lakshminarayanan, and S. Valiyaveetil, "Synthesis and Characterization of Monodispersed Spheres of Amorphous Calcium Carbonate and Calcite Spherules," *Crystal Growth & Design*, **5**[3] 1129-34 (2005).
- ¹³⁹J. Jiang, M.-R. Gao, Y.-H. Qiu, and S.-H. Yu, "Gram-Scale, Low-Cost, Rapid Synthesis of Highly Stable Mg-ACC Nanoparticles and Their Long-Term Preservation," *Nanoscale*, **2**[11] 2358-61 (2010).
- ¹⁴⁰M. Neumann and M. Epple, "Monohydrocalcite and Its Relationship to Hydrated Amorphous Calcium Carbonate in Biominerals," *European Journal of Inorganic Chemistry*, **2007**[14] 1953-57 (2007).
- ¹⁴¹L. M. Hamm, A. F. Wallace, and P. M. Dove, "Molecular Dynamics of Ion Hydration in the Presence of Small Carboxylated Molecules and Implications for Calcification," *The Journal of Physical Chemistry B*, **114**[32] 10488-95 (2010).
- ¹⁴²D. Dissard, G. Nehrke, G. J. Reichart, and J. Bijma, "Impact of Seawater pCO₂ on Calcification and Mg/Ca and Sr/Ca Ratios in Benthic Foraminifera Calcite: Results from Culturing Experiments with *Ammonia tepida*," *Biogeosciences*, **7**[1] 81-93 (2010).
- ¹⁴³D. Di Tommaso and N. H. de Leeuw, "First Principles Simulations of the Structural and Dynamical Properties of Hydrated Metal Ions Me²⁺ and Solvated Metal Carbonates (Me = Ca, Mg, and Sr)," *Crystal Growth & Design*, **10**[10] 4292-302 (2010).
- ¹⁴⁴T. Munemoto and K. Fukushi, "Transformation Kinetics of Monohydrocalcite to Aragonite in Aqueous Solutions," *Journal of Mineralogical and Petrological Sciences*, **103**[5] 345-49 (2008).
- ¹⁴⁵A. Mikkelsen, A. B. Andersen, S. B. Engelsen, H. C. B. Hansen, O. Larsen, and L. H. Skibsted, "Presence and Dehydration of Ikaite, Calcium Carbonate Hexahydrate, in Frozen Shrimp Shell," *Journal of Agricultural and Food Chemistry*, **47**[3] 911-17 (1999).
- ¹⁴⁶I. P. Swainson, "The Structure of Monohydrocalcite and the Phase Composition of the Beachrock Deposits of Lake Butler and Lake Fellmongery, South Australia," *American Mineralogist*, **93**[7] 1014-18 (2008).
- ¹⁴⁷Effenberger, "Kristallstruktur und Infrarot-Absorptionsspektrum von Synthetischen Monohydrocalcit, CaCO₃(H₂O)," *Monatshefte für Chemie und verwandte Teile anderer Wissenschaften*, **112** 899-909 (1981).
- ¹⁴⁸J. Wang and U. Becker, "Energetics and Kinetics of Carbonate Orientational Ordering in Vaterite Calcium Carbonate," *American Mineralogist*, **97**[8-9] 1427-36 (2012).
- ¹⁴⁹S. Kamhi, "On the Structure of Vaterite CaCO₃," *Acta Crystallographica*, **16**[8] 770-72 (1963).

- ¹⁵⁰J. Wang and U. Becker, "Structure and Carbonate Orientation of Vaterite (CaCO₃)," *American Mineralogist*, **94**[2-3] 380-86 (2009).
- ¹⁵¹F. Zhang, H. Xu, H. Konishi, and E. E. Roden, "A Relationship Between d104 Value and Composition in the Calcite-Disordered Dolomite Solid-Solution Series," *American Mineralogist*, **95**[11-12] 1650-56 (2010).
- ¹⁵²A. v. S. Hood, M. W. Wallace, and R. N. Drysdale, "Neoproterozoic Aragonite-Dolomite seas? Widespread Marine Dolomite Precipitation in Cryogenian Reef Complexes," *Geology*, **39**[9] 871-74 (2011).
- ¹⁵³J. M. Ferry, B. H. Passey, C. Vasconcelos, and J. M. Eiler, "Formation of Dolomite at 40-80C in the Latemar Carbonate Buildup, Dolomites, Italy, from Clumped Isotope Thermometry," *Geology*, **39**[6] 571-74 (2011).
- ¹⁵⁴M. Al-Awadi and W. J. Clark, "Dolomite: Perspectives on a Perplexing Mineral," *Oilfield Review*, **21**[3] 32-45 (2009).
- ¹⁵⁵J. C. Deelman, "Low-Temperature Nucleation of Magnesite and Dolomite," *Neue Jahrbuch Mineralogie, Monatshefte.*, **7** 289-302 (1999).
- ¹⁵⁶W. A. Dollase and R. J. Reeder, "Crystal Structure Refinement of Huntite, CaMg₃(CO₃)₄, with X-ray Powderdata," *American Mineralogist*, **71** 163-66 (1986).
- ¹⁵⁷B. Nashar, "Barringtonite—A New Hydrous Magnesium Carbonate from Barrington Tops, New South Wales, Australia," *Mineralogical Magazine*, **34** 370-72 (1965).
- ¹⁵⁸R. Peterson, K. Tait, and I. Nicklin, "Dypingite from Rapid Creek, Yukon, Canada. Chemical Composition, Optical Properties, and Comparison with Similar Hydrated Magnesium Carbonates," in GSA Annual Meeting
- ¹⁵⁹R. Beck and J.-P. Andreassen, "The Onset of Spherulitic Growth in Crystallization of Calcium Carbonate," *Journal of Crystal Growth*, **312**[15] 2226-38 (2010).
- ¹⁶⁰N. Koga, Y. Nakagoe, and H. Tanaka, "Crystallization of Amorphous Calcium Carbonate," *Thermochimica Acta*, **318**[1-2] 239-44 (1998).
- ¹⁶¹S. J. Burns, J. A. McKenzie, and C. Vasconcelos, "Dolomite Formation and Biogeochemical Cycles in the Phanerozoic," *Sedimentology*, **47**[Suppl s1] 49-61 (2000).
- ¹⁶²M. Sánchez-Román, J. A. McKenzie, A. de Luca Rebello Wagener, M. A. Rivadeneyra, and C. Vasconcelos, "Presence of Sulfate Does Not Inhibit Low-Temperature Dolomite Precipitation," *Earth and Planetary Science Letters*, **285**[1-2] 131-39 (2009).

- ¹⁶³M. Sánchez-Román, C. Vasconcelos, R. Warthmann, M. Rivadeneyra, and J. A. McKenzie, "Microbial Dolomite Precipitation under Aerobic Conditions: Results from Brejo do Espinho Lagoon (Brazil) and Culture Experiments," pp. 167-78. in *Perspectives in Carbonate Geology*. John Wiley & Sons, Ltd, 2009.
- ¹⁶⁴J. C. Deelman, "Dolomite Book: Low Temperature Formatio of Dolomite and Magnesite." in., 2011.
- ¹⁶⁵B. Dickens and W. E. Brown, "Crystal Structure of Calcium Carbonate Hexahydrate at About -120 Degrees," *Inorganic Chemistry*, **9**[3] 480-86 (1970).
- ¹⁶⁶A. R. Lennie, C. C. Tang, and S. P. Thompson, "The Structure and Thermal Expansion Behaviour of Ikaite, CaCO₃ 6H₂O, From T = 114 to T = 293 K," *Mineral Mag*, **68**[1] 135-46 (2004).
- ¹⁶⁷K. Dahl and B. Buchardt, "Monohydrocalcite in the Arctic Ikka Fjord, SW Greenland: First Reported Marine Occurrence," *Journal of Sedimentary Research*, **76**[3] 460-71 (2006).
- ¹⁶⁸J. Kawano and et al., "Precipitation Diagram of Calcium Carbonate Polymorphs: Its Construction and Significance," *Journal of Physics: Condensed Matter*, **21**[42] 425102 (2009).
- ¹⁶⁹H. Papenguth, R. J. Kirkpatrick, B. Montez, and P. Sandberg, "¹³C MAS NMR Spectroscopy of Inorganic and Biogenic Carbonates," *American Mineralogist*, **74** 1152-58 (1989).
- ¹⁷⁰K. J. D. MacKenzie and R. H. Meinhold, "²⁵Mg Nuclear Magnetic Resonance Spectroscopy of Minerals and Related Inorganics: A Survey Study.," *American Mineralogist*, **79** 250-60 (1994).
- ¹⁷¹P. J. Pallister, I. L. Moudrakovski, and J. A. Ripmeester, "Mg-25 Ultra-High Field Solid State NMR Spectroscopy and First Principles Calculations of Magnesium Compounds," *Physical Chemistry Chemical Physics*, **11**[48] 11487-500 (2009).
- ¹⁷²S. Melchionna, G. Ciccotti, and B. Lee Holian, "Hoover NPT Dynamics for Systems Varying in Shape and Size," *Molecular Physics*, **78**[3] 533-44 (1993).
- ¹⁷³D. L. Bryce, "Calcium Bbinding Environments Probed by ⁴³Ca NMR Spectroscopy," *Dalton Transactions*, **39**[37] 8593-602 (2010).
- ¹⁷⁴D. L. Bryce, E. B. Bultz, and . Aebi, "Calcium-43 Chemical Shift Tensors as Probes of Calcium Binding Environments. Insight into the Structure of the Vaterite CaCO₃ Polymorph by ⁴³Ca Solid-State NMR Spectroscopy," *Journal of the American Chemical Society*, **130**[29] 9282-92 (2008).

- ¹⁷⁵A. Wong, A. P. Howes, R. Dupree, and M. E. Smith, "Natural Abundance ⁴³Ca NMR Study of Calcium-Containing Organic Solids: A Model Study for Ca-Binding Biomaterials," *Chemical Physics Letters*, **427**[1-3] 201-05 (2006).
- ¹⁷⁶D. Laurencin, C. Gervais, A. Wong, C. Coelho, F. Mauri, D. Massiot, M. E. Smith, and C. Bonhomme, "Implementation of High Resolution ⁴³Ca Solid State NMR Spectroscopy: Toward the Elucidation of Calcium Sites in Biological Materials," *Journal of the American Chemical Society*, **131**[37] 13430-40 (2009).
- ¹⁷⁷K. J. D. MacKenzie and R. H. Meinhold, "²⁵Mg Nuclear Magnetic Resonance Spectroscopy of Minerals and Related Inorganics: A Survey Study," *American Mineralogist*, **79** 250-60 (1994).
- ¹⁷⁸M. Akao, F. Marumo, and S. Iwai, "The Crystal Structure of Hydromagnesite," *Acta Crystallographica Section B*, **30**[11] 2670-72 (1974).
- ¹⁷⁹M. Akao and S. Iwai, "The Hydrogen Bonding of Hydromagnesite," *Acta Crystallographica Section B*, **33**[4] 1273-75 (1977).
- ¹⁸⁰J. K. Harper, "Chemical Shift Anisotropy and Asymmetry: Relationships to Crystal Structure." in *Encyclopedia of Magnetic Resonance*. John Wiley & Sons, Ltd, 2007.
- ¹⁸¹G. Ferlat, T. Charpentier, A. P. Seitsonen, A. Takada, M. Lazzeri, L. Cormier, G. Calas, and F. Mauri, "Boroxol Rings in Liquid and Vitreous B₂O₃ from First Principles," *Physical Review Letters*, **101**[6] 065504-8 (2008).
- ¹⁸²A. Pedone, T. Charpentier, and M. C. Menziani, "Multinuclear NMR of CaSiO₃ Glass: Simulation from First-Principles," *Physical Chemistry Chemical Physics*, **12**[23] 6054-66 (2010).
- ¹⁸³A. Pedone, T. Charpentier, and M. C. Menziani, "The Structure of Fluoride-Containing Bioactive Glasses: New Insights from First-Principles Calculations and Solid State NMR Spectroscopy," *Journal of Materials Chemistry*, **22**[25] 12599-608 (2012).
- ¹⁸⁴A. Soleilhavoup, J.-M. Delaye, F. Angeli, D. Caurant, and T. Charpentier, "Contribution of First-Principles Calculations to Multinuclear NMR Analysis of Borosilicate Glasses," *Magnetic Resonance in Chemistry*, **48**[S1] S159-S70 (2010).
- ¹⁸⁵I. P. Swainson and R. P. Hammond, "Hydrogen bonding in ikaite, CaCO₃ · 6H₂O," *Mineralogical Magazine*, **67**[3] 555-62 (2003).
- ¹⁸⁶C. Gervais, D. Laurencin, A. Wong, F. Pourpoint, J. Labram, B. Woodward, A. P. Howes, K. J. Pike, R. Dupree, F. Mauri, C. Bonhomme, and M. E. Smith, "New Perspectives on Calcium Environments in Inorganic Materials Containing Calcium-Oxygen Bonds: A Combined Computational-Experimental ⁴³Ca NMR Approach," *Chemical Physics Letters*, **464**[1-3] 42-48 (2008).

- ¹⁸⁷D. Laurencin, A. Wong, W. Chrzanowski, J. C. Knowles, D. Qiu, D. M. Pickup, R. J. Newport, Z. Gan, M. J. Duer, and M. E. Smith, "Probing the Calcium and Sodium Local Environment in Bones and Teeth using Multinuclear Solid State NMR and X-ray Absorption Spectroscopy," *Physical Chemistry Chemical Physics*, **12**[5] 1081-91 (2010).
- ¹⁸⁸D. Laurencin, A. Wong, R. Dupree, and M. E. Smith, "Natural Abundance ⁴³Ca Solid-State NMR Characterisation of Hydroxyapatite: Identification of the Two Calcium Sites," *Magnetic Resonance in Chemistry*, **46**[4] 347-50 (2008).
- ¹⁸⁹J. D. Rodriguez-Blanco, S. Shaw, P. Bots, T. Roncal-Herrero, and L. G. Benning, "The Role of pH and Mg on the Stability and Crystallization of Amorphous Calcium Carbonate," *Journal of Alloys and Compounds*, **536**[Suppl 1] S477–S79 (2012).
- ¹⁹⁰L. A. Hollingbery and T. R. Hull, "The Thermal Decomposition of Huntite and Hydromagnesite, A Review," *Thermochimica Acta*, **509**[1-2] 1-11 (2010).
- ¹⁹¹D. Laurencin and M. E. Smith, "Development of ⁴³Ca NMR Solid State NMR Spectroscopy as a Probe of Local Structure in Inorganic and Molecular Materials," *Progress in Nuclear Magnetic Resonance Spectroscopy*, **In Press**[Corrected Proof] (2012).
- ¹⁹²C. Gunther, A. Becker, G. Wolf, and M. Epple, "In Vitro Synthesis and Structural Characterization of Amorphous Calcium Carbonate," *Zeitschrift für Anorganische und Allgemeine Chemie*, **631**[13-14] 2830-35 (2005).
- ¹⁹³K. J. D. MacKenzie and R. H. Meinhold, "Thermal Decomposition of Dolomite (Calcium Magnesium Carbonate) Studied by ²⁵Mg Solid-State Nuclear Magnetic Resonance," *Thermochimica Acta*, **230**[0] 331-37 (1993).
- ¹⁹⁴G. Giester, C. L. Lengauer, and B. Rieck, "The Crystal Structure of Nesquehonite, MgCO₃ · 3H₂O, From Lavrion, Greece," *Mineralogy and Petrology*, **70**[3] 153-63 (2000).
- ¹⁹⁵K. D. Oh, H. Morikawa, S. I. Iwai, and H. Aoki, "The Crystal Structure of Magnesite," *American Mineralogist*, **58** 1029-33 (1973).
- ¹⁹⁶W. Jahnen-Dechent and M. Ketteler, "Magnesium Basics," *Clinical Kidney Journal*, **5**[Suppl 1] i3-i14 (2012).

APPENDIX

Additional results are contained here that were ancillary to the main discussion. Methodological information related to this appendix is given already in the main text. The appendix includes the results of ikaite crystallization experiments, ^{13}C CASTEP NMR calculations, and example input files for CASTEP NMR calculations and SIMPSON simulation.

Ikaite Crystallization Results

Table 10. Fit parameters of ikaite experimental NMR and ^{43}Ca CASTEP NMR

Sample/Site	δ_{iso} (ppm)	C_q (MHz)	η_q	FWHM (Hz)
Experimental*	0.9 ± 0.1	2.43 ± 0.05	0.23 ± 0.02	
CASTEP H-opt	0.28	2.32	0.28	
CASTEP original	-3.8	2.45	0.39	
Experimental**	168.2 ± 0.1	-	-	344 ± 12

δ_{iso} = isotropic chemical shift; C_q = quadrupolar coupling constant; η_q = quadrupolar asymmetry parameter; FWHM = full width at half maximum.

*Fit with SIMPSON⁶³

**Fit with Abscissa

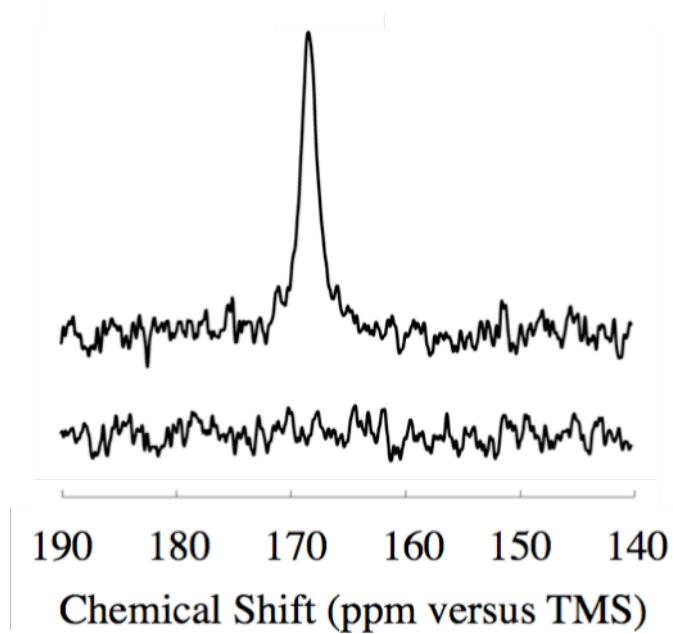


Figure 27. ^1H - ^{13}C CPMAS spectra from 20.0 T for ikaite -5°C . Ikaite ^{13}C - ^1H CP resonance is well-fit with single Lorentzian functions centered at 168.2 ± 0.1 ppm. Heating at 60°C was sufficient to remove all water from the sample (shown by the lower trace).

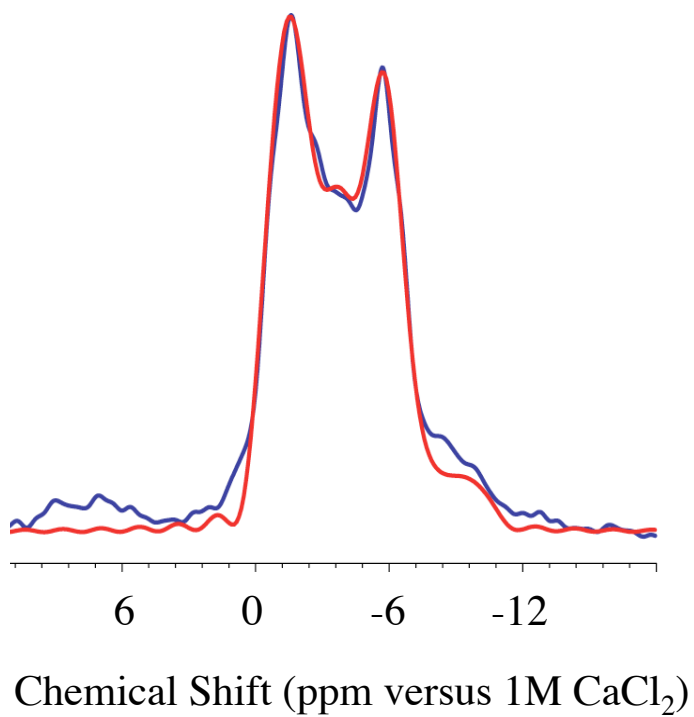


Figure 28. ⁴³Ca MAS NMR spectra and SIMPSON simulations of the ikaite NMR resonance at 20.0 T. Synthetic ikaite specimen is colored blue and the simulation results red. Several spinning sidebands are not shown. The sample exhibited a minute quantity of calcite near 21 ppm that is not shown.

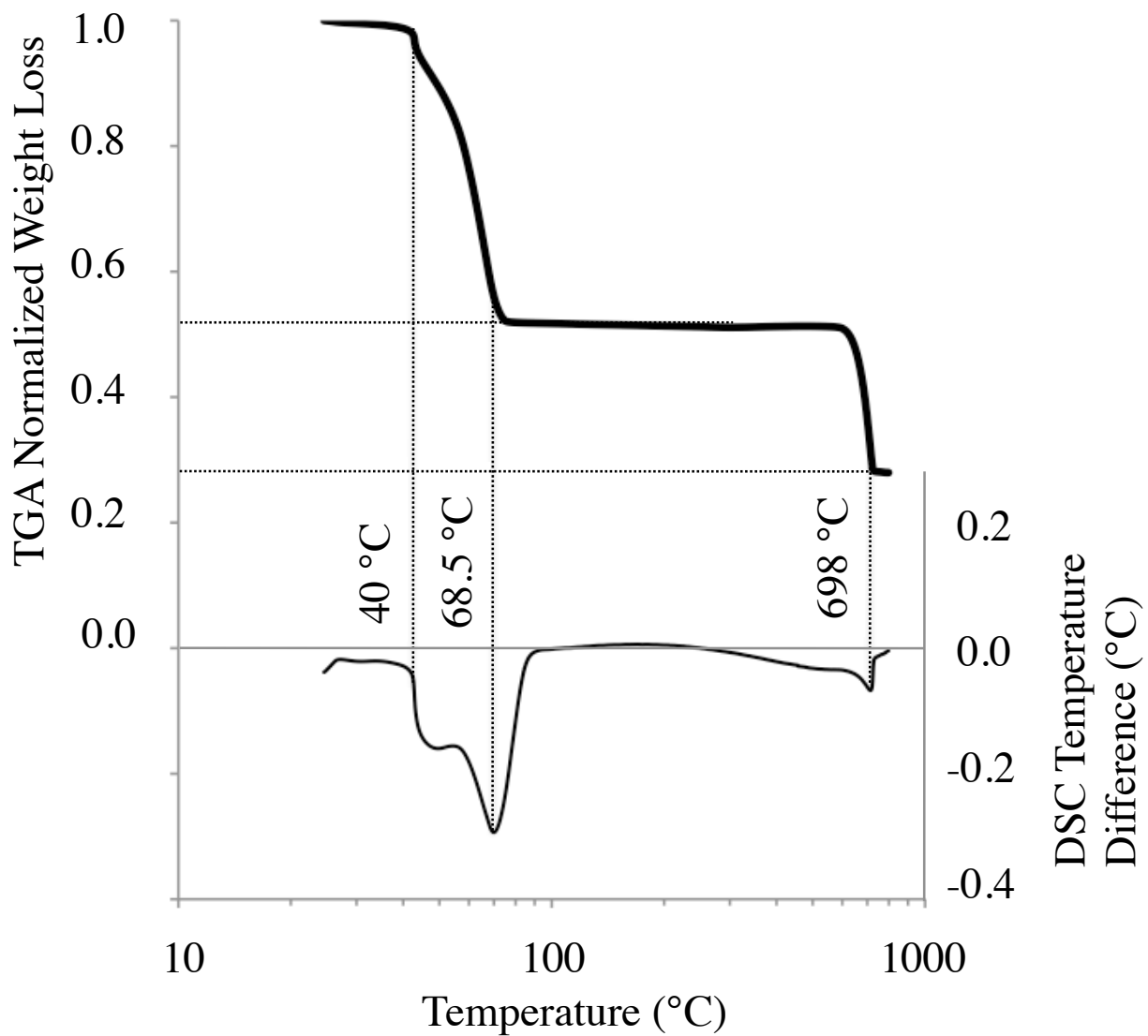


Figure 29. TGA and DSC of ikaite thermal decomposition showing a two-stage dehydration of six stoichiometric water molecules, absence of recrystallization event (no exothermic event), and decarbonation temperature (698°C) consistent with perseverance of an amorphous phase at high temperature.

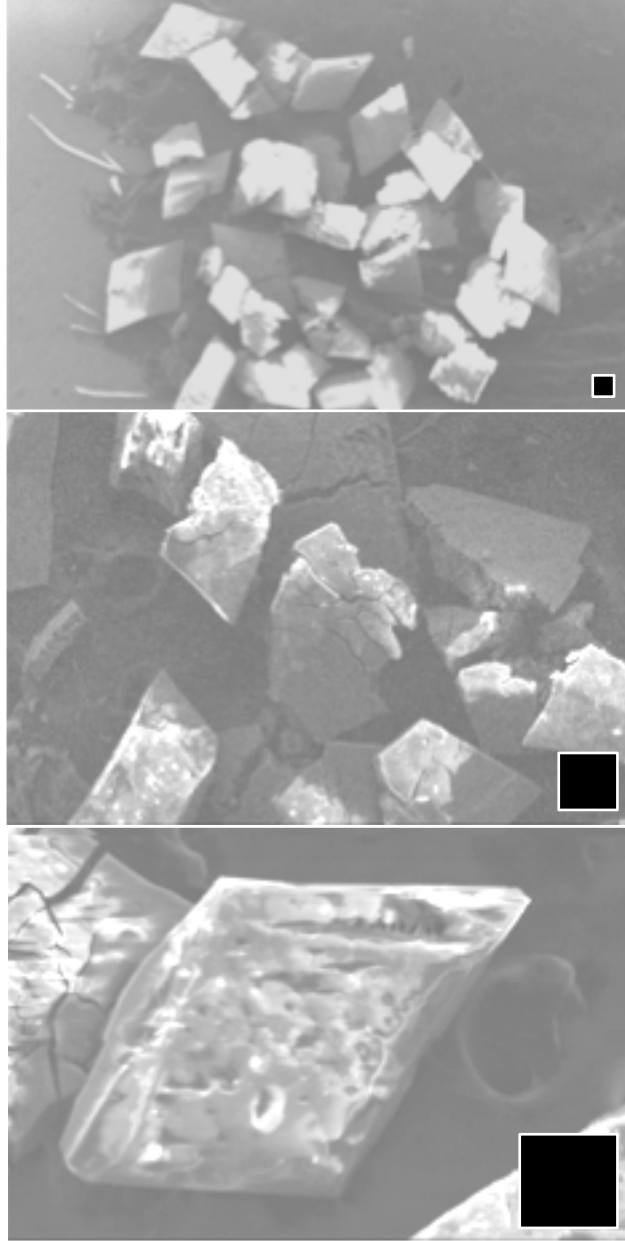


Figure 30. SEM of ikaite crystals displaying rhombohedral habit and onset of decomposition (cracking and vaporization) under SEM conditions. 100 micron scale in all micrographs.

CASTEP NMR Carbon (13) Results

Table 11. Carbon (13) CASTEP NMR properties calculations for reference phases in the Ca-Mg-CO₃-H₂O system. P-denotes conversion to a primitive cell (P1) symmetry. The relaxed symmetry constraints do affect the calculation.

Reference Phase Name	Species/Site	Isotropic Shielding (ppm)	Anisotropic Shielding (ppm)	Chemical Shift Asymmetry	Quadupolar Coupling (MHz)	Quadrupolar Shift Asymmetry
Aragonite	C1	0.47	76.2	0.17	2.98	0.06
Aragonite P	C1	-2.95	77.3	0.16	89.36	0.06
Calcite	C1	3.92	69.6	0.00	2.96	0.00
Calcite P	C1	-0.18	70.7	0.00	87.84	0.00
Dolomite	C1	2.16	72.1	0.00	2.94	0.00
Huntite	C1	8.00	68.3	0.00	3.09	0.00
Huntite	C2	4.53	71.6	0.32	2.96	0.08
Hydromagnesite	C1	12.05	61.2	0.71	2.81	0.32
Hydromagnesite	C2	5.79	65.8	0.19	2.82	0.09
Ikaite	C1	0.80	72.6	0.39	2.85	0.08
Ikaite H-opt P	C1	-1.80	73.2	0.02	84.62	0.03
Ikaite P	C1	-1.14	73.2	0.03	84.13	0.03
Lansfordite	C1	2.41	69.3	0.30	2.86	0.13
Magnesite	C1	0.57	74.5	0.00	2.94	0.00
Monohydrate P	C1	-3.97	77.2	0.31	90.20	0.12
Monohydrate P	C2	-4.38	77.6	0.32	90.31	0.11
Monohydrate P	C3	-4.05	77.2	0.35	90.01	0.14
Monohydrate H-opt P	C1	-2.67	76.6	0.26	89.85	0.06
Monohydrate H-opt P	C2	-4.26	78.0	0.13	90.33	0.02
Monohydrate H-opt P	C3	-3.10	77.4	0.21	90.60	0.04
Monohydrate	C1	-2.68	76.8	0.25	2.91	0.05
Monohydrate	C2	-4.21	78.0	0.17	2.92	0.02
Monohydrate	C3	-3.08	77.5	0.22	2.93	0.04
Nesquehonite	C1	6.41	67.4	0.67	2.71	0.18
Vaterite	C1	-2.27	71.0	0.16	2.98	0.03
Vaterite	C2	-4.39	70.9	0.04	2.95	0.00

Sample SIMPSON Input File for MAS NMR Simulations

```
# MAS quadrupolar spectrum of a single nuclei
```

```
# Uses direct calculation of propagators
```

```
spinsys {  
  nuclei 25Mg  
  channels 25Mg  
  shift 1 12.472p 0 0 0 0  
  quadrupole 1 2 3.19e6 0.00 0 0 0  
}
```

```
par {  
  start_operator I1x  
  detect_operator I1c  
  spin_rate 10000  
  gamma_angles 40  
  sw gamma_angles*spin_rate  
  crystal_file zcw4180  
  np 4096  
  proton_frequency 850e6  
  verbose 1101  
}
```

```
proc pulseseq {} {  
  global par  
  
  maxdt 1  
  
  set tdwell [expr 1.0e6/$par(sw)]  
  acq  
  for {set i 1} {$i < $par(np)} {incr i} {  
    delay $tdwell  
    acq  
  }  
}
```

```
proc main {} {  
  global par  
  
  set f [fsimpson]  
  fsave $f $par(name).fid  
  fzerofill $f 16384  
  fadlb $f 400 0  
  fft $f  
  fsave $f $par(name).spe  
}
```

Sample SIMPSON Input File for Static NMR Simulations

```
#STATIC quadrupolar spectrum of a single nuclei
```

```
# Uses direct calculation of propagators
```

```
spinsys {  
  nuclei 25Mg  
  channels 25Mg  
  shift 1 12.472p 0 0 0 0  
  quadrupole 1 2 3.19e6 0.00 0 0 0  
}
```

```
par {  
  start_operator I1x  
  detect_operator I1c  
#  spin_rate 10000  
#  gamma_angles 40  
#  sw gamma_angles*spin_rate  
  sw 40322.6  
  crystal_file zcw4180  
  np 4096  
  proton_frequency 850e6  
  verbose 1101  
}
```

```
proc pulseseq {} {  
  global par
```

```
#  maxdt 1
```

```
  set tdwell [expr 1.0e6/$par(sw)]  
  acq  
  for {set i 1} {$i < $par(np)} {incr i} {  
    delay $tdwell  
    acq  
  }  
}
```

```
proc main {} {  
  global par
```

```
  set f [fsimpson]  
  fsave $f $par(name).fid  
  fzerofill $f 16384  
  fadlb $f 400 0  
  fft $f  
  fsave $f $par(name).spe  
}
```

Sample CASTEP-Related Input Files

```
comment : CASTEP single point energy parameter file
task : SinglePoint
xc_functional : PBE
spin_polarized : false
opt_strategy : Speed
page_wvfns : 0
cut_off_energy : 600.0000000000000000
grid_scale : 1.7500000000000000
finite_basis_corr : 0
elec_energy_tol : 2.0000000000000000e-006
max_scf_cycles : 100
fix_occupancy : true
metals_method : dm
mixing_scheme : Pulay
mix_charge_amp : 0.5000000000000000
mix_charge_gmax : 1.5000000000000000
mix_history_length : 20
nextra_bands : 0
calculate ELF : false
calculate_stress : false
popn_calculate : true
calculate_densdiff : false
popn_bond_cutoff : 3.0000000000000000
pdos_calculate_weights : false
num_dump_cycles : 0
```

Sample CASTEP-Related Input Files

```
comment : CASTEP NMR properties parameters input file
task : MagRes
continuation : default
spin_polarized : false
magres_method : crystal
magres_task : NMR
magres_max_cg_steps : 250
bs_max_iter : 250
bs_max_cg_steps : 50
bs_eigenvalue_tol : 1.0e-9
pdos_calculate_weights : false
num_dump_cycles : 0
```

Sample CASTEP-Related Input Files

comment: CASTEP cell file of ikaite

%BLOCK LATTICE_CART

8.263548030058960	0.000000000000001	-3.102607322061360
0.000000000000000	8.323499999999999	0.000000000000001
0.000000000000000	0.000000000000000	11.053200000000000

%ENDBLOCK LATTICE_CART

%BLOCK POSITIONS_FRAC

H	0.5724999904632570	0.6869000196456910	0.0017000000225380
H	0.6373999714851381	0.8062999844551090	0.0904999971389771
H	0.3679000139236450	0.1079000011086460	0.3531000018119810
H	0.8812000155448910	0.5931000113487240	0.4724999964237210
H	0.7788000106811520	0.8859999775886540	0.3538999855518340
H	0.6279000043869020	0.9915000200271610	0.3307000100612640
H	1.0724999904632571	1.1869000196456909	0.0017000000225380
H	1.1373999714851382	1.3062999844551089	0.0904999971389771
H	0.8679000139236450	0.6079000011086461	0.3531000018119810
H	1.3812000155448909	1.0931000113487241	0.4724999964237210
H	1.2788000106811519	1.3859999775886540	0.3538999855518340
H	1.1279000043869019	1.4915000200271611	0.3307000100612640
H	-0.5724999904632570	0.6869000196456910	0.4982999999774621
H	-0.6373999714851381	0.8062999844551090	0.4095000028610229
H	-0.3679000139236450	0.1079000011086460	0.1468999981880190
H	-0.8812000155448910	0.5931000113487240	0.0275000035762790
H	-0.7788000106811520	0.8859999775886541	0.1461000144481661
H	-0.6279000043869020	0.9915000200271611	0.1692999899387360
H	-0.0724999904632569	1.1869000196456911	0.4982999999774620
H	-0.1373999714851381	1.3062999844551091	0.4095000028610229
H	0.1320999860763550	0.6079000011086460	0.1468999981880191
H	-0.3812000155448910	1.0931000113487239	0.0275000035762790
H	-0.2788000106811520	1.3859999775886540	0.1461000144481660
H	-0.1279000043869020	1.4915000200271611	0.1692999899387360
H	-0.5724999904632570	-0.6869000196456910	-0.0017000000225380
H	-0.6373999714851381	-0.8062999844551090	-0.0904999971389771
H	-0.3679000139236450	-0.1079000011086460	-0.3531000018119810
H	-0.8812000155448910	-0.5931000113487240	-0.4724999964237210
H	-0.7788000106811520	-0.8859999775886540	-0.3538999855518340
H	-0.6279000043869020	-0.9915000200271610	-0.3307000100612640
H	-0.0724999904632569	-0.1869000196456911	-0.0017000000225380
H	-0.1373999714851381	-0.3062999844551090	-0.0904999971389771
H	0.1320999860763550	0.3920999988913540	-0.3531000018119810
H	-0.3812000155448910	-0.0931000113487241	-0.4724999964237210
H	-0.2788000106811520	-0.3859999775886541	-0.3538999855518341
H	-0.1279000043869020	-0.4915000200271610	-0.3307000100612640

H	0.5724999904632570	-0.6869000196456910	0.5017000000225380
H	0.6373999714851381	-0.8062999844551090	0.5904999971389772
H	0.3679000139236450	-0.1079000011086460	0.8531000018119810
H	0.8812000155448910	-0.5931000113487240	0.9724999964237211
H	0.7788000106811520	-0.8859999775886541	0.8538999855518340
H	0.6279000043869020	-0.9915000200271611	0.8307000100612640
H	1.0724999904632571	-0.1869000196456911	0.5017000000225380
H	1.1373999714851382	-0.3062999844551091	0.5904999971389772
H	0.8679000139236450	0.3920999988913540	0.8531000018119811
H	1.3812000155448909	-0.0931000113487241	0.9724999964237211
H	1.2788000106811519	-0.3859999775886541	0.8538999855518340
H	1.1279000043869019	-0.4915000200271610	0.8307000100612640
C	0.0000000000000000	-0.1941000074148180	0.2500000000000000
C	0.5000000000000000	0.3058999925851820	0.2500000000000000
C	0.0000000000000000	0.1941000074148180	-0.2500000000000000
C	0.5000000000000000	0.6941000074148180	-0.2500000000000001
O	0.0272000003606081	-0.1145000010728840	0.1576000005006790
O	0.6146000027656560	0.7221999764442441	0.0913000032305717
O	0.2860000133514400	0.0582000017166138	0.3828000128269200
O	0.6707000136375430	0.8848999738693241	0.3589000105857850
O	0.5272000003606081	0.3854999989271160	0.1576000005006790
O	1.1146000027656560	1.2221999764442439	0.0913000032305717
O	0.7860000133514400	0.5582000017166138	0.3828000128269200
O	1.1707000136375429	1.3848999738693240	0.3589000105857850
O	-0.0272000003606081	-0.1145000010728840	0.3423999994993210
O	-0.6146000027656560	0.7221999764442441	0.4086999967694283
O	-0.2860000133514400	0.0582000017166138	0.1171999871730800
O	-0.6707000136375430	0.8848999738693240	0.1410999894142150
O	0.4727999996393919	0.3854999989271160	0.3423999994993210
O	-0.1146000027656560	1.2221999764442442	0.4086999967694283
O	0.2139999866485600	0.5582000017166138	0.1171999871730800
O	-0.1707000136375430	1.3848999738693240	0.1410999894142150
O	-0.0272000003606081	0.1145000010728840	-0.1576000005006790
O	-0.6146000027656560	-0.7221999764442441	-0.0913000032305717
O	-0.2860000133514400	-0.0582000017166138	-0.3828000128269200
O	-0.6707000136375430	-0.8848999738693241	-0.3589000105857850
O	0.4727999996393919	0.6145000010728839	-0.1576000005006790
O	-0.1146000027656560	-0.2221999764442441	-0.0913000032305717
O	0.2139999866485600	0.4417999982833862	-0.3828000128269200
O	-0.1707000136375430	-0.3848999738693240	-0.3589000105857851
O	0.0272000003606081	0.1145000010728840	0.6576000005006790
O	0.6146000027656560	-0.7221999764442441	0.5913000032305718
O	0.2860000133514400	-0.0582000017166138	0.8828000128269201
O	0.6707000136375430	-0.8848999738693240	0.8589000105857851
O	0.5272000003606081	0.6145000010728839	0.6576000005006790
O	1.1146000027656560	-0.2221999764442441	0.5913000032305718

O 0.7860000133514400 0.4417999982833862 0.8828000128269200
O 1.1707000136375429 -0.3848999738693240 0.8589000105857850
O 0.0000000000000000 -0.3501000106334691 0.2500000000000001

O 0.5000000000000000 0.1498999893665309 0.2500000000000000
O 0.0000000000000000 0.3501000106334691 -0.2500000000000001
O 0.5000000000000000 0.8501000106334690 -0.2500000000000001
Ca 0.0000000000000000 0.1467999964952470 0.2500000000000000
Ca 0.5000000000000000 0.6467999964952470 0.2500000000000000
Ca 0.0000000000000000 -0.1467999964952470 -0.2500000000000000
Ca 0.5000000000000000 0.3532000035047530 -0.2500000000000000

%ENDBLOCK POSITIONS_FRAC

%BLOCK KPOINTS_LIST

0.3333333333333333 0.3333333333333333 0.2500000000000000 0.2222222222222222
0.3333333333333333 0.3333333333333333 -0.2500000000000000 0.2222222222222222
0.3333333333333333 0.0000000000000000 0.2500000000000000 0.1111111111111111
0.3333333333333333 0.0000000000000000 -0.2500000000000000 0.1111111111111111
0.0000000000000000 0.3333333333333333 0.2500000000000000 0.2222222222222222
0.0000000000000000 0.0000000000000000 0.2500000000000000 0.1111111111111111

%ENDBLOCK KPOINTS_LIST

%BLOCK SYMMETRY_OPS

1.0000000000000000 -0.0000000000000000 0.0000000000000000
0.0000000000000000 1.0000000000000000 -0.0000000000000000
0.0000000000000000 0.0000000000000000 1.0000000000000000
0.0000000000000000 0.0000000000000000 0.0000000000000000
1.0000000000000000 -0.0000000000000000 0.0000000000000000
0.0000000000000000 1.0000000000000000 -0.0000000000000000
0.0000000000000000 0.0000000000000000 1.0000000000000000
0.5000000000000000 0.5000000000000000 0.0000000000000000
-1.0000000000000000 -0.0000000000000000 -0.0000000000000000
0.0000000000000000 1.0000000000000000 0.0000000000000000
0.0000000000000000 0.0000000000000000 -1.0000000000000000
0.0000000000000000 0.0000000000000000 0.5000000000000000
-1.0000000000000000 -0.0000000000000000 -0.0000000000000000
0.0000000000000000 1.0000000000000000 0.0000000000000000
0.0000000000000000 0.0000000000000000 -1.0000000000000000
0.5000000000000000 0.5000000000000000 0.5000000000000000
-1.0000000000000000 0.0000000000000000 -0.0000000000000000
0.0000000000000000 -1.0000000000000000 0.0000000000000000
0.0000000000000000 0.0000000000000000 -1.0000000000000000
0.0000000000000000 0.0000000000000000 0.0000000000000000
-1.0000000000000000 0.0000000000000000 -0.0000000000000000

